DEVELOPMENT OF A MACHINE VISION BASED WEED (GOLDENROD) DETECTION SYSTEM FOR SPOT-APPLICATION OF HERBICIDES IN WILD BLUEBERRY CROPPING SYSTEM

by

Tanzeel Ur Rehman

Submitted in partial fulfilment of the requirements
for the degree of Master of Science

at

Dalhousie University
Halifax, Nova Scotia
July 2017

DEDICATION

To my Parents, Dr. Abdul Rehman Tahir and Dr. Farkhanda Jabeen

TABLE OF CONTENTS

LIST OF TABLES

LIST OF FIGURES

ABSTRACT

Wild blueberry crop yields are dependent on heavy agrochemical applications to control weeds competing with crop. Goldenrod is a creeping herbaceous perennial weed that occurred in more than 90% of wild blueberry fields surveyed in Nova Scotia. The objective of this study was to develop and evaluate a graphical user interface based goldenrod detection system using colour concurrence matrices as image processing algorithm and machine learning procedures for spot-application of Callisto® herbicide. The performance of developed goldenrod detection system was tested and evaluated in four wild blueberry fields. Results of laboratory evaluation suggested that developed colour co-occurrence matrices algorithm with a back-propagation classifier has ability to target the goldenrod with an accuracy of 97%. Optimum parameter selection suggested that intensity levels of 256 and a unit image size of 128 × 128 pixels can help to minimize the processing time without compromising the classification accuracy for real-time applications. Results of classifiers development showed that back-propagation artificial neural network classifier performed better than statistical quadratic classifier to classify goldenrod for training and test datasets. Field evaluation results confirmed the higher accuracy of artificial neural network classifier compared to statistical quadratic counterpart. The savings with colour occurrence matrices and artificial neural network classifier were in the range of 32% to 65% depending upon the goldenrod coverage within selected field tracks. This study can help to apply Callisto® site specifically for goldenrod control, thereby allowing the producers to apply agrochemicals in an economic and environment friendly fashion.

LIST OF ABBREVIATIONS AND SYMBOLS USED

AC – Alternating Current

AES – Auto Exposure Shutter

AGC – Auto Gain Control

ANN – Artificial Neural Network

ANOVA – Analysis of Variance

AOI – Area of Interest

ASM – Angular Second Moment

AVG – Average

AWB – Auto White Balance

B – Blue

BGR – Blue-Green-Red

Blobs – Binary Large Objects

BMP – Windows bitmap

BP-ANN – Back-Propagation Artificial Neural Network

bpp – Bits per Pixel

CA – Coverage Area

CCMs – Colour Co-occurrence Matrices

CLR – Common Language Runtime

COM – Communication Port

CON – Contrast

COR – Correlation

cm – Centimeters

CN – Control

CPU – Central Processing Unit

CSV – Comma Separated Value

DAT – Days after Treatment

DC – Direct Current

DENT – Difference Entropies

dB – Decibel

DiB – Device Independent Bitmap mode

DM – Data Model

DGPS – Differential Global Positioning System

DR – Damage Rating

.dll – Dynamic link library

ENT – Entropy

EXG – Excessive Green

FSB – Front-Side Bus

G – Green

g - Gram

GB – Gigabit

GDS – Goldenrod Detection System

GDI+ – Graphics Device Interface

GHz – Gigahertz

GLCMs – Gray Level Co-occurrence Matrices

GPS – Global Positioning System

GR – Goldenrod

GUIs – Graphical User Interfaces

H – Hue

ha – Hectare

Hf_2 – Second Feature of the Hue term

HI – Hue and Intensity

HMM – Hidden Markov Models

HOM – Homogeneity

HS – Hue and Saturation

HSI – Hue, Saturation, and Intensity

I – Intensity

IDM – Inverse Difference Moment

If_2 – Second Feature of the Intensity term

I/O – Input/output

KB – Kilobyte

km– Kilometer

kPa– Kilo Pascal

kW- Kilowatt

L - Liter

LM – Learning Mode

LMC – Land Manager-II Controller

ln – Natural log

LoG – Laplacian-of-Gaussian

LR – Learning Rate

LSD – Least Significance Difference

LUT – Look-up Table

m – Meter

MB – Megabyte

MHz – Megahertz

mm – Millimeters

MRF – Markov Random Field

ms – Milliseconds

MSE – Mean Square Error

MT – Momentum Term

n – number of samples

NaN – Not a Number

NMEA – National Marine Electronics Association

PAC – Percentage Area Coverage

PGP – Percentage of Green Pixels

PM – Product Moment

PVC – Polyvinyl Carbonate

QGDS – Quick Goldenrod Detection System

R – Red

R^2 – Coefficient of Determination

RAM – Random Access Memory

RGGB – Red-Green-Green-Blue

RMC – Recommended Minimum Data for GPS

RTK-GPS – Real-time Kinematics Global Positioning System

S – Saturation

S_p – Pooled Standard Deviation

SAS - Statistical analytical software

S.D. – Standard deviation

SD – Reduced Models developed by STEPDISC

SENT – Sum Entropies

Sf_2 – Second Feature of the Saturation term

SGDMs – Spatial Gray-tone Dependence Matrices

SH – Stem Height

SI – Saturation and Intensity

SSQ – Sum of Squares

TM – Topology Model

UA – Uniform Application

USB – Universal Serial Bus

UTV – Utility Task Vehicle

V - Volt

VR – Variable Rate

VRC – Variable Rate Controller

W - Watt

WBB – Wild Blueberry

WSPs – Water Sensitive Papers

µ – Micro

® – Registered

™ – Trade mark

ACKNOWLEDGEMENTS

First and foremost, I am extremely thankful to ALLAH ALMIGHTY and Holy Prophet MUHAMMAD (PBUH) for all the blessings on me to complete my master's degree and for any good that comes in my life. It's been a long journey, a rough path hardly to walk on alone. Thanks to all the people that helped me getting rid of the obstacles. I feel pleasure in expressing gratitude to Dr. Qamar Zaman, my supervisor for providing me an opportunity to participate in smart sprayer program. His regardless efforts and consistent support during my course of studies helped me to complete this project. I gratefully acknowledge my committee members Dr. Young Ki Chang, Dr. Arnold Schumann, and Dr. Kenneth Corscadden for providing me valuable suggestions, technical assistance, and sincere advices, which enabled me to accomplish my study goals.

I am thankful to Carl Bragg (president, Doug Bragg Enterprises Ltd.) and Peter Swinkels (general manager, Doug Bragg Enterprises Ltd.) for providing the Utility Task Vehicle to carry out the field experiments. Thanks to Joe Slack (president, Slack Farms Ltd.) and Tom Groves (farm manager, Slack Farms Ltd.) for providing the agrochemical supplies and wild blueberry fields to carry out field tests. I am thankful to Doug Wyllie (field manager, Bragg Lumber Company) for allowing me to use his fields for image library development and spray applications. A special thanks to Chris Nelson for his technical help in preparing and coating the camera case. I express my appreciations to Nova Scotia Research and Innovation Trust (NSRIT), Faculty of Agriculture at Dalhousie University, New Brunswick Department of Agriculture, Aquaculture and Fisheries (NB-DAAF) and Bleuets NB blueberries for financially supporting this project.

I want to thank precision agriculture research team Travis Esau (Post-Doctoral fellow), Hassan Shafqat Chattah, Asif Abbas, Muhammad Waqas Jameel, Salamat Ali (Research assistants), Lukas Geldart, Samuel Creelman, Rachel Hirtle, Scott Withrow, and Brooke MacLean

(Summer students) for their help/assistance during image library development, field experimentation and data collection. I will never forget the unconditional help of three wonderful ladies; Marie Law, Pamela Sutherland (Graduate secretaries) and Mandi Wilson (Administrative assistant). I also express my sincere gratitude to Dr. Qamar Zaman, Mrs. Afshan Qamar and their family for providing the care and help during my stay at Dalhousie University, which never let me feel home sick.

Lastly, I would like to thank my loving parents, Dr. Abdul Rehman Tahir and Dr. Farkhanda Jabeen, brother (Musatfeez-ur-Rehman) and sister, without your support, where would I be? I am thankful to my mother for being with me pretty much all through graduate school, for listening to my rants about several things, but most of all, for the love and support that was shown to me through the long days and sleepless nights when I just wanted to give up. A special feeling of gratitude to all my teachers, uncles, cousins and other family members for believing in me and all the mental support they provided during this journey.

CHAPTER 1: INTRODUCTION

An escalated increase in human population has pushed the agricultural community and scientific think tanks around the globe to replace the current uniform application of agrochemicals with innovative solutions for site-specific ones to ensure sustainable agriculture. The rapidly fostering trend of competitiveness and increased production also demands for innovative tools to manage nutrients and pesticides in an economically and environmentally sustainable fashion. Wild blueberry (*Vaccinium angustifolium* Ait.), a fruit crop native to the northeastern North America initially growing in forests, has now been commercially managed and harvested (Jensen and Yarborough, 2004). The presence of randomly distributed weeds and bare spot coverage of 30 to 50% in newly developing area within wild blueberry fields emphasizes the need to develop cost-effective and reliable systems for spot application of agrochemicals on an as-needed basis (Zaman et al., 2011).

Weeds are one of the major yield limiting factor in wild blueberries that uptake plant nutrients, compete with plants, harbor diseases and insects, and hinders the harvesting operation (Kinsman, 1993). Among many other weed species found in wild blueberry fields, goldenrod (*Solidago* spp.) is the most common weed, which grows aggressively in the form of dense weed patches in more than 90% wild blueberry fields in Nova Scotia, Canada (McCully et al., 1991). It was ranked as the fifth most invasive weed by the Wild Blueberry Producers Association of Nova Scotia (Boyd and White, 2010). Goldenrod offers severe competition to the crop because of its overlying doomed foliage (Kinsman, 1993). Currently, goldenrod is managed by uniform application of herbicides, when it is significantly taller than the wild blueberry plants (Boyd and White, 2010).

The dynamics of field plants, residue, and soil ecosystems are exceptionally complicated, but machine vision technology has the potential to systematically unravel and identify the plants using optical properties, shape, and texture of leaves (Meyer et al., 1998). Recent studies indicated that a mathematical process of characterizing, interpreting, and extracting leaf shape and texture based information has a great potential to differentiate the weeds from crop plants (Meyer, 2011). Shape based image analysis involves the classification of weeds and crops on the basis of some simple features including area, perimeter, circularity, aspect ratio, etc. The plant leaf orientation/rotation, canopy overlapping, and differences in the size of weed plant itself impairs the efficiency of such weed classification system (Perez et al., 2000). Textural features provide some botanical information, such as leaf venation, leaf pubescence, and leaf surface coarseness for detecting plant and weed phenotypes, but shadows, bidirectional reflectance of leaf surfaces, and background lighting bridged up together to reduce the efficiency of this method (Neto and Meyer, 2005).

Chang et al. (2012a) developed a color co-oocurence matrices (CCMs) based texture analysis algorithm and extracted eleven textural features to delineate blueberry and weed species. They used statistical multivariate linear classifiers to perform weed identification task. This texture based algorithm did not perform well for goldenrod discrimination from wild blueberry plants (Chang, 2016). Many other researchers have developed innovative solutions for weed and fertilizer management in a site-specific manner for wild blueberry cropping system (Zaman et al., 2011; Chang et al., 2014; Esau et al., 2014); however, very little research has been conducted on the identification of goldenrod for effective management of this weed on an as-needed basis. In order to address this challenge of goldenrod sensing and real-time application of agrochemical on this

weed, a machine vision based weed detection system for spot application of herbicides is considered as a potential solution.

Therefore, the main goal of this research is to develop a graphical user interface (GUI) based goldenrod detection system (GDS) using optimized CCMs as image processing algorithm and machine learning techniques in Microsoft Visual® C#. The developed GDS used statistical multivariate non-linear and backpropagation artificial neural network classifiers for improved goldenrod detection accuracy. The GUI provides on-screen updates of acquired and processed images along with controls to adjust spraying configurations. The processed images can then be used for the automatic toggling of spray nozzles in the areas where goldenrod is detected.

1.1 Objectives

The objectives of this study are:

1. Development of a graphical user interface based goldenrod detection system with an embedded optimized colour co-occurrence matrix algorithm for real-time spot spray,

2. Development of wild blueberry and goldenrod segmentation classifiers using statistical and artificial neural network techniques, and

3. Performance evaluation of the developed goldenrod detection system for spot-application of herbicide in wild blueberry fields.

CHAPTER 2: LITERATURE REVIEW

2.1 Wild Blueberry Cropping System and Weed Management

Wild blueberry is a unique naturally grown perennial crop that is commercially managed in native stands or abandoned farmlands (Eaton and Nams, 2006). Wild blueberries follow a two-year production cycle with the perennial shoots being pruned in alternate years to fortify floral bud initiation and fruit yield (PMRA, 2005). The rhizomatous spread of seedlings forms a clone composed of widespread ramets. As a result, wild blueberry fields contain multiple perennial clones that have tremendous phenotypic variability, demonstrating variable responses to management (Glass and Percival, 2000).

The "wild nature" of the crop is responsible for the greater variability in terms of weed species and their distribution compared to any other cultivated crop that persistently hinders fruit productivity (Kennedy et al., 2010). Weeds are one of the most significant yield limiting factors (Yarborough and Bhowmik, 1993; Jensen and Yarborough, 2004). Weed flora in blueberry fields traditionally consisted of creeping herbaceous perennial weed species; whereas, many of the new species invading blueberry fields are common vigorous annual weeds of arable fields. The herbaceous perennial weeds produce large number of seeds and require control with herbicides (McCully et al., 1991; Jensen and Yarborough, 2004).

Several species of creeping herbaceous perennial weeds can cause problems in wild blueberry fields, but goldenrod is the most common and most difficult to control (PMRA, 2014), and offers a severe competition because of its ability to crowd out the fields (Hall et al., 1979). Goldenrod occurred in over 90% of wild blueberry fields surveyed in Nova Scotia in the early 1980's (McCully et al., 1991). It was ranked as the fifth most invasive weed by the Wild Blueberry Producers Association of Nova Scotia (Boyd and White, 2010). Current goldenrod management

practices include the uniform application of Callisto® when goldenrod is significantly taller than the wild blueberry plants (Boyd and White, 2010). This traditional method of excessive herbicide application increases production costs and poses environmental hazards (Zaman et al., 2011). Economic and ecological benefits can be achieved by employing new sophisticated methods to fine-tune rate and timing of herbicide applications in a spot specific fashion to control goldenrod pressure in wild blueberry fields.

2.2 Digital Image Processing- A Tool for Precision Spraying

Today, digital images play a vital role in remote sensing, agricultural automation, medicine, education, and traffic control for detection of different objects (Gonzalez and Woods, 2008). Normally, a set of images is investigated to gain insight and to understand the dynamics of data they contain, and how it can be used to extract desired information. For example, an agronomic digital image may contain information related to object's colour, shape, and texture and can be manipulated for weed-crop recognition (Romeo et al., 2013).

2.2.1 Colour based Discrimination

Colour is perceived as a visual attribute of radiation incident on the retina of the human eye. Specifically, colour is perceived as a measure by which radiation of similar spectral content are grouped together labelling the object as red, green, blue, or yellow (Julesz, 1962). Image information related to colour spectra can be utilized to discriminate different plant/weed species and soil residues (Woebbecke et al., 1995). Several vegetative indices have been developed for weed-crop discrimination by using information available in different spectral channels and their combinations (Woebbecke et al. 1995; El-Faki et al., 2000; Lamm et al., 2002; Wang et al., 2003; Mao et al., 2003; Yang et al., 2003; Marchant et al., 2004).

Colour based vegetative indices accentuate a particular spectral band such as plant greenness to provide a better pictorial output for comparison. Woebbecke et al. (1995) used colour chromatic coordinates to develop excessive green (EXG) index for distinguishing plant material from bare soil, wheat straw, and corn residue. Comparatively, less sensitivity of this index to variation in lighting conditions resulted in wide acceptability for the removal of residual background (Campbell, 1996). However, disproportionate effects from numerous lighting sources may overcast a digital image, resulting in the poor identification of green plants and increased background noise (Meyer et al., 2004).

2.2.2 Shape based Discrimination

Shape-based features exploit information regarding geometrical orientation and representation of an object leading towards high-level image processing including object recognition and decision making. Shape features have been used to discern between plant species based on leaf or plant canopy geometry.

Guyer et al. (1986) calculated the geometrical area, perimeter, and width of individual leaves to discriminate corn and weed species. Guyer et al. (1993) considered the leaf and overall plant canopy shapes and achieved 69% correct identification rate for 40 weeds and soybean crop. The authors reported that no single shape feature alone was sufficient to distinguish different plant species. Woebbecke et al. (1995) found similar results for shape features and reported that any particular shape feature did not work efficiently as a plant classifier, because of greater phenological variance among plants of the same species. While leaf shape provides information leading to the identification of plant species, it is difficult to delineate a leaf from mixed occluded canopies in real-time field conditions leading towards the unpredictable behavior of classification systems (Woebbecke et al., 1995).

2.2.3 Texture based Discrimination

Texture is a rich source of visual information about the nature and three-dimensional shape of physical objects. Textures are complex visual patterns composed of specific, spatially repetitive sub-patterns of surfaces that have characteristic brightness, slope, colour, and size, and can be regarded as similarity grouping in an image (Rosenfeld and Kak, 1982). Local sub-pattern properties include lightness, uniformity, density, roughness, smoothness, regularity, linearity, randomness, and granulation (Levine, 1985).

Colour and leaf shape features alone may not be sufficient to consistently distinguish between young weed and crop species. The colour or tonal detail for texture was first described by quantification of co-occurrence of tonal pairs or contrast also known as spatial tonal frequency (Haralick et al., 1973). Wavelet analysis and energy have been recently suggested as a frequency based textural analysis for segmenting weeds embedded in canopies (Tang et al., 2003).

2.3 Texture Analysis Methods

Numerous textural analysis algorithms have emerged over the last few decades to retrieve different levels of information from underlying scenes (Haralick, 1979). These methods have been widely used and studied in depth; however, there is no general consensus regarding which method provides the best information (Haralick, 1979). Classically, texture analysis approaches are broadly categorized in; structural, model-based and transform domain descriptors (Tuceryan and Jain, 1998), which are briefly discussed in the following sections.

2.3.1 Structural Descriptors

Structural approaches utilize well-defined primitives (micro-texture) and organization of spatial dependencies (macro-texture) of those primitives to describe textural arrangements (Haralick, 1979; Levine, 1985). The textural features were calculated by defining the spatial

placement of particular primitive (Blostein and Ahuja, 1989). Carlucci (1972) developed a textural extraction model using line segments, open, and closed polygons as primitives with the placement rule being defined by tree and subtrees syntactically in a graph like language.

Zucker (1976) conceived real texture as a distortion of an underlying ideal texture and has exploited the isomorphic graph theory of usual tessellation to express the primitive placement rule for ideal texture. A mathematical transformation of these ideal graph primitives was distorted for inferring actual textural patterns. Binary large objects (Blobs) have ample information contained within them to explain the textural associativity of image objects (Voorhees and Poggio, 1988). They applied Laplacian-of-Gaussian (LoG) filter at different angular orientations to identify tonal variation of geographically distributed image elements to extract the Blobs. Blostein and Ahuja (1989) also opted the same technique to locate the spatially occluded or fine scale textured surfaces by detecting systematic variability in the area, density, and aspect ratio of image elements. These apparent changes in texture element properties can be analyzed to recover information about the physical layout of the scene.

Structural descriptors provide a decent symbolic depiction of the image; however, they are more useful for generating the synthetic images than analysis task. Methods based on these descriptors have never been proved as promising solutions for natural textures due to the substantial variability in both micro and macro-texture and vague boundaries, segregating them in natural conditions (Haralick, 1979).

2.3.2 Model-Based Descriptors

Model-based texture analysis attempts to interpret an image texture by developing a generative image model (Cross and Jain, 1983; Pentland, 1984; Chellappa and Chatterjee, 1985; Derin and Elliott, 1987; Manjunath and Chellappa, 1991; Materka and Strzelecki, 1998). The

model parameters capturing the essential perceived qualities of texture are calculated, followed by image analysis. McCormick and Jayaramamurthy (1974) developed an autoregressive model by assuming linear dependence of an image pixel on its neighboring pixels and assigned a weighted average tonal value on the basis of linear associativity to synthesize texture. The image segmentation was carried out by estimating model parameters using maximum-likelihood approaches (Tou and Chang, 1976; Deguchi and Morishita, 1978). Several models have been developed on the basis of a Markov random field (MRF) approach; a probabilistic process considering all interactions as local. The probability that an image pixel having specific textural state is utterly determined by the probabilities of neighboring pixels (Blake and Zisserman, 1987). The MRF based models can capture highly detailed local information in an image and have been applied to various image processing applications such as texture synthesis (Cross and Jain, 1983), texture classification (Chellappa and Chatterjee, 1985), image segmentation (Cohen and Cooper, 1987), image restoration (Geman and Geman, 1984), and image compression (Chellappa and Chatterjee, 1985).

Geman and Geman (1984) segmented image texture by deploying Markov and Gaussian random field-based models together to take full advantage of posterior probability. Hidden Markov Models (HMM) out-performed other MRF based methods in texture discrimination as they attempted to discern the fundamental structure of image that was not even directly observable with the naked eye (Povlow and Dunn, 1995). Panjwani and Healey (1995) developed a new MRF model for colour texture segmentation by elaborating maximum pseudo-likelihood scheme for estimating model parameters from different textural regions. A set of a large number of parameters originating between and within different colour bands exponentially increases the computational complexity and cost leading it to non-adaptable approach (Bennett and Khotanzad, 1998).

Model based textural analysis techniques are scale and rotation variants that changing scale and direction of an image would result in significantly different model parameters leading towards misclassification of image segments (Haralick, 1979). Another disadvantage is that the template model will always be used to segment the images having properties very similar to the source image making them less suitable for real-time image segmentation (Campbell, 1996). Furthermore, computational complexity arising in estimating model parameters is of primary concern (Haralick, 1979).

2.3.3 Transform Based Descriptors

The human brain performs highly recursive frequency analysis along with spatial information for analyzing the surface texture of any image data (Julesz, 1962; Campbell, 1996). In order to mimic this approach, several frequency (times the particular tonal value occurred in an image), spatial or joint spatial-frequency domain methods were developed for calculating multi-scale image-textural features (Cohen, 1989). These descriptors represent an image in a space whose coordinate system has an interpretation that is closely related to the characteristics of image tonal frequency (Rosenfeld and Kak, 1982).

The frequency analysis of the textured image is best done in the Fourier domain (Rosenfeld and Weszka, 1976). Weszka et al. (1976) used the Fourier transform to classify the aerial photographs into five land use classes on the basis of frequency based textural variation with an accuracy of 74%. Coggins and Jain (1985) used a set of frequency and orientation-selective filters in a multichannel filtering approach to detect and classify synthetic textures. Haralick et al. (1973) compared textural features extracted from the Fourier transform and second order statistics. They reported that Fourier features performed poorly due to lack of spatial localization.

The introduction of spatial dependency in the Fourier transform by using a filter window (resolution) function resulted in joint spatial-frequency domain, called Gabor transform (Turner, 1986). Tang et al. (1999) developed a weed classification system using a Gabor filter to acquire joint spatial-frequency characteristics of weed texture images. Gabor based approaches were disapproved due to their non-orthogonality resulting in the redundant features at different scale and orientation of filter window (Teuner et al., 1995). Moreover, there is no single filter resolution at which one can localize a spatial structure in natural features (Daugman, 1985).

Frequency and spatial localization of image texture can also be achieved by mining the image data at multi-resolution scale; called Wavelet transformation (Mallat, 1989). This approach treats any image variability as a small wave having a particular frequency for a limited duration (Gonzalez and Woods, 2008). The problem with wavelet based techniques, however, is that they are not resistant to variation in image caused by the movement of object pixels (Brady and Xie, 1996).

2.3.4 Statistical Descriptors

Describing texture by using statistical measures was initially perceived from experiments on human visual pattern discrimination (Julesz, 1962). Julesz's experiments suggested that the human ability to discriminate between different objects can be described by tonal frequency or probability measures of two neighboring pixels having specific brightness values. Darling and Joseph (1968) extended the idea of statistical measures of image texture by extracting a set of features based on classical statistical measures of mean and variance of image gray tones along with entropies in horizontal and vertical directions. However, computation of these features without performing gray tone normalization generated different results of the same scene.

Rosenfeld and Troy (1970) adapted a procedure based on gray tone differences of adjacent image elements for measuring textural coarseness. Later, variability in textural coarseness was used for boundary detection (Rosenfeld and Thurston, 1971). Haralick et al. (1973) developed "spatial gray-tone dependence matrices (SGDMs)" by using probability measures of the spatial distribution of neighboring tonal variation at different orientations. They suggested using the set of four features extracted from these matrices to classify image objects. Fourteen features extracted from these matrices were used for aerial photographs and satellite imagery with accuracies of 82% and 83%, respectively (Haralick et al., 1973).

Shearer and Holmes (1990) introduced the idea of hue-saturation-intensity (HSI) colour features to SGDMs and named it as CCMs. They generated three co-occurrence matrices, one for each HSI colour plane and extracted the textural features as suggested by Haralick et al. (1973). Shearer and Holmes (1990) used a colour co-occurrence approach for classifying the different types of nursery stocks with an accuracy of 91%. Burks et al. (2001) developed a weed discrimination system based on CCMs followed by statistical discriminant analysis and stated an overall accuracy of 93%. Burks et al. (2005) reported an increased weed classification accuracy of 97% using a similar approach with a back-propagation neural network based classification system. Significantly higher weed classification rates by using CCMs with relatively low computational time make it a good candidate for real-time goldenrod detection.

2.4 Machine Learning Techniques for Plant Cover Classification

The quantitative textural features can be employed to develop a classifying criterion which can be utilized to supervise the classification of a new unknown observation into one of the two or more classes/groups (Pao, 1989). This classification criterion can learn from externally supplied successive real field plant cover instances to make predictions about similar future instances

(Marchant and Onyango, 2003) and will be able to adapt to any unforeseen changes in data on the basis of the similarity of supplied instances (Pao, 1989). A large number of techniques can be utilized to develop these classification criterions on the basis of the dimensional nature of input data and output classes. These techniques; however, can be broadly categorized into two basic types, statistical and artificial intelligence-based techniques.

2.4.1 Statistical Classifiers

The statistical methods for creating the classification rule are developed on basic probability theory of calculating the probability of belonging to an individual class. These methods were used in a large number of studies to discriminate the weed from crop plants. Gebhardt et al. (2006) used maximum-likelihood classification method to discriminate between the broadleaf weed species and reported an overall classification accuracy ranging from 71% to 91%. A similar approach for identifying the broadleaf weed patches reported the overall accuracy of 91.3% (de Castro et al., 2013).

Shearer and Holmes (1990) developed a weed classification criterion by modeling the textural features extracted from the CCMs through the generalized squared distances based discrimination procedure and were able to achieve a maximum classification accuracy of 90.9% on the test image dataset with the parametric model. Lee et al. (1999) adopted this approach and developed a robotic weed control system for the tomatoes. They were able to correctly classify the 68.8% and 73.1% of the tomatoes and weeds, respectively.

Meyer et al. (1998) used the contrast enhancement and gray level co-occurrence matrices along with the statistical methods for classifying the two species of grasses, broadleaf weeds, and the soil residue. In addition to the Bayesian approach, they used the canonical correlation approach to finding the linear combination of only two quantitative variables best modeling the class

differences. Chang et al. (2012a) followed the same statistical pattern for classifying the bare spots, wild blueberry plants, and weeds. They reported the maximum achievable accuracies of 100.0%, 98.9% and 93.9% for the bare spots, wild blueberry, and weeds, respectively with linear discriminant function. The similar statistical techniques can be utilized to model the CCM features for the prediction of the goldenrod in the wild blueberry cropping system and may result in the real-time herbicide applications.

2.4.2 Artificial Neural Network Classifiers

Artificial neural network (ANN) is an information-processing framework based on the structure of the biological neural system which learns the association between the input and output variables (Tu, 1996). The key element of this paradigm is the novel structure of the information processing system capable of extracting the useful classifying non-linear functional relationships (Pao, 1989). Yang et al. (2002) developed the ANN based classifying relationship for the identification of crops and weeds in maize fields. The ANN model with the classical vegetative index from each pixel was developed to discriminate between maize plants and weeds. The results evaluated that the artificial neural networks have the potential for accurate and fast image processing and identification. The correct classification rate was found to be 90-100% for corn and 60-70% for the weeds.

Tang et al. (1999) characterized the images into broadleaf and grass categories with 100% classification accuracies using the Gabor wavelet based textural analysis algorithm followed by the three-layered feedforward, back-propagation ANN classifier. Cho et al. (2002) modeled the canopy shape features using the ANN classifier trained with the Log-Sigmoid function for delineating the weed plants from radish fields. They achieved approximately 93% accuracy in both cases. Burks et al. (2005) compared the performance of four ANN classifiers modeled through the

CCM features. The results of their study indicated that back-propagation ANN classifier resulted in the highest classification accuracy of 97% along with the low computational requirements.

Kavdır (2004) applied the ANN classifiers to distinguish between sunflower plants and cocklebur weeds. A back-propagation neural network classifier was developed to achieve a maximum classification accuracy of 95.3%. The real advantage of using multi-layered ANN classifiers is their ability to learn nonlinear decision surfaces (White, 1989) and their ability to outperform the statistical classifiers particularly in the case of multiple processing systems (Burks et al., 2005). These ANN based classifiers can be developed through the CCM based features for the prediction of the goldenrod in the real-time and can be compared with the statistical approaches to select the most accurate classifier for practical applications.

2.5 Graphical User Interfaces for Agricultural Applications

The development of graphical user interfaces (GUIs) can provide the on-screen updates of continuous real-time sensed data, mapped geographical locations and can help in monitoring and managing the sensed data for different agricultural applications (Schumann and Zaman, 2005; Zaman et al., 2008; Swain et al., 2010; Zaman et al., 2010; Chang et al., 2012b; Farooque et al., 2013). Schumann and Zaman (2005) devised a 32-bit Windows-based GUI with a sensing mast of ultrasonic sensors and differential global positioning system (DGPS) for real-time citrus tree canopy volume and tree height estimation. In addition to the real-time updates of acquired data on computer display unit, this GUI possesses the functionality of generating Microsoft Access database of the graphical location of the individual tree along with its height and canopy cross-sectional area.

Ramsey (2015) designed a GUI for providing the real-time dynamically updated value of the plant height measurement, bale chamber position, hydraulic pressure to weigh the hay bales,

moisture sensor output, and GPS location. They developed another Windows based GUI to mark the current positions of the rounded hay bales on a map along with the direction of travel for providing the information to the bales collection unit. Zaman et al. (2010) evaluated a GUI capable of communicating with custom made slope sensor. The GUI was capable of displaying the vehicle speed data along with the slope information on the main display page and storing the slope information along with the GPS co-ordinates in the central database. Farooque et al. (2013) configured the multiple sensors to sense the plant height, fruit yield, and topographic features. All these sensors connectively integrated with a GUI for providing the real-time sensed data and GPS location.

Chang et al. (2012b) developed an automated wild blueberry yield monitoring system consisting of two digital cameras and a real-time kinematics GPS (RTK-GPS) along with a GUI for real-time display of acquired images to observe the performance of the cameras. Similarly, a GUI for controlling multiple cameras and nozzles with an embedded CCMs based algorithm can be developed for wild blueberry fields to target goldenrod site-specifically.

2.6 Smart Spraying System

Weeds do not grow uniformly; there is always significant spatial variability in weed plant density and weed type across a field (Lamb and Brown, 2001). However, for operational effectiveness and conformity, the normal psyche of human-being is to spray the entire field at a uniform rate (Stafford and Miller, 1993).

The core goal of chemical application systems is to apply chemical or biological crop protection products to increase crop growth, health, and yield. Many variable rate (VR) spraying technologies have been developed to control various weed species (Shearer and Holmes, 1990; Franz et al., 1991; Tang et al., 1999; Perez et al., 2000; Burks et al., 2005). Zaman et al. (2011)

developed a VR sprayer by using cost-effective ultrasonic sensors in conjunction with a VR controller interfaced to a pocket PC to detect any prevailing height difference between wild blueberry plants and weeds. Although, the system performed well in real-time applications, but, non-detectable height difference due to overlapped canopies proved to be a key element for the failure of the product.

Chang et al. (2014) hypothesized that optical variability of terrain can play a pivotal role in weed-crop segmentation systems and developed green ratio algorithm coupled with classical approach of thresholding to identify bare spots, green weeds (fescue grasses and sheep sorrel) and wild blueberry plants. This algorithm was capable of spraying the newly emerging green weeds, fungus and mosses against well contrasting reddish pruned wild blueberry plants (Chang et al., 2014; Esau et al., 2014) but, due to optical resemblance; green ratio algorithm was not able to identify goldenrod leaving behind the problem as unsolved (Chang, 2016).

Chang et al. (2012a) developed CCMs from six-bit luminance and HSI images and extracted a set of eleven textural features to delineate blueberry and weed species. They used statistical multivariate linear classifiers to perform weed identification task. This texture based algorithm did not perform well for goldenrod discrimination from wild blueberry plants (Chang, 2016). Percival et al. (2014) retrofitted a commercially available boom sprayer with a commercial weed seeker for real time pre-emergent herbicide application. This arrangement did not show acceptable goldenrod detection accuracy resulting into a commercially non-viable option.

To date, little attention has been given to goldenrod, a weed that is very common in wild blueberry fields. Advances in sensing technology and VR control systems allowing them to respond quickly have offered cost-effective alternatives for weed detection. Furthermore, there is great potential for herbicide saving by targeting the goldenrod and varying the application rate to

its density; this further emphasizes the need to develop an algorithm to differentiate goldenrod from blueberry plants for spot application of herbicide with the sprayer. Spot application of herbicide on goldenrod will not only provide better weed control but also ensure economic and environmental sustainability.

CHAPTER 3: MATERIALS AND METHODS

3.1 Mobile Field Imaging System

3.1.1 Image Acquisition Hardware

Image acquisition hardware consisted of four µEye CMOS, USB 2.0 colour cameras (UI-1240-LE, IDS Imaging Development System Inc., Woburn, MA, USA), having a sensor resolution of 1280 × 1024 (horizontal × vertical) pixels. The imaging sensor (EV76C560CT, e2v Technologies Ltd., Essex, UK) had a depth of 8-bits which resulted in the 256 (2^8) different intensity levels for a single colour channel. The sensor used nineteen pixels for true black level adjustment and six pixels on each side for protecting the active photodiodes resulting in the fill factor of 98.09 %. The sensor was covered with a grid pattern of red-green-green-blue (RGGB) Bayer filter to generate a colour image and had a dynamic range of 71.12 decibel (dB). The quantum efficiency of the sensor can vary between 10% and 45% depending upon the wavelength of incident visible light (UI-1240-LE, camera fact sheet, IDS Imaging Development System Inc., Woburn, MA, USA).

The cameras were fitted on a 6.1 m long boom at a spacing of 1.52 m. This boom was fixed on the back of utility task vehicle (UTV) Gator™ XUV 825i (Deere and Company, Moline, IL, USA) at a height of 1.22 m from ground surface. Camera outputs were routed through 12.2 m long USB 2.0 active link extension cables (Sabrent CB-USBXT, Miami, FL, USA) to a 2.70-gigahertz (GHz) Intel® Core™ i7 central processing unit (CPU) and 8.00-gigabyte (GB) random access memory (RAM) fan-less commercial computer (SP675HP, Unicomp Laboratories Inc., NY, USA) installed with 64-bit Windows 7 operating system (Microsoft Corp, Redmond, WA, USA). The computer was powered by a 200 W, 12 Volt direct current (DC) to 120 Volt alternating current (AC) Eliminator™ inverter (Motomaster Inc., Watford, UK) through cigarette lighter receptacle

fixed inside the UTV cabin. A Garmin® GPS 18x receiver (Garmin International Inc., Olathe, KS, USA) was also connected to the computer through a RS232 communication cable.

The wide angle field of view C-mount lenses (LM4NCL, Kowa Optimed Inc., Torrance, CA, USA) having a focal length of 3.5 mm were fixed with cameras. The 3.5 mm lenses were selected to perfectly match with camera sensor size and to capture more details in a single frame because of deeper depth of field. The lenses had manual iris and focus control that helped in adjusting the aperture and focus. All the lenses were setup to a fix aperture of f/4.0 to cover both very bright and dark images in real-time outdoor illumination conditions. Furthermore, the exposure time and digital gain were controlled automatically by auto exposure shutter (AES), auto gain control (AGC), and auto white balance (AWB) controls inside the custom made image acquisition GUI to adjust for variable outdoor illumination conditions. The focus of the lenses was setup to the infinity distance to include 1.22 m (height of camera above ground surface) with enough depth of field during the operation of image acquisition system. The ground resolution was 2.36 m × 1.89 m (horizontal × vertical) on flat ground with this camera-lens arrangement and each pixel covered a flat ground area of approximately 0.18 cm × 0.18 cm (horizontal × vertical).

3.1.2 Image Acquisition Interface

A custom image acquisition GUI program was developed during this study using C# programming language (Microsoft Corp, Redmond, WA, USA) for a 64-bit Windows 7 operating system. The GUI continuously acquire, store, and display the images from four different µEye cameras in real-time (Figure 3-1). The GUI was developed using a “Form” graphical element from the .NET framework library. The GUI merged different objects that displayed the information on computer screen and enabled the operator to interact with application via a mouse, keyboard, or touch screen. The GUI incorporated setup, configuration, and real time monitoring features, to

select the appropriate computer peripherals, and to diagnose correct operation of GPS and cameras individually.

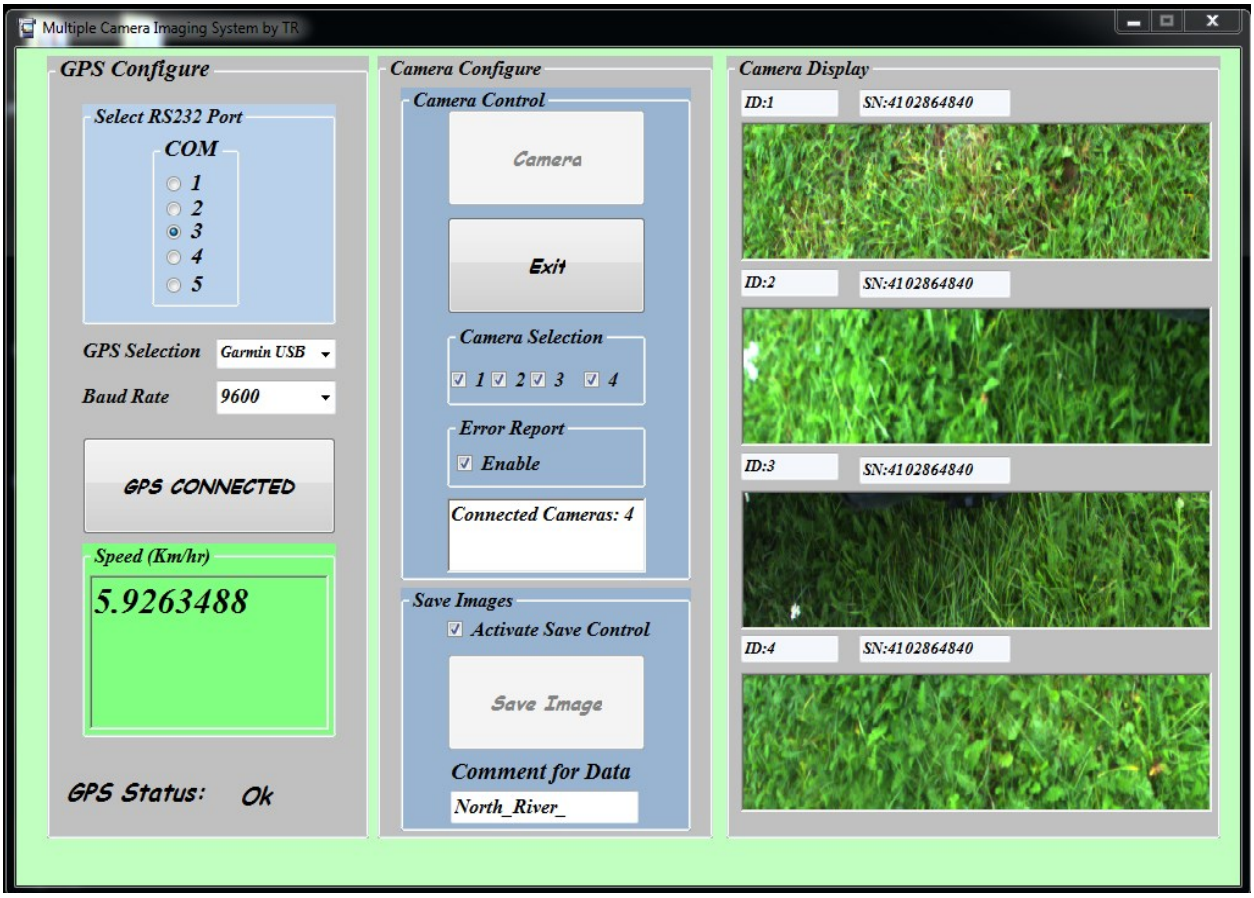

Figure 3-1: Windows based GUI showing different controls and camera images.

An array of "Camera _ Handler" objects was created inside the GUI for initializing the physical cameras using a "for" loop, allocating the memory for a particular image, and initiating the image acquisition process (Figure 3-2). The physical identification number (ID) of cameras was set from 1 to 4. This ID was utilized as an index number of array along with looping structure for initializing driver, memory allocation, and image acquisition procedures for all four cameras at a time. All cameras were initialized by using "Init" command which started the µEye camera driver and established secure connection between them. The "Allocate" command was utilized to allocate the particular section of the computer's memory heap according to image size and "Set

active" command activated the allocated memory to receive the image data in conjunction with "Freeze" command for image acquisition.

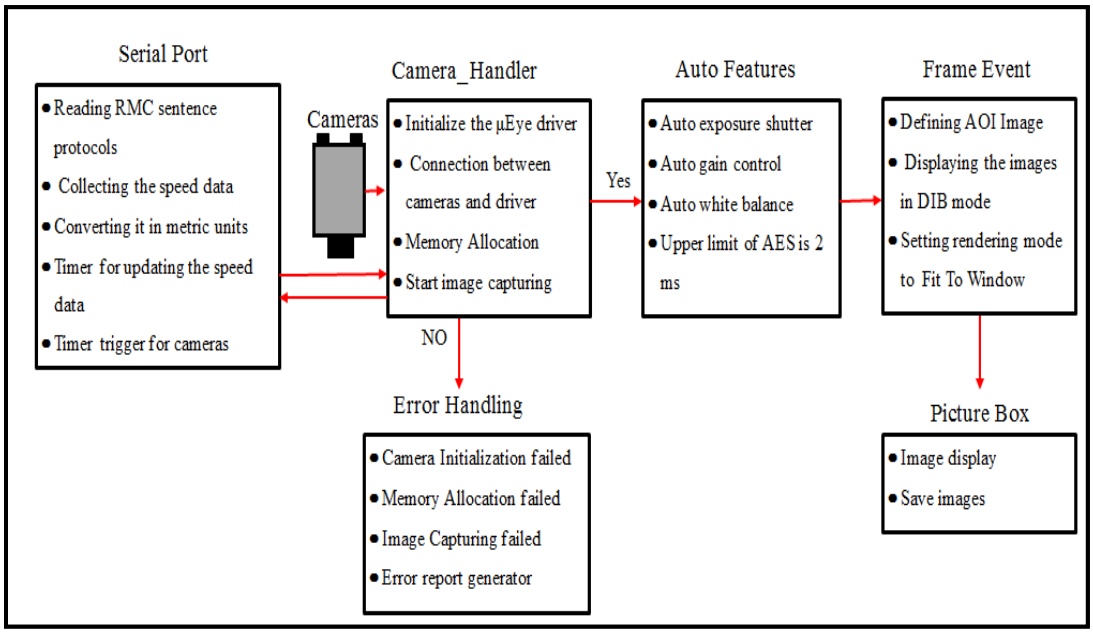

Figure 3-2: Flowchart showing process from image acquisition to display and storage.

Each camera was capable of capturing a frame of 1280 × 1024 pixels; however, an area of interest (AOI) having a size of 768 × 128 pixels was defined by setting the required width, height, and location of the image during memory allocation. The ground resolution of AOI image was 1.52 m × 0.31 m resulting in exact match of image width to camera spacing. The AOI image was located at the coordinates of [200, 200] from top left corner of full frame (Figure 3-3). This location for AOI image was selected to reduce the barrel effect on the sides of a full image frame caused by the wide angle lens. The AOI was not extracted from the center of the full frame image to allow for a greater buffer distance and extra time for CCM and textural analysis of an AOI image. All cameras were programmed to acquire 24-bits per pixel (bpp) blue-green-red (BGR) colour images. As height of the AOI image was 0.31 m, therefore a new frame was captured after every 0.31 m distance. The BGR channel arrangement for image acquisition was selected to perfectly match the

Windows graphics device interface (GDI) for later laboratory and real-time image processing along with proper on-screen display. TheGUI also had functionality of checking the number of cameras attached to computer and allowed the operator to select particular cameras in case additional useable cameras (more than 4) were detected. An error report generator was also incorporated in program to check for any error associated with cameras and display it on GUI in real-time.

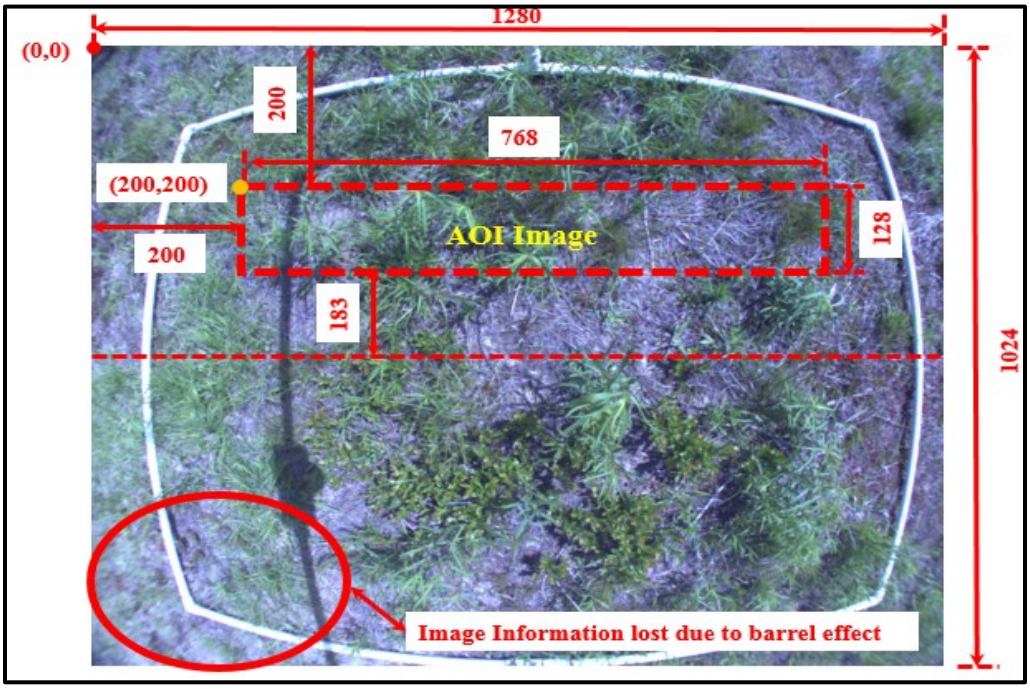

Figure 3-3: Diagram showing the AOI image location with reference to the full frame (all dimensions are in pixels). Barrel effect can be seen in each corner of the image.

Four "Picture Box" controls were added to GUI for displaying the acquired AOI images of four cameras in real time. As the image acquisition process is completed, an event was raised to display the image in each picture box. An event handler named "EventFrame" for "Camera_ Handler" objects was declared to define parameters that were passed to a method responsible for handling the image display. A delegate referring to particular was first created. This delegate was responsible for invoking the display method when the event handler was raised. The image display

was set to device independent bitmap mode (DiB) which is compatible with all graphics cards resulting in more easily and user friendly transfer of the GUI to other computers. The display rendering mode was set to the "Fit to Window" so that all the acquired the AOI images can be displayed properly in the picture boxes.

The GUI featured automatic camera parameters adjustment controls to come up with best quality pictures and to minimize the effects caused by varying outdoor illumination conditions. These automatic parameters were AES, AGC, and auto AWB. The AES function adjusted the exposure time automatically to control the image brightness. However, the motion blur caused by the long term exposure under low light condition, was avoided by setting the maximum exposure time to 2 milliseconds (ms). The AGC function enhanced the image brightness and contrast by controlling the master gain (global gain) value for all the pixels to capture images in cloudy and dark conditions. The artifacts caused by high gain settings were controlled by fixing the maximum gain to a value of 50. These two automatic controls were prioritized in a way that the AES had the highest priority and was set first on the basis of outdoor illumination conditions (bright sunny condition, cloudy condition, or dark condition) and then AGC was adjusted accordingly depending upon the requirement. The AWB control automatically adjusted the white level of the image to reduce the colour casting effect caused by the different colour temperatures of the light. This feature utilized the BGR channels gain for white level adjustment. As the variability in colour temperatures causes the colour offset to red hue or blue hue therefore; the gain controls were adjusted until the red and blue channel brightness matches the average brightness of green channel.

In order to connect the GPS receiver with the GUI, a "serial port" component was added to the GUI with a baud rate, number of data bits, parity, and number of stop bits set by default to 9600, 8, none, and 1, respectively. A GPS communication control box was also added to GUI for

selecting the appropriate RS232 port, changing the baud rate, a text box for displaying the ground speed data, and a button control for opening the serial port component. As soon as secure connection between serial port and GPS receiver was established, a read-only empty string was created for receiving incoming text strings of GPS receiver. The recommended minimum data for GPS (RMC) sentence of the National Marine Electronics Association (NMEA-0183) was separated from incoming strings, parsed, and saved in single line program array. The ground speed (in knots) was parsed from GPS string and converted into the metric unit, using the relationship speed (km hr^{-1}) = 1.852 × speed (knots). This converted speed was again parsed back to string data type to display it on GUI.

Two timer interrupt routines were created in GUI by utilizing standard Windows based timer. One interrupt was utilized for refreshing the raw NMEA sentence protocols at a rate of 5 Hz and another for triggering the cameras to grab new frame after UTV covered a distance of 0.31 m in direction of travel. The ground speed data served as source information for calculating the time required to cover 0.31 m distance and handed it over to second interrupt routine for updating the cameras trigger time. The "Timer.Tick" event was invoked when the time interval defined in milliseconds (ms) by "Timer.Interval" property had elapsed. The default timer routine for triggering the cameras was set to 200 ms in case of GPS receiver signal outage.

The GUI also had "Camera" and "Save" button controls for initializing the whole image acquisition/display process and saving the images in specified folder. The default directory was set to the "C:\\" using "GetFolderPath" method of the "Environment" class. The "Personal" enumeration of "SpecialFolder" class was utilized to access the "Desktop" and folder for saving the images was named as "uEye_Camera_Images". The GUI looked for this folder on desktop and all images were stored in it. The "CreateDirectory" method of the "Directory" class was utilized

to create the “uEye_Camera_Images” in case it was not available on the desktop. The images from all the cameras were stored in the Windows bitmap (BMP) file format to prevent any loss of information caused by image compressions. This is achieved by applying a “.bmp |*.bmp” filter property of “File Dialogue” class. The developed GUI along with image acquisition hardware was utilized for acquiring, displaying, and saving images.

3.1.2.1 Exceptions and Error Handling Capabilities of the Interface

The usability of image acquisition GUI was enhanced by adding error handling layouts. The error handling schemes were divided into two categories, one for handling an exception (non-frequent error) to a certain predefined rule and another for severe problems. The exceptions were handled by using an exception throwing mechanism that enabled the program to continue executing as if no problems were encountered. An exception was shown by displaying a dialogue box containing information about the error and required actions from user. The severe problems were those that caused the program to terminate by notifying the user about error instead of continuing normal execution. The severe error handling mechanisms included the camera-driver connection, memory allocation, image capturing, camera counting, error report generator, and GPS connection checking routines. In addition to the error handler for camera-driver connection, an exception handler was also added to notify the user in case any camera was not properly connected to computer and initiate image acquisition process with available cameras. This exception handler was also responsible for throwing a notification message if any camera connection was lost during the real-field operation of image acquisition GUI. Similarly, an exception handler was added for camera counter function to inform the user about the additional cameras connected to the computer. Almost all the dialogue boxes either used for the severe errors or exceptions were designed as modal and required user response before associated program can continue. However,

the exception handler associated with camera initialization was designed as modaless thereby allowing the program to continue image execution even only one camera is securely connected to the computer.

3.2 Algorithm Development for Goldenrod Detection

Image data include large amount of information, such as colour, texture, and shape. Images of real objects do not have uniform properties, but texture can give information about the image through repetition of some specific pattern. It is one of the most important characteristics in identifying the objects or regions of interest in the images (Julesz, 1962). CCMs based texture analysis method was opted for this study because of its wide spread agricultural applications (Shearer and Holmes, 1990; Burks et al., 2001; Pydipati et al., 2005; Roy et al., 2006; Tahir et al., 2007; Kim et al., 2009) and higher object classification rate (Burks et al., 2005; Tahir et al., 2007). The CCMs were developed by extending the idea of spatial gray-level dependence matrices (Haralick et al., 1973) to colour images (Shearer and Holmes, 1990).

3.2.1 Programming Scope and Objective

The primary objective of GDS was to develop a C# based GUI capable of reading the BGR AOI images in computer RAM directly coming from camera, creating HSI colour images, generating three CCMs from an AOI image, extracting textural features from each CCM, model these features into a meaningful result in terms of goldenrod detection and trigger the powering signal to solenoid valves attached to nozzles depending upon target detection. A streamlined version QGDS (Quick Goldenrod Detection System) of GDS was also developed for laboratory scale image analysis. The main advantage of the QGDS was its batch mode file handling algorithm for generating the CCMs and feature extraction. Moreover, this system was also capable of generating a database of extracted features by transferring them to a comma separated value (CSV)

file. The functionality of QGDS program was limited to the CCMs features extraction. Otherwise, the basic goal of image reading and processing was the same as found in GDS. Both GDS and QGDS were checked for image processing time, optimized, and selected based on their performance and compatibility.

3.2.2 Changing the Colour Model

The preliminary step adopted for construction of CCMs was the conversion of original images having BGR channels to HSI colour space. This colour space is adopted due to its strong tolerance towards any change in lighting condition or reflection (Shearer and Homes, 1990). The hue channel of HSI colour space represented the purity of colour such as pure red, green, and blue in terms of degree, whereas saturation represented the measure 1 to 0 to which pure colour is diluted by neutral colour (Gonzalez and Woods, 2008). The blue (B), green (G), and red (R) intensity levels of individual pixel of an image were utilized to calculate the H, S, and I components of that pixel by using the geometrical transformation relationships (Eqs. 3-1 – 3-4). These relationships are defined by the International Commission on Illumination (CIE) chromaticity diagram (Gonzalez and Woods, 2008).

$$\Theta = \cos^{-1}\{\frac{\frac{1}{2}[(R-G)+(R-B)]}{[(R-G)^2+(R-B)(G-B)]^{1/2}}\} \tag{3-1}$$

$$H = \begin{Bmatrix} \Theta & \text{if B} \leq \text{G} \\ 360-\Theta & \text{if B} > G \end{Bmatrix} \tag{3-2}$$

$$S = \{1 - \frac{3}{R+G+B}\,[Min(R, Min(G,B)]\} \tag{3-3}$$

$$I = (B+G+R)/3 \tag{3-4}$$

A “Colour Conversion” class was developed for this project to read an AOI image coming from the camera using “Marshal.copy” method. This class encapsulated a “RGB2HSI” method for converting the input colour AOI image streaming to HSI images. The input parameters of this

method were set to source image in bitmap format and camera Id for tracking image source. The argument values representing the AOI image along with its format and camera id were supplied to these parameters on method call. Three 1D arrays namely "byteHue, byteSaturation, and byteIntensity" were created in this class. The size of these objects was equal to AOI image size rounded up to 4-byte of AOI image width. These objects were created for storing the converted images. As the acquired AOI images were in 24bpp (8-bits for three channels) format, therefore, a newly calculated H, S, or I value was applied to all channels for individual pixel to change it into respective new colour plane. A "for" loop was utilized to iterate the method call for every pixel in an AOI image thrice to generate three new H, S, and I images.

The "divided by zero" exception was thrown by the method for pixels having same intensity level for all three B, G, and R channels. The similar exception was observed for the pixels with intensity level in all three channels equal to zero. However, the divided by zero exception was avoided by adding a very small factor (1×10^{-6}) in the denominator of hue and saturation relationships (Eqs. 3-5 – 3-6).

$$\theta = \cos^{-1}\{\frac{\frac{1}{2}[(R-G)+(R-B)]}{[(R-G)^2+(R-B)(G-B)]^{1/2}+1*\ 10^{-6}}\} \tag{3-5}$$

$$S = 255*\{1-\frac{3}{R+G+B+1*\ 10^{-6}}\ [Min(R,Min(G,B)]\} \tag{3-6}$$

The H colour plane in this study was defined in terms of circle. This is because the angle ($\theta = 360^{o}$) of circle can be easily normalized in the range [0, 1]. This normalized angle was then linearly transformed to 256 different intensity levels for calculating the H of particular pixel depending upon its B, G, and R components (Eq. 3-7).

$$H = \begin{cases} \frac{\Theta}{360} * 255 & \text{if B} \leq \text{G} \\ \frac{360 - \Theta}{360} * 255 & \text{if B} > G \end{cases} \quad (3\text{-}7)$$

3.2.3 An Overview of Colour Co-occurrence Matrices

One of the defining qualities of the texture is spatial distribution of gray values associated with individual pixel of an image. The CCMs are based on assumption that overall or average spatial relationship of pixels defines the texture of image (Shearer and Holmes, 1990). These matrices are in essence a measure of relative frequencies with which two neighboring pixels, separated by a distance "d" occur in image; one with intensity level "i"; the other with intensity level "j" and assigning these frequencies to a new spatial location defined by tonal values (i, j). An Image [I *(x, y), 0* $\leq x \leq$ N_x*-1, 0* $\leq y \leq$ N_y *-1* with G intensity levels] can be utilized to generate a G × G co-occurrence matrix [P (i, j, d, θ)] for a distance vector d (d_x, d_y) as follows;

$$P(i, j, d, \theta) = freq\{ ((r, s), (t, v)) \in \text{I}\left(\left(N_x, N_y\right), \left(N_x, N_y\right)\right)\} \quad (3\text{-}8)$$

Where (*r, s)* represents coordinate of image I with intensity level *i*, *(t, v)* represents coordinate of image I with intensity level j, N_x is horizontal spatial domain of image I, N_y is vertical spatial domain of image I, d is distance to consider two pixels as neighboring pixels, θ is angular relationship between two neighboring pixels, and *freq* is frequency of elements in the set.

3.2.4 Conceptualization (Construction) of Colour Co-Occurrence Matrices

The development of CCM was conceptualized by using an imaginary 4 × 4 image (I) with 4 intensity levels ranging from 0 to 3 (Figure 3-5a), where 0 represented the darkest and 3 as brightest pixels of image. These intensity levels determined the dimensions of CCM as it was proportional to G × G. The reference pixel was marked with asterisk sign and the surrounding

nearest neighbors were labeled from 1 to 8 in a clockwise direction (Figure 3-6b, other entries were kept intentionally blank). All these neighbors were located at a distance equal to 1. Neighbors labelled 1 and 5 were located at a distance of one pixel and orientation of 0 º from the reference pixel located at (x, y).

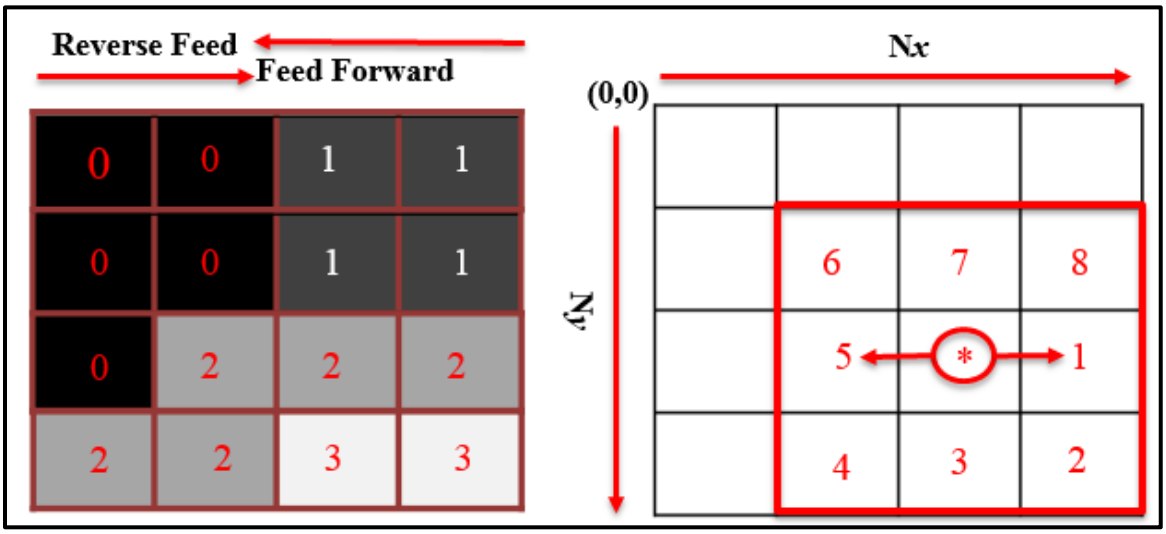

(a) (b)

Figure 3-4: Diagram showing the framework for CCM construction (a) Imaginary 4 × 4 image (b) Labelled image showing the nearest neighbors.

The feed forward mechanism of image scanning was utilized to generate the horizontal set (R_H) of nearest neighbor pixel pairs with intensity levels *i* and *j*. In order to generate the symmetric CCM, the image was scanned again in reverse feed mode to find the pairs separated by distance of – *d* and were added in the set (Eq. 3-8).

$$R_H = \{[(0)(0)]\ [(0)(0)], [(0)(1)], [(1)(0)], [(1)(1)], [(1)(1)],$$
$$[(0)(0)], [(0)(0)], [(0)(1)], [(1)(0)], [(1)(1)], [(1)(1)],$$
$$[(0)(2)], [(2)(0)], [(2)(2)], [(2)(2)], [(2)(2)], [(2)(2)],$$
$$[(2)(2)], [(2)(2)], [(2)(3)], [(3)(2)], [(3)(3)], [(3)(3)]\}$$

The numbers of pairs with intensity level *i* and *j* in the set (R_H) were counted and placed in the matrix (CCM) at a point whose geometric bounds were defined as (*i, j*). For example, the

element at (2, 3) position of horizontal CCM with a displacement vector of 1 pixel was total number of times the two intensity levels with values 2 and 3 occurred horizontally. Extending this concept to additional orientations and summing the results over the entire image, four CCMs were developed from this imaginary image (Figure 3-6).

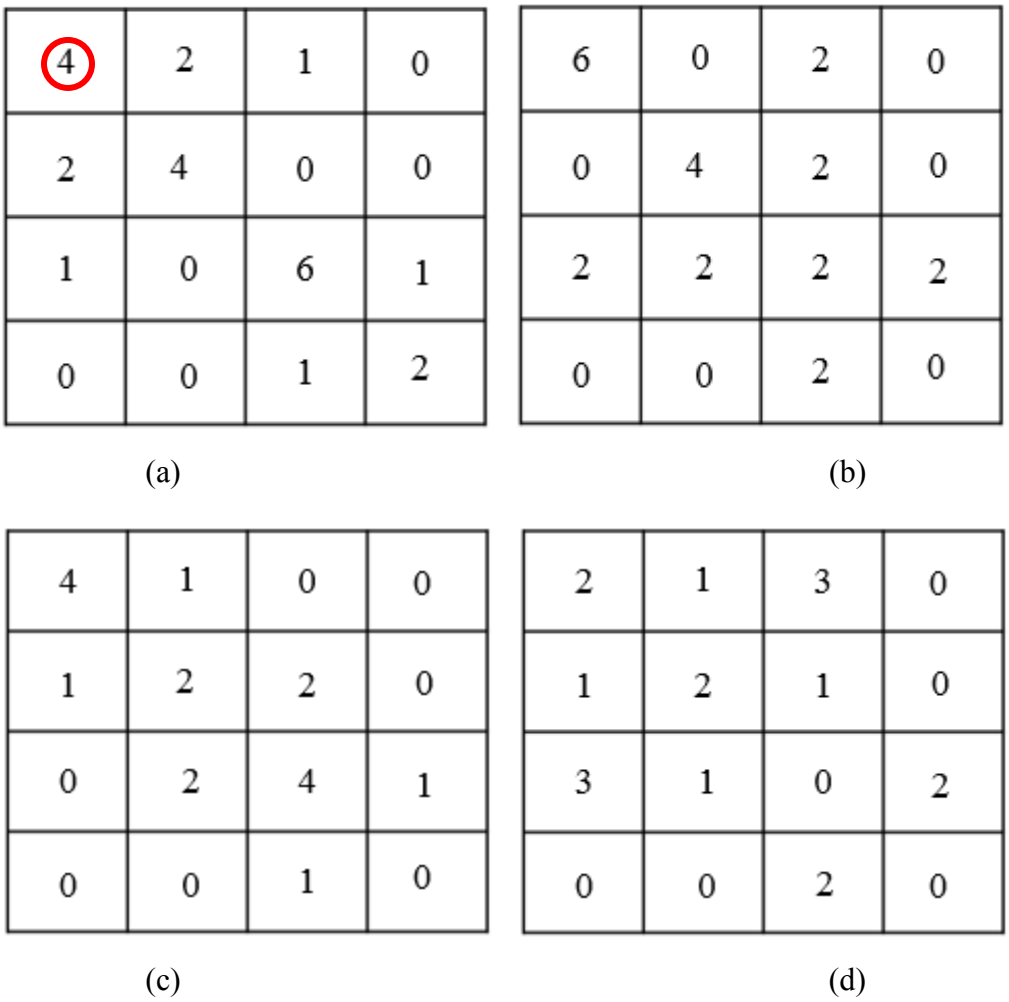

Figure 3-5: Four CCMs at four different orientations with d=1 (a) P (*i, j, 1, 0*), red circle indicates the number of highlighted pairs from R_H (b) P (*i, j, 1, 90*) (c) (*i, j, 1, 45*) (d) (*i, j, 1, 135*).

These CCMs were then normalized (Haralick et al., 1973) by dividing the individual entity in matrix by total number of pairs in each matrix (Eq. 3-9). Normalizing the CCMs resulted in

entities ranging from 0 to 1 which was in streamline with probability rule of minimum and maximum probabilities (Figure 3-6).

$$Normalization = p(i,j,d,\theta) = \frac{P(i,j)}{C_{(i,j,d,\theta)}} \tag{3-9}$$

Where $C_{(i,j,d,\theta)}$ is total number of pairs in matrix with specific orientation and displacement vector.

0.166	0.083	0.041	0
0.083	0.166	0	0
0.041	0	0.25	0.041
0	0	0.041	0.083

(a)

0.25	0	0.083	0
0	0.166	0.083	0
0.083	0.083	0.083	0.083
0	0	0.083	0

(b)

0.222	0.055	0	0
0.055	0.111	0.111	0
0	0.111	0.222	0.055
0	0	0.055	0

(c)

0.111	0.055	0.166	0
0.055	0.111	0.055	0
0.166	0.055	0	0.111
0	0	0.111	0

(d)

Figure 3-6: Four normalized CCMs at four different orientations with d=1 (a) *p* (*i, j, 1, 0*) with C*ij* = 24 (b) *p* (*i, j, 1, 90*) with C*ij* = 24 (c) *p* (*i, j, 1, 45*) with C*ij* = 18 (d) *p* (*i, j, 1, 135*) with C*ij* = 18.

3.2.5 C# implementation of CCMs and Textural Features (CCM Class Construction)

In this study, six unit images of 128 × 128 pixels extracted from an AOI were utilized to control the spray nozzles of a VR sprayer. The unit images were generated to minimize the canopy overlap of goldenrod and wild blueberry plants and helped in preparing the images for supervised learning. This also resulted in improving the learning mechanism and overall efficiency of the statistical and back-propagation artificial neural network (BP-ANN) architecture based models (section 4.3.3). Each unit image was utilized to generate three HSI colour images and each new HSI image was utilized to develop a CCM thus resulting a total of eighteen CCMs (6 unit images and 3 CCMs from a unit image). Unit images of 64 × 64 pixels (total 24 images from an AOI) and 32 × 32 pixels (total 96 images from an AOI) can help to reduce the canopy overlap further, but processing the large number of unit images from an AOI may result in increased overall processing time. Moreover, manual classification of smaller size unit images with naked eye and preparing them for supervised learning purposes resulted in increased complexity.

The concept of CCMs was implemented in C# by developing a "CCM" class responsible for creating eighteen CCMs from three HSI colour images, normalizing these CCMs and extracting a set of 13 features from individual CCM. In case of the QGDS system these features were stored in the database file, while in GDS system these features were utilized for further processing. As frequency in the CCMs is a function of angular relationship and distance between neighboring pixels therefore, in this study; an angular relationship of 0^{o} and a displacement vector of 1 pixel were selected for CCM construction. The displacement vector of 1 pixel was selected as it provided the best result when varied between 1 and 5 (Chang et al., 2012a). Additionally, the textural features were not significantly affected by different orientation angles (0^{o}, 45^{o}, 90^{o}, 135^{o}) as long

as the displacement vector is 1 pixel (Burks, 1997). This resulted into the reduction of twelve CCMs from a unit image to only three CCMs.

A looping mechanism along with the modified index bounds defined by starting location and original index of the one dimensional colour image array was utilized to partition a single H, S, or I image into six two dimensional CCMs from an AOI image (768 × 128 pixels) by utilizing the following relationship.

$$Modified\ Index\ Bound = i * Width * Channels + x_i * Channels + j * Chanles \quad (3\text{-}10)$$

Where *i* is index bound to access the information in rows of HSI images, *j* is index bound to access the information in columns of HSI images, *Width* is AOI image width (768), x_i is starting location of the CCM with reference to 1D image array and *Channels* represented number of colour channels in an AOI image.

The loops incrementally selected each element in 1D HSI arrays by performing 128 iterations. Upon each iteration, two dimensional CCM arrays were evaluated and updated on the basis of element being processed during that iteration. The starting location of six CCMs with reference to 1D image array were set with an interval of 128 elements starting from 0 for first CCM and ending on 640 for last CCM. The width during the scanning of one dimensional image array was limited by defining the maximum limit of the original column index bound to 127 using a "for" loop. The completion of the loop resulted in the development of a CCM. This whole process was repeated for all three HSI images. All the CCMs were normalized by dividing the individual entity with a constant factor of "32512" calculated for displacement vector of 1 pixel and angular relationship of 0^o ($C_{(i,j,1,0)}$).

A process of extracting a set of 13 features was repeated HSI CCMs individually resulting in a total of 39 features from an individual unit image (128 × 128). This set was based on the textural features used by Shearer and Holmes (1990) with two additional features "contrast" and "homogeneity". Instead of defining thirteen variables for a unit image, three arrays (hf [6, 13], sf [6, 13], and If [6, 13]) were defined for storing the CCM features for three HSI images. The row index of these arrays defined the number of unit images and column defined the number of features to be extracted from CCMs. For example, sf [1, 2] represented the second saturation feature of first unit image. The similar interpretations can be extended to hue and intensity images. The order of the features calculation and assignment to respective arrays was done in an order that minimizes the repetitive calculations. Two loops were utilized to iterate the feature calculation subroutines 256 times to extract the information contained in individual CCM. The following is a list of textural features extracted from an individual CCM.

Angular Second Moment (ASM):

The angular second moment calculated the level of uniformity of an image (Shearer and Holmes, 1990). For a uniform image with fewer intensity transitions, CCMs had fewer entries of large magnitude resulting into high ASM. Conversely, a numerous entries of small magnitude resulted in smaller value of ASM feature from a non-uniform image.

$$F_1 = \sum_{i=0}^{Ng-1} \sum_{j=0}^{Ng-1} p(i,j)^2 \quad (3\text{-}11)$$

Where *p(i, j)* is normalized CCM.

Contrast (CON):

Contrast quantified local variations in images. It measured the intensity variations between the reference pixel and its neighbor. In visual perception of real world, the similar intensity level

means the same contrast; therefore, a lower weightage was given to frequency of similar intensities occurring together and frequency of extremely different intensities occurring together were given the high weightage in contrast calculation.

$$F_2 = \sum_{n=0}^{Ng-1}(i-j)^2\left\{\sum_{i=0}^{Ng-1}\sum_{j=0}^{Ng-1}p(i,j)\right\} \quad (3\text{-}12)$$

Inverse Difference Moment (IDM):

IDM computed the closeness of distribution of elements in image. The frequencies of similar intensities occurring together were given higher weightage as compared to frequency of extremely different intensities. The pixels with similar intensity levels were grouped up in the leading diagonal of the CCMs, therefore the maximum weightage of 1 was given to those elements of CCMs. These weights continued to decrease exponentially as (*i- j*) or distance from diagonal increased.

$$F_3 = \sum_{i=0}^{Ng-1}\sum_{j=0}^{Ng-1}p(i,j)\frac{1}{1+(i-j)^2} \quad (3\text{-}13)$$

Homogeneity (HOM):

This feature measured the homogeneity of image by quantifying the extent of intensity levels transition between two different pixels. Homogeneity weighs the pixels by inverse of contrast, with weights decreasing linearly away from the diagonal. Therefore, intensity levels with smaller differences were given the larger weights. The maximum value of the homogeneity can be achieved when all the elements in image are same. Homogeneity and inverse difference moments were inversely related to contrast in terms of pixel pair's distribution.

$$F_4 = \sum_{i=0}^{Ng-1}\sum_{j=0}^{Ng-1}p(i,j)\frac{1}{1+|i-j|} \quad (3\text{-}14)$$

Average (AVG):

The mean of brightness data contained in an image was computed by utilizing this feature. There were two different averages from an individual CCM, one in the horizontal direction and other in vertical direction and can be calculated by using the CCMs row or column index.

$$F_5 = \mu_x = \sum_{i=0}^{Ng-1} i\, p_x(i) \quad \text{OR} \quad F_5 = \mu_y = \sum_{j=0}^{Ng-1} j\, p_y(j) \tag{3-15}$$

The $p_x\,(i)$ and $p_y\,(j)$ represents the marginal probability matrices (Eq. 3-16). For symmetrical CCMs, these matrices were equivalent resulting into the similar average values in the horizontal and vertical direction.

$$p_x(i) = \sum_{j=0}^{Ng-1} p(i,j) \quad \text{OR} \quad p_y(j) = \sum_{i=0}^{Ng-1} p(i,j) \tag{3-16}$$

Sum of Squares (SSQ):

The variatio n in intensity levels of an image was identified by using the sum of squares. It measured the dispersion of intensity values about the mean by assuming normal distribution of intensity levels.

$$F_6 = \sum_{i=0}^{Ng-1} \sum_{j=0}^{Ng-1} [(i-\mu_x)^2 p(i,j)] \tag{3-17}$$

Correlation (COR):

The measure of linear dependences among two neighboring pixels exhibited the correlation among them. The greater degree of association among neighboring pixels resulted into higher value of correlation, whereas the greater intensity variability among neighboring pixels showed zero values. Its value ranged from 0 to 1, with 1 representing the perfectly correlated image intensities.

$$F_7 = \sum_{i=0}^{Ng-1} \sum_{j=0}^{Ng-1} p(i,j) \frac{[(i-\mu_x)(j-\mu_y)]}{\sigma_x \sigma_y} \tag{3-18}$$

Product Moment (PM):

The monotonic associativity among intensity levels of two neighboring pixels gave the information about their covariance (PM). The positive value of higher magnitude indicated that the probability of occurring the similar intensity levels together is higher.

$$F_8 = \sum_{\mathrm{i}=0}^{\mathrm{Ng}-1} \sum_{\mathrm{j}=0}^{\mathrm{Ng}-1} (\mathrm{i} - F_5)(\mathrm{j} - F_5)\mathrm{p}(\mathrm{i},\mathrm{j}) \tag{3-19}$$

Entropy (ENT):

The quantitative measure of repetitive order of intensity values in an image defined its entropy. This feature determined the disorder or level of complexity in an image. An image having the more repetitive patterns of similar intensity levels result into the higher entropy value, thus indicating nature of complexity of objects contained in it.

$$F_9 = Entropy = \sum_{i=0}^{Ng-1} \sum_{j=0}^{Ng-1} [p(i,j)\ \ell \mathrm{n} p(i,j)] \tag{3-20}$$

Sum and Difference Entropies (SENT and DENT):

The sum and difference entropies are difficult to interpret (Shearer and Holmes, 1990). The frequencies summed along the major (leading) diagonal of CCMs resulted into difference matrix, while frequencies summed along the minor diagonal resulted into sum matrix.

$$F_{10} = Sum\ Entropy = \sum_{k=0}^{2(Ng-1)} p_{x+y}(k)\ \ell n(p_{x+y}(k)) \tag{3-21}$$

$$F_{11} = Difference\ Entropy = \sum_{k=0}^{Ng-1} p_{x-y}(k) \ell n\left(p_{x-y}(k)\right) \tag{3-22}$$

Where:

$$p_{x+y}(k) = Sum\ Matrix = \sum_{\substack{i=0 \\ k=i+j}}^{Ng-1} \sum_{j=0}^{Ng-1} p(i,j)\ \ for\ k = 0,1,2,\ldots,2\left(N_g - 1\right) \tag{3-23}$$

$$p_{x-y}(k) = Difference\ Matrix = \sum_{\substack{i=0 \\ k=|i-j|}}^{Ng-1} \sum_{j=0}^{Ng-1} p(i,j)\ for\ k = 0,1,2,\ldots,\left(N_g - 1\right) \tag{3-24}$$

Information Measures of Correlation:

These two features did not exhibit any physical meaning with exception that they are the ratios of different entropies (Haralick et al., 1973; Shearer and Holmes, 1990).

$$F_{12} = Info.Correlation - I = (HXY - HXY1)/\max(HX, HY) \tag{3-25}$$

$$F_{13} = Info.Correlation - II = \left[1 - exp^{-2(HXY2 - HXY)}\right]^{1/2} \tag{3-26}$$

Where:

$$HXY1 = \sum_{i=0}^{Ng-1}\sum_{j=0}^{Ng-1} p(i,j)\ \ell n(p_x(i)\, p_y(j)) \tag{3-27}$$

$$HXY = ENT = \sum_{i=0}^{Ng-1}\sum_{j=0}^{Ng-1} p(i,j)\ \ell n(p(i,j)) \tag{3-28}$$

$$HX = Vertical\ ENT = \sum_{j=0}^{Ng-1} p_y(j)\ \ell n(p_y(j)) \tag{3-29}$$

$$HX = Horizontal\ ENT = \sum_{i=0}^{Ng-1} p_x(i)\ \ell n(p_x(i)) \tag{3-30}$$

$$HXY2 = \sum_{i=0}^{Ng-1}\sum_{j=0}^{Ng-1} p_x(i)p_y(j)\ \ell n(p_x(i)\, p_y(j)) \tag{3-31}$$

The CCM class thrown "Not a Number (NaN)" exception for entropy terms of some images. After checking, it was found that the natural log (*ln*) of zero caused by zero entries in CCMs resulted into this exception. In order to handle this exception for zero entries in CCMs a small factor (1×10^{-6}) was added to natural log section of the entropy terms. This added some biasness to the entropy features, but relatively small magnitude of term made it a good compromise for NaN exceptions. Some of these features were found to be highly correlated and quantified the similar properties in different ways. Many of them were found to be a linear combination or scalar

multiple of the other features, but because of their wide acceptability in agriculture (Shearer and Holmes, 1990; Roy et al., 2006; Tahir et al., 2007) they all were included in this study.

3.3 Development of Plant Cover Classifiers

3.3.1 Field Selection for Image Acquisition

Four wild blueberry fields were selected in central Nova Scotia, Canada to develop an image library containing the images of goldenrod, wild blueberry, bare spots, and mixed canopies. The selected fields were North River I (45° 35' 54" N, 63° 21' 18" W), Cattle Market (45° 21' 52" N 63° 12 '46" W), Londonderry (45° 46' 59" N and 63° 33' 13" W), and North River II (45° 37' 45" N, 63° 22' 19" W). The Cattle Market and North River I fields were in their vegetative growth year during 2015 and in crop year during 2016, while the Londonderry and North River II were in their crop year during the 2015 and in vegetative growth year during 2016. Over the past decade, these fields were commercially managed and received biennial pruning by mowing. The image library was built by acquiring the images during vegetative growth year from each field.

3.3.2 Image Library Development

A task of developing an image library was completed during summer of 2015 and 2016 by acquiring wild blueberry field images focused on goldenrod only, wild blueberry plants only, and mixed canopies. A set of 2701 full frame (1280 × 1024) images was added to library by acquiring the images from North River I and Cattle Market fields during 2015 and were stored in BMP file format to avoid any loss of necessary information. Images were acquired using a µEye camera (UI-1240-LE) fixed with 3.5mm lens at four different day times (8 AM to 9 AM, 11:30 AM to 12:30 PM, 3 PM to 4 PM and 6:30 PM to 7:30 PM) with 100% shade (to mimic cloudy conditions), 50% shade (for reflections) and no shade (natural sunny conditions) from four cardinal directions to include as much lightning and directional variability as possible in acquired data. A rectangular

frame of polyvinyl carbonate (PVC) pipe along with camera housing was made to mount camera at height similar to boom height of mobile field imaging system. This imaging arrangement resulted in relatively good quality images by eliminating the motion blur and hand shake effects during acquisition.

Another set of 9,669 AOI images was added to image library by collecting the data from North River II and Londonderry fields using mobile field imaging system equipped with four cameras during summer 2016. Test tracks containing goldenrod patches were selected and data were acquired from two cardinal directions. To accommodate the effect caused by sun angle, the image acquisition process was repeated at different day times.

3.3.3 Image Pre-Processing and CCM Statistics

The image library was partitioned into two datasets containing 70% of the data for developing and training a wild blueberry and goldenrod segmentation classifier and 30% for validating the classifier. To ensure randomization in image selection for model development, images were arranged according to time in ascending order and two images from same location with two different cardinal directions were selected. This approach minimizes a negative time dependent variability, and reduced the potential for data selection bias between the training and validation test datasets. The AOI images were cropped from the full frame images acquired during 2015 by using IrfanView. The relative location of the AOI image was [200, 200] from top left corner of full frame image. In order to isolate the individual class specimen, 128 × 128 pixel unit images were extracted from AOI images of both years. There were six unit images from individual AOI image. The extracted unit images were manually classified into wild blueberry (WBB) and goldenrod (GR), and were labeled with “spray” or “no spray” tags to aid the classifiers for learning

from these labels at later stage. The manually classified images were rotated thrice at 90˚ to increase the volume of data in both model training and testing phases.

3.3.4 Selection Classifying Variables

The extraction of 39 textural features from an individual unit image (128 × 128) can result into a total number of 234 features (39 × 6) from an AOI image. All of 39 extracted features, have discriminating power; however, some variables contribute less towards the identification of goldenrod and wild blueberry. This might occur due to either class membership means that are not very different on these variables or some variables share the same discriminatory information even though they are individually good discriminators (Klecka, 1980). The inclusion of these variables in the classifying criterion can also decrease the precision of estimated coefficients and predicted values (Klecka, 1980). Another important logical factor for reducing the variable set is to minimize computational time and complexity (Shearer and Holmes, 1990). Therefore, feature selection procedure was carried out on training data to achieve a balance between simplicity (as few variables as possible) and fit (as many variables as needed) to minimize the size of features set.

The process of extracting the sub-set of quantitative features was carried to fulfill the two opposing objectives. First, to make a classifying criterion as complete and realistic as possible by adding more and more features, and second to include as few features as possible to minimize the cost of low discriminatory features.

3.3.4.1 Stepwise Discriminant Analysis

The SAS PROC STEPDISC procedure (SAS Institute Inc., Cary, NC, USA) was used to select subsets (called as data models hereafter) of most suitable discriminating features from the training images by performing stepwise analysis. This procedure was first used for sifting through large numbers (39) of potential independent features and then for fine-tuning the selected data

model (DM) by moving the selected features in or out to get more balanced DM. The stepwise procedure consisting of the forward selection and backward elimination was opted during feature selection. At each forward step, an individual feature or a pair of features with greatest discriminatory power, as determined by the F-statistic and R^2 between the groups mean, was added. After every forward step, DM with added features was analyzed to identify the feature that no longer makes any contribution to discriminatory power and was cast out although it remained eligible for reselection at any future forward selection step. The procedure of adding and removing the features from DM was continued until all possible features have been added or remaining features do not contribute a sufficient power. The feature addition and removal was assisted by defining the significance level to enter (F-to-enter) and significance level to remove (F-to-remove) thresholds. The threshold level for F-to-enter and F-to-remove were 0.0015 and 0.0010, respectively (Chang et al., 2012a). At the end of the each step a multivariate statistic Wilk's lambda was calculated for selected features to measure the class centroid's differences over the selected features.

The STEPDISC procedure was used for individual colour plane and their possible combinations along with control model containing all 39 features for monitoring the relative performance of all developed DMs. All DMs extracted from different colour planes were used for different classifiers development. The classifiers developed by this procedure do not account the relationships between features that have not yet been selected. Moreover, the final classifying model cannot guarantee to be optimal in any specified sense (SAS 9.3 User's Guide, 2011) and can result into the underestimated model. Therefore, in order to guard against the underestimated models, the matrix plots generated by using Minitab 17 statistical software (Minitab Inc. NY, USA) were used to identify features strongly relating to the class memberships. Moreover, these

plots also helped in identifying the features with similar discriminatory power, thereby providing the general guidelines about features necessarily needed to be selected or eliminated.

3.3.5 Development of Statistical Classifiers

The successfully selected DMs were used to define the classification criterion by using SAS PROC DISCRIM procedure (SAS Institute Inc., Cary, NC, USA) based discriminant analysis approach from which a new observation can be identified in future. In order to make a decision between the parametric and nonparametric methods for generating a discriminating function, a multivariate and univariate normality tests were performed in Minitab 17. The normality tests were performed for all the 39 features. The normality tests also helped to identify the outliers in training dataset resulting in exclusion of these extreme scenarios from discriminant function.

The univariate normality test was performed by analyzing the frequency distribution plots of textural features for both goldenrod and wild blueberry classes. The multivariate normality was tested by calculating the Mahalanobis distances between features extracted from CCM of a colour plane and a multivariate space's centroid (overall mean). A scatter plot between squared Mahalanobis distances and quantiles extracted from the chi-square distribution of features was developed from training dataset. This plot was used to subjectively evaluate the multivariate normality and outliers by using the underlying concept that Mahalanobis distances have chi-square distribution. This plot resembled a straight-line for normal data with outliers pointed on upper right corner having the squared Mahalanobis distance notably greater than chi-square quantile value.

A likelihood ratio test for homogeneity to select from within group covariance matrices or pooled covariance matrix was performed at a significance level of 0.1 (Morrison, 1976). The significance of this test resulted in selection of within group covariance matrices leading towards the development of quadratic classification criterion. However, the linear classification criterion

was also developed and compared to the quadratic criterion because of its simple and easy implementation for real-time applications. This comparison also helped to quantify the cost of misclassification in order to make a fair compromise between classification accuracy and execution time. The prior probabilities of goldenrod and wild blueberry classes were set to equal level to treat both of them equally.

The linear classification functions for GR and WBB classes were developed by linearly combining the coefficients with DM features from training dataset (Eq. 3-32). These functions were trained in a way that each linear combination maximizes class differences while minimizing the variation within classes. These classification functions were resolved for textural features of any unknown observation to calculate its class membership scores. The classification of unknown observation into a class having the highest class membership scores served as classification criterion (SAS 9.3 User's guide, 2011). This process of calculating the class scores was repeated for all DMs to develop the individual linear combinations in an effort to get the highest classification accuracy.

$$S_k(X^*) = c_k + b_{k1}X_1 + b_{k2}X_2 + \cdots + b_{kp}X_p \quad (3\text{-}32)$$

Where $S_k(X^*)$ is classification score of k^{th} class for an unknown observation X^*, c_k is constant term for k^{th} class, b_{ki} is Coefficient of i^{th} feature in kth class, X_i is textural feature of an unknown observation X^*.

The quadratic classification criterions were based on the estimation of proximity by measuring the distance of an individual unknown observation to each class centroids and classify the observation to closest class. The distance estimation used in this study was squared Mahalanobis distance (Eq. 3-33). The within group covariance matrices and vectors containing the

means of features in GR and WBB classes were extracted from training data. These within group variance matrices and mean vectors were used to develop and resolve two different generalized squared distance functions for an unknown observation in real-time. The posterior class membership probabilities (Eq. 3-35) calculated from these functions were used as a classifying criterion (SAS 9.3 User's guide, 2011). This procedure of estimating the distances was repeated for all DMs.

$$d_{GR}^2(X^*) = (x - m_{GR})^T \, S_{GR}^{-1}(x - m_{GR}) \tag{3-33}$$

$$D_{GR}^2(X^*) = d_{GR}^2(X^*) + \ln |S_{GR}| \tag{3-34}$$

$$p(GR|X^*) = e^{(-0.5 D_{GR}^2(X^*))} / \sum_n e^{(-0.5 D_{WBB}^2(X^*))} \tag{3-35}$$

Where $d_{GR}^2(X^*)$ represents squared Mahalanobis distance from X^* to class GR, x is a vector containing the quantitative values of features of an unknown observation X^*, m_{GR} is a vector containing means of features in class GR, S_{GR}^{-1} is inverse of within group covariance matrix S_{GR}, $D_{GR}^2(X^*)$ represented generalized squared distance function from X^* to class GR, $D_{WBB}^2(X^*)$ is generalized squared distance function from X^* to class WBB, $p(GR|X^*)$ represented the posterior probability of X^* belonging to class GR.

3.3.6 Development of BP-ANN Classifiers

The multilayer, feedforward, supervised, back-propagation neural networks were trained by using Peltarion Synapse (Peltarion Systems®, Netherlands) software. The same arrays (DMs) of input features selected by the STEPDISC were used for BP-ANN classifiers development. Moreover, use of same set of input variables between statistical and BP-ANN approaches allowed us a fair comparison. The BP-ANN classifiers were developed using DMs with the highest

classification accuracy during DISCRIM procedure along with DM containing all 39 features to compare the relative accuracy of other DMs. The network was trained for each DM on trial and error basis. Each parameter was tweaked individually at a time in an effort to come up with best choice of that particular parameter. The performance of these networks at the end of each tweak was tested by evaluating it on both training and testing data sets. The tweaked networks were extracted using the deployment post-processing tool of Peltarion Synapse software to make a separate and stand-alone WorkArea0.dll (.NET dynamic linking library) file. A C# based command prompt program was written to predict and validate both external and internal data sets by using WorkArea0.dll file and save processed result as a comma separated value (CSV) file. These networks for internal and external validations were tested and evaluated to achieve the highest overall and individual species classification accuracy with Mean Square Error (MSE) as a supplementary criterion to assist the evaluation process.

3.3.6.1 Back-Propagation Topology Design

The precise network topology (number of hidden layers and neurons) required for classifying the GR and WBB classes was experimentally determined with Peltarion Synapse default topology as initial network. The neurons at input layer for particular DM corresponded to number of input features with output layer neurons being fixed to number of classes (GR and WBB). An experimental approach for determining the appropriate number of intermediate hidden layers and neurons was based on the constructive algorithms. The initial network consisted of one hidden layer with number of neurons equal to mean of input and output neuron and were built larger at each successive step. The optimum numbers of hidden neurons for specific training data were also calculated by using $\log_2 (T)$, where T is number of training samples (Mirchandani and Cao, 1989).

The learning parameters including learning rate (LR), learning mode (LM), momentum term (MT), epochs (iterative steps), and mathematical neuron activation function were remained fixed to 0.1, online, 0.7, 1000, and tanh sigmoid, respectively, during this experimentation. The learning parameters remained same for bigger networks except the linear activation function for the neurons of the last hidden layer. The network topology was tested by processing both training and testing data set to calculate and record both individual class and overall classification accuracies with the help of command prompt program. Additionally, MSE was recorded and plotted against the modified network topology.

The same experimental topology design approach was adopted for all high performing DMs and control DM. The topologies were designed so that all DMs converged to a trainable solution. The topology with the highest individual and overall classification accuracies were nominated for further experimentation to select the appropriate learning parameters.

3.3.6.2 Back-Propagation Training Parameters Selection

The successful selection of networks topology led to identify the training parameters that would allow the network to learn from data thereby resulting to achieve the highest classification accuracies. The parameters adjusted during this experimentation include LR, LM, MT, epochs, and mathematical neuron activation function. The topology with the highest classification accuracies were first used to fine-tune the mathematical activation functions. The different mathematical activation functions (tanh sigmoid, logistic sigmoid, linear, sine, Gaussian, superposed logistic sigmoid-I, superposed logistic sigmoid-II, and Morlet) were tested in this session. All other parameters were kept constant (LR = 0.1, MT = 0.8, LM = online, and epochs = 1000), and results were compared by plotting the accuracies against these functions along with MSE.

The LR was varied from 0.025 to 0.150 and MT was varied from 0.7 to 0.95 to generate the matrix of classification accuracies during the next phase. The LR was fine-tuned first followed by adjustments in MT. After each adjustment, individual class and overall accuracies along with MSE were plotted against LR and MT to locate the most suitable values of LR and MT. All these networks were trained for 1000 epochs with most suitable topology and activation function with online training mode to have a fair comparison among these networks. The adjustment of LR and MT was followed by the modifications in LM. The suitable combination of LR, MT, and mathematical function along with appropriate network topology were used to quantify the effect of LM for 1000 epochs. The batch and online learning modes were tested to make the suitable corrections in the weights and biases associated with each neuron by carrying out the gradient search in weight space on the basis of average network error.

In order to generalize the basic relationships between input and output neurons based on the training data, epochs were varied between 500 and 10,000 in a step of 500 epochs. This range of epoch was utilized to minimize the chances of network over-training by getting entrapped in local minima (Bishop, 2007; LeCun et al., 2012). The individual class and overall accuracies were given more weightage as compared to MSE for evaluating the results of epoch experimentation. This was due to the fact that MSE in case of over-trained networks continued to decrease with a compromise being made on the generalization capabilities of the networks. Moreover, networks activated and initialized with different activation functions were analyzed to identify combination of different functions resulting in training of networks at relatively less epochs, thereby further reducing the chance of over-training. The epoch test was performed on appropriate network topology along with suitable learning parameters adjusted during previous steps. The similar parameter selection procedure was used for all DMs.

3.4 Field Evaluation

3.4.1 VR Sprayer Hardware Configuration for Field Evaluation

A prototype VR sprayer hardware as defined in Esau et al. (2014) was modified by removing the front sensor boom and incorporating the cameras on the spray boom (Figure 3-8). The newly developed GDS for this project was tested in real-time field conditions using the modified VR sprayer hardware. The VR sprayer hardware consisted of four µEye colour cameras, a fan-less desktop computer, an eight channel computerized variable rate controller (VRC), eight solenoid valves (Delware Pump and Parts Limited, Delware, ON, Canada), and spray nozzles (Figure 3-8). The cameras were fixed on a 6.1 m long boom at a height of 1.22 m. The 3.5 mm lenses were setup to f/4.0 fixed aperture and infinity focuses. Additionally, a flow rate control mechanism consisting of Dickey John Land Manager-II controller (LMC) module (Dickey John Corp., Auburn, IL, USA), a Garmin® GPS 18x receiver (Garmin International Inc., Olathe, KS, USA), a flow meter, and a servo valve was used to regulate the flow rate according to travel speed. The spray nozzles used in evaluation procedure were flat fan TeeJet TP8004E (Spraying Systems Co., Wheaton, IL, USA) having a spray angle of 80^{o} and operated at a pressure of 275 ± 10 kPa. The sprayer boom was divided into eight sections of 0.76 m. A pair of solenoid valve and spray nozzle was mounted in the middle of each section with a uniform spacing of 0.76 m between two consecutive pairs. The nozzles were connected directly to solenoid valves with a 1.27 cm to 0.63 cm union joint in between them.

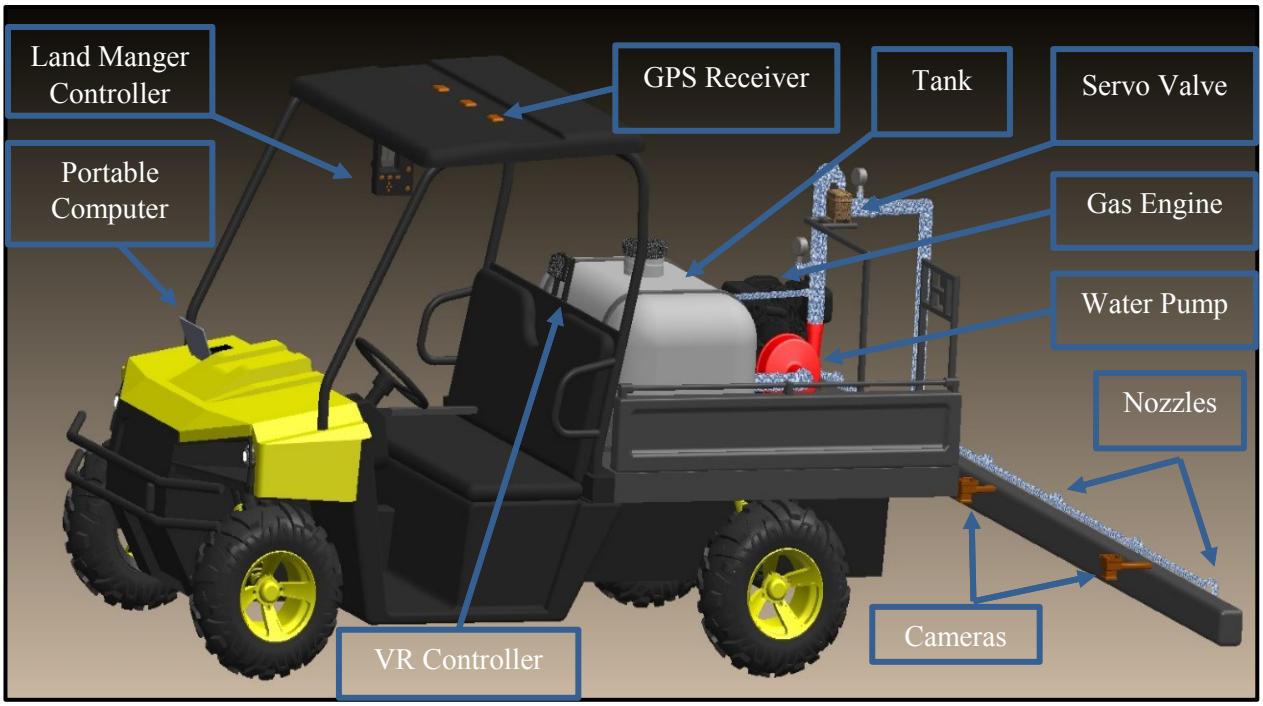

Figure 3-7: Schematic diagram of VR sprayer for field evaluation showing different components of machine vision and flow control system.

The centrifugal pump was operated by Honda® GX™ 160 (Honda Inc., NS, Canada) 3.57 kilowatt (kW) at 3600 rated rpm air cooled gasoline engine. The cameras were installed in between the two nozzles in a way that spacing between centerline of camera and centerline of nozzle is approximately 0.38 m and between two consecutive cameras is 1.52 m (Figure 3-9). This camera-nozzle agreement was utilized so that an AOI image can be used to control the two sections of boom. One half of an AOI image (three unit images) was utilized to control a nozzle at a time (Figure 3-10). The custom developed GDS was tested for acquiring and processing the AOI images along with goldenrod triggering signals sent to a U3-HV I/O module (LabJack Corp., Lakewood, CO, USA) through USB 2.0 cable.

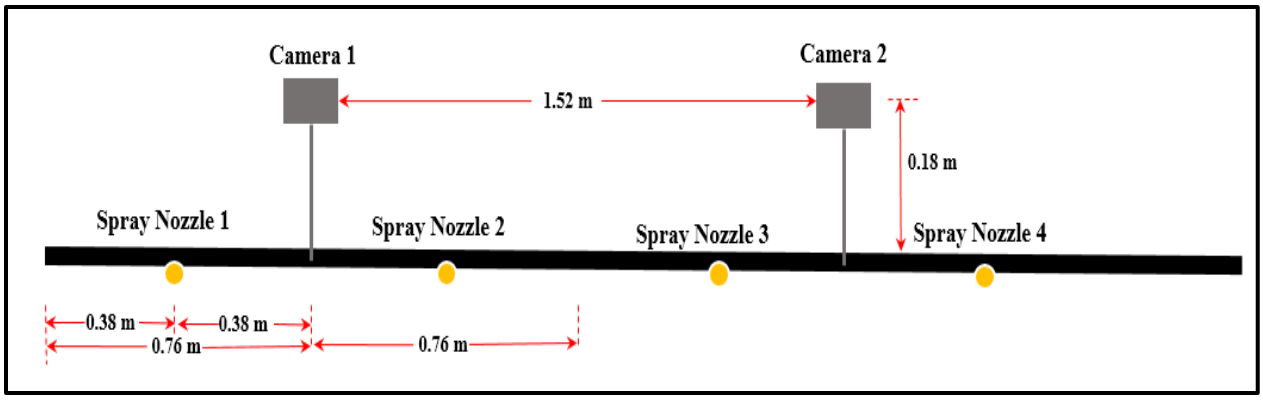

Figure 3-8: Schematic diagram showing camera and sprayer nozzle arrangement for the half boom.

The U3-HV module was capable of handling eight dedicated digital channels numbered 8 to 15 on its DB-15 connector. This unit was further interfaced with VRC through DB-15 standard connector cable to feed the 8-channels of VRC. The VRC was designed to pull a 5 V direct current (DC) signal coming from the U3-HV module to a 12 V (DC) signal. The solenoid valves were powered individually to open at specific time interval when needed. The VRC also shared its solenoid valve triggering signals with LMC to provide the information needed to adjust the flow rate using the servo flow control valve on the basis of number of nozzles opened and ground speed of UTV.

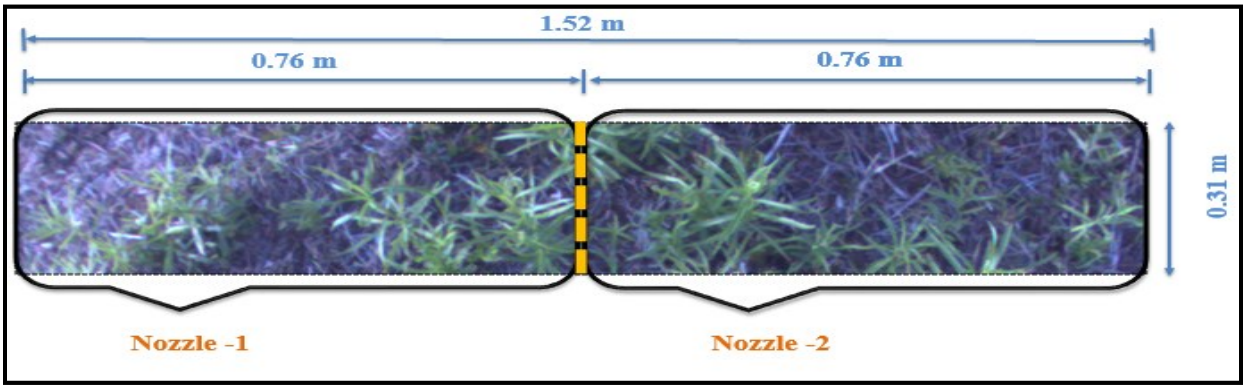

Figure 3-9: Experimental setup showing relationship between AOI Image size and nozzle control configuration.

3.4.2 Field Experiments during 2016

3.4.2.1 Fields Description

Performance of GDS was tested in two wild blueberry fields during the summer of 2016. The selected fields were Londonderry (45° 46' 59" N and 63° 33' 13" W) and North River II (45° 37' 45" N, 63° 22' 19" W). Both of these fields were in vegetative growth year during experiments and crop year in 2015. Among other weed species, fields contained goldenrod in mix canopy pattern. Results reported during 2016 were achieved by training the classifiers using only the image library of 2015. The DISCRIM and BP-ANN classifiers with the highest classification accuracy were used for field evaluation. The highest performing classifier obtained through DISCRIM procedure was quadratic.

3.4.2.2 Field Experiment 1

Two test tracks (6.1 m × 110 m), containing distinct goldenrod patches and occluded canopies were selected by surveying each field to compare and evaluate the accuracy of GDS (Figure 3-11, 3-12). The track boundaries and goldenrod patches were manually mapped from both tracks using a Hiper® lite+™ real-time kinematics (RTK) GPS receiver (Topcon positioning systems Inc., Livermore, CA, USA) for developing the representative maps of both fields using ArcGIS 10.2.2 (ESRI, Redlands, CA, USA). Eight goldenrod (targeted areas) and eight blueberry spots (non-targets) were randomly selected in each track and these locations were point marked using RTK-GPS. Sixteen water sensitive papers (WSPs) (Spraying Systems Co., Wheaton, IL, USA) were attached to plant canopies with the help of paper pins with their sensitive surface facing to sky. The GDS loaded with BP-ANN classifier was used to water spray these tracks in first run on June 4, 2016. The WSPs were collected after drying and new papers were placed at same locations. New WSPs were again water sprayed using a quadratic classifier and WSPs were again collected. Finally, WSPs were placed and sprayed on uniform application (UA) mode for

comparing the performance of individual classifier with UA application. Dried water sensitive papers were digitized and processed using a custom blue detection program (Precision Agriculture Research Program, Dalhousie University, NS, Canada) to detect colour change caused by water droplets. Percent area coverage (PAC) of sprayed targets in both blueberry and goldenrod areas were recorded for statistical analysis (Zaman et al., 2011). Similar experimental procedure was repeated in Londonderry field, except that tracks were first sprayed by using quadratic model followed by BP-ANN. The student paired t-test was utilized to calculate the significant difference between PAC of targets and non-targets in both VR and UA modes.

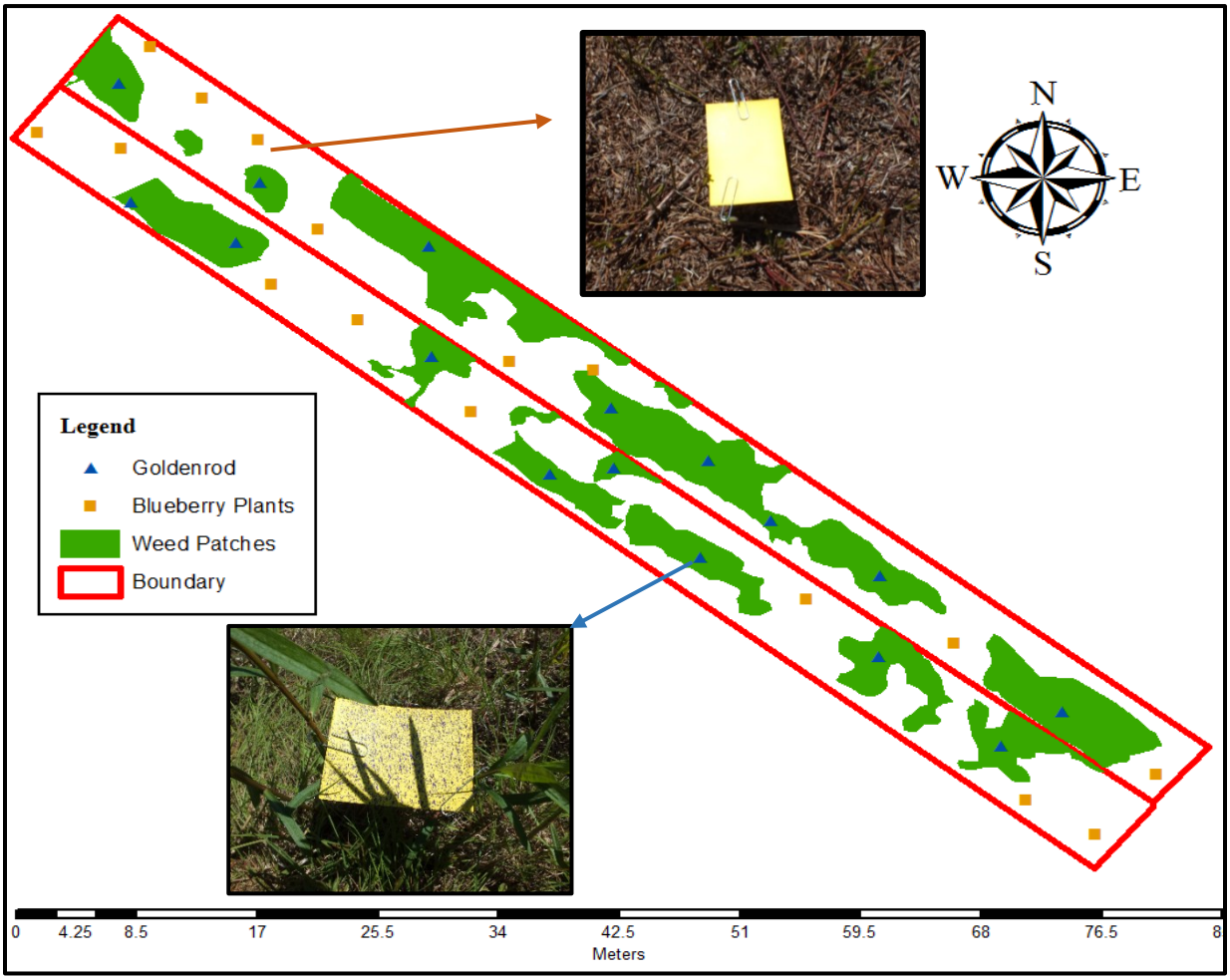

Figure 3-10-: Map of North River II test tracks showing goldenrod and wild blueberry points selected for spray applications with GDS.

Figure 3-11: Map of Londonderry test tracks showing goldenrod and wild blueberry points selected for spray applications with GDS.

3.4.2.3 Field Experiment 2

Same test tracks in both wild blueberry fields were used to compare the performance of two different classifying models. Weed maps were generated by using previously marked goldenrod patches from tracks. The test tracks in Londonderry and North river II were sprayed with BP-ANN and quadratic classifier, respectively, using a Lazer™ blue coloured non-permanent spray pattern indicator herbicide dye (Bluewater Chemgroup Inc., Fort Wayne, IN, USA) on June 12, 2016. Blue marked patches were mapped using RTK-GPS and sprayed map was generated using ArcGIS 10.2.2. These tracks were again sprayed by switching models with same blue dye marker on June 15, 2016. The new marked patches were again mapped and sprayed maps were generated. Sprayed maps from BP-ANN and quadratic models were superimposed on the weed maps generated before dye spray separately using ArcGIS package. The coverage area (CA) of different sprayed polygons in sprayed maps were exported form ArcGIS and two-sample t-test was performed to statistically analyze the performance of both classifiers. The superimposed maps were also compared subjectively by placing side by side to look for any over and under-sprayed areas. The potential and actual chemical savings were also calculated by using the goldenrod area and sprayed area (Esau et al., 2014), respectively.

$$Potential\ Chemical\ Savings\ (\%) = 100 - \frac{Goldenrod\ Area}{Total\ Area} \times 100 \quad (3\text{-}36)$$

$$Actual\ Chemical\ Savings\ (\%) = 100 - \frac{Sprayed\ Area}{Total\ Area} \times 100 \quad (3\text{-}37)$$

3.4.2.4 Statistical Analysis

PAC of two different VR modes (BP-ANN and quadratic) was compared with UA mode individually by performing paired t-test using Minitab 17. Collected data were tested for normality

assumption by performing Anderson-Darling (AD) normality test at significance level of 5%. The randomization of treatments within selected fields assured the independence of error terms.

Performance of two different classifiers was evaluated by comparing CA of two different sprayed maps, while treating the individual polygon as an observation unit. Normality was checked by using AD test at 5% significance level and independence was achieved through randomization. The equal variance of two data populations was tested by calculating the ratio of sample standard deviations (with larger sample standard deviation in numerator). Validation of equal variance assumption led to analyze the CA by using t-distribution with pooled variance (Sp^2).

3.4.3 Field Experiments during 2017

3.4.3.1 Field Selection and Experimental Design

The BP-ANN and quadratic classifiers were compared with UA and non-treated control (CN) applications by setting field experiments at Portapique (45° 24' 28.20" N, 63° 43' 30.65" W) and Robie Glenn (45° 27' 3.63" N, 63° 25' 9.87" W) fields, Nova Scotia, Canada in May of 2017. These fields were mature, commercial wild blueberry fields, receiving mowing from at least last five years and were in vegetative growth year during experimentation. Experiments were setup as completely randomized design (CRD) to examine the effect of four different treatments (BP-ANN, Quadratic, UA and CN) on goldenrod damage. The experiment was replicated six times for each treatment in both fields and a plot size of 6.1 m × 5 m was used to collect the response data. A tank mix of 0.3 L ha^{-1} Callisto® 480SC (480 g L^{-1} Mesotrione) herbicide (Syngenta Canada Inc., Guelph, ON, Canada), 0.4 L ha^{-1} Agral® 90 (92% Nonylphenoxy polyethoxy ethanol) non-ionic spreading agent (Syngenta Canada Inc., Guelph, ON, Canada), and a water volume of 186.4 L ha^{-1} and was used to spray the test plots at a grower's rate of 187.1 L ha^{-1}. The GDS with two different classifiers and UA mode were used to apply the tank mix of Callisto® in test plots. Both BP-ANN and

quadratic classifiers used for 2017 experimentation were trained and laboratory tested using image libraries developed during 2015 and 2016 from different fields.

3.4.3.2 Data Collection

Goldenrod damage caused by the Callisto® was evaluated by recording goldenrod stem height (SH) and damage rating (DR) data, 21 days after treatment (DAT). The SH (cm) was measured by randomly selecting the 25 damaged goldenrod stems across each treated plot and averaged out to represent a single plot. The DR was measured subjectively on whole-plot basis by ranking the damage on a scale of 0 to 100, where 0 represented no visible damage and 100 as a complete death of above ground shoots (Wu and Boyd, 2012). The colour change from green to pale yellow caused by the goldenrod damage due to Callisto® application was quantified by using green ratio algorithm (Chang et al., 2014). The images were acquired from six randomly selected points in each plot using Fujifilm FinePix HS30EXR (Fujifilm, Mississauga, ON, Canada) 16-megapixel digital colour camera with a fixed aperture of f/3.6 by pointing it downward at a height of 0.75 m above the ground. The exposure, gain and white balance were on automatic mode during the image acquisition. A wooden quadrat of 25 cm × 25 cm was placed on selected points to mark the area of interest. There were other green weeds at some of the selected points and therefore, area of interest marked with quadrat was hand-weeded by pulling their stems to remove all green weeds except goldenrod. The percentage of green pixels (PGP) in quadrat region of images taken from four different treatments (BP-ANN, Quadratic, UA and CN) was calculated by green-ratio algorithm with manually obtained threshold of 90 (Esau et al., 2014).

3.4.3.3 Statistical Analysis

One-way analysis of variance (ANOVA) was used to test the effect of different treatments on collected data of SH and PGP using Minitab 17. Normality of error terms was checked by developing the normal probability plot (NPP) of error terms. The AD test at 5% level of

significance was performed on NPP of error terms. Constant variance was checked by plotting the residuals against fitted values. Randomization of treatments within selected fields assured independence of error terms. Least significant difference (LSD) test was used as multiple means comparison (MMC) method to identify the means significantly different from other at a level of 5%.

The DR data was analyzed by performing a rank-based, non-parametric Kruskal-Wallis H test using Proc Npar1Way procedure in SAS 9.3. Measurement of the DR on a 100-point scale assured the ordinal level assumption. Application of Callisto® tank mix with three different treatments helped to meet the assumption of more than two categorical, independent treatment populations. Dunn-Bonferroni test was performed as post-hoc to identify significantly different DR means at a level of 5%.

CHAPTER 4: DEVELOPMENT OF A GRAPHICAL USER INTERFACE BASED GOLDENROD DETECTION SYSTEM WITH AN EMBEDDED OPTIMIZED COLOUR CO-OCCURRENCE MATRIX ALGORITHM FOR REAL-TIME SPOT SPRAY

4.1. Introduction

The spatio-temporal variability of weed flora across wild blueberry fields offers an advantage of applying the agrochemicals on an as-needed basis. The wild nature of crop is responsible for inherent variability in terms of weed species, their distribution, and fruit productivity as compared to cultivated crops (Kennedy et al., 2010). Newly developing fields typically possess randomly distributed weed patches and bare spots varying from 30% to 50% of total field area (Zaman et al., 2008). The unique characteristics of wild blueberry cropping system emphasize the need to develop cost-effective and reliable solutions for spot application of agrochemicals on an as-needed basis.

Several studies indicated that a mathematical process of extracting, characterizing, and interpreting leaf texture based tonal information of agronomic images has great potential to differentiate weeds from crops (Meyer, 2011). Textural features provide some botanical information, such as leaf venation, leaf pubescence, and leaf surface coarseness for detecting plant and weed phenotypes (Neto and Meyer, 2005). Numerous textural analysis algorithms have emerged over the last few decades to retrieve different levels of information from underlying scenes (Haralick, 1979). Gray level co-occurrence matrices (GLCMs) and CCMs followed by extraction of statistical features (Haralick et al., 1973) are widely used textural information retrieval techniques for agricultural applications (Shearer and Holmes, 1990; Burks et al., 2001; Pydipati et al., 2005; Roy et al., 2006; Tahir et al., 2007; Kim et al., 2009) and have proven to have significantly higher object recognition rates (Burks et al., 2005; Tahir et al., 2007).

Chang et al. (2012a) detected bare spots, wild blueberry plants, and weeds using CCMs. Research concluded that the process of constructing CCMs and extracting textural features is computationally intensive. They recommended 64-bit programming or hardware parallel computation for the commercial application of these algorithms in VR sprayers. The computational overheads can be minimized by first studying and analyzing the factors in time space responsible for the high computational loads. This analysis will then help in the appropriate selection of the parameters for optimized performance and real-time application of these algorithms in commercial VR sprayers.

Many agricultural researchers developed the GUIs for continuous real-time sensing, mapping, monitoring and updating the sensed data (Schumann and Zaman, 2005; Zaman et al., 2008; Swain et al., 2010; Zaman et al., 2010; Chang et al., 2012b; Farooque et al., 2013). Schumann and Zaman (2005) monitored citrus tree canopy area and height by using a GUI coupled with an array of ultrasonic sensors and differential global positioning system (DGPS). Zaman et al. (2010) developed a GUI for reading and storing the slope sensor data in a database. Chang et al. (2012b) used two digital cameras and GUI to estimate the wild blueberry yield. This GUI helped to monitor the performance of the cameras by providing the on-screen updates of processed images along with necessary camera and GPS communication parameters. A similar concept can be extended to develop a GUI capable of acquiring, saving, and processing continuous timed image streams from multiple cameras in real-time along with decision-making capabilities for the targeted application of agrochemicals on goldenrod. Moreover, the imaging system should be monitored and corrected for any errors and loss of connections during image acquisition process.

Therefore, the specific objective of this chapter was to develop a user interface based GDS with an embedded optimized colour co-occurrence matrix algorithm in C# for image acquisition

and processing in real-time and to study the intrinsic and extrinsic parameters influencing the real-time application of CCMs for wild blueberry fields.

4.2 Materials and Methods

4.2.1 Development of Goldenrod Detection System

The custom image acquisition GUI program was upgraded from Figure 3-1 to accompany the CCM based textural analysis algorithm for extracting the CCM features in real-time, to model these features in meaningful way in terms of goldenrod and wild blueberry detection, and transfers the 5 volt weed or plant triggering signals through a digital U3-HV I/O unit to VRC (Figure 4-1). This upgraded program was capable of displaying the processed AOI images in the real-time and to provide the on-screen updates of sprayer nozzle status accordingly. A "Stop" button was also added to the GDS program to stop and resume the image acquisition, processing and other functionalities associated with camera. Other controls added, included the channel control, foam marker control, and artificial lighting control protocols.

The AOI image data coming from each camera in computer memory were copied to the new instances of the "Bitmap" class with pixel format set to 24bpp. The "RGB2HSI" method of "Colour Conversion" class was called to convert the contents of copied image data. The "CCM" class was responsible for dividing an AOI image into six unit images, creating eighteen CCMs for HSI colour planes, normalizing these CCMs, and extracting a set of 13 features from an individual CCM. The angular relationship of 0^{o}, a displacement vector of 1 pixel, and 256 intensity levels were selected in this study for CCM construction. A process of extracting a set of 13 features was repeated thrice for CCMs resulting in a total of 39 features from an individual unit image. The comprehensive detail of CCMs, list of textural features, and their definitions are presented in Chapter 3. This real-time GDS integrated the reduced list of CCM features according to the results

of STEPDISC function to minimize the processing time and enhance the overall classification accuracy. Instead of looping class call over four cameras, the GDS called these classes on different worker threads to minimize processing time for real-time application. The processed AOI images from all cameras were displayed on-the-screen using picture box controls and all contents of image were disposed of thereby enabling the program to process new incoming AOI image data.

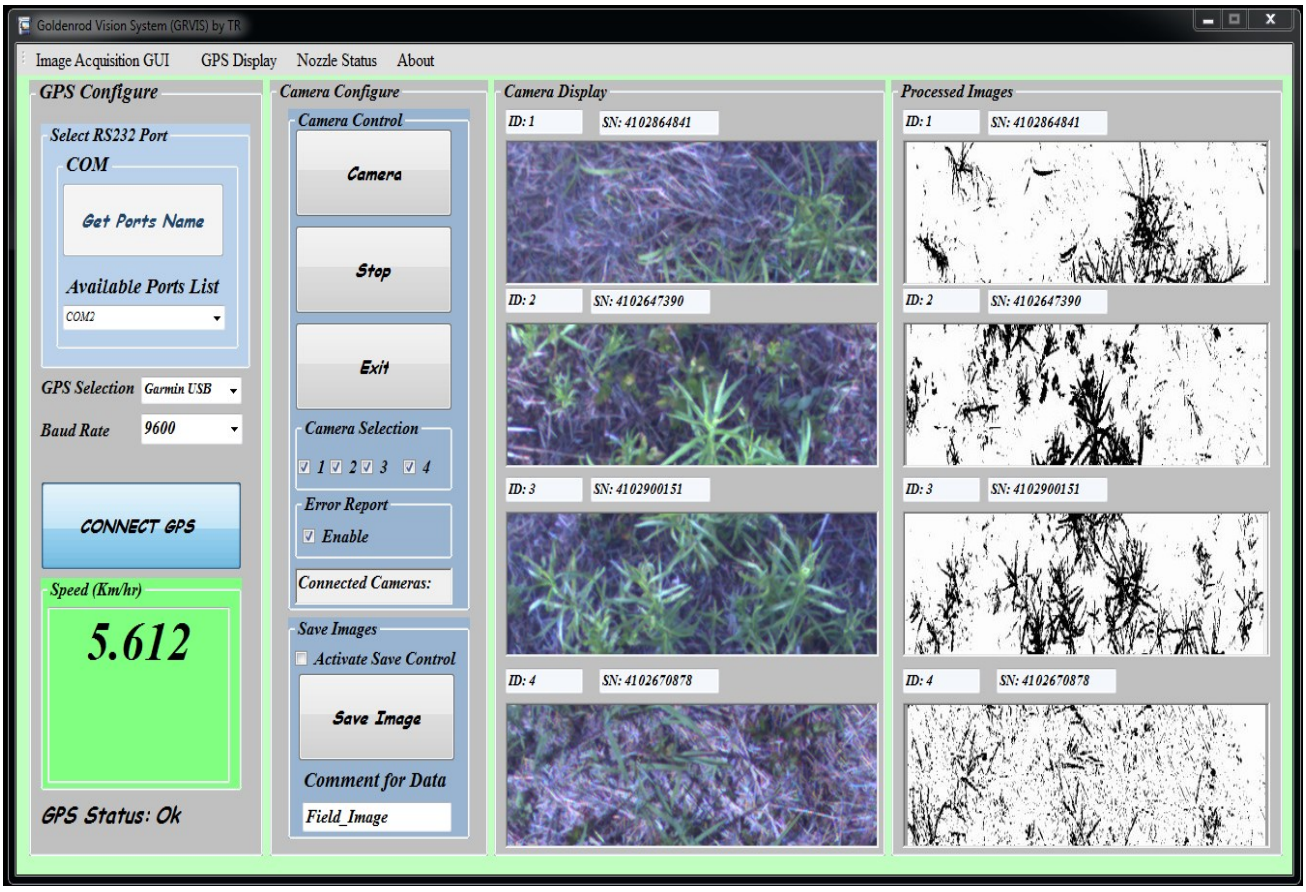

Figure 4-1: Windows based GDS showing real-time camera images display, processed images, controls, ground speed, and camera diagnostics.

Two streamlined variants of GDS were developed to accommodate quadratic and BP-ANN based classifying criterions. The basic data handling flow and processing layout of both variants were same except the decision rules (Figure 4-2). The quadratic GDS directly included the mean

feature values and within group covariance matrices of GR and WBB classes to model the CCM features of new real-time observation. This program solved a quadratic model by calculating the generalized square distances of observation from both GR and WBB. These distances decided the category (GR or WBB) on the basis of smallest distance from particular class. A Dynamic link library (.dll) file extracted from the Peltarion Synapse was included in the BP-ANN based GDS. This library contained the definitions and all necessary parameters of a trained model. The CCM features were handed to this library in matrix format and a two elemental output (GR and WBB) were retrieved. These classifying criterions were solved for six unit images extracted from an AOI image and the process was repeated for all the cameras by both these variants. The results of classifiers development are shown in chapter 5.

The outputs of classifying models were compared for the GR and WBB using "if-else" logical block for all unit images and results were stored in a six elemental decision unit array according to the following rule:

$$\text{Decision Unit} = \begin{cases} 1 & \text{if GR} > \text{WBB} \\ 0 & \text{else} \end{cases} \tag{4-1}$$

Three decision units representing three unit images (One-half of an AOI image) were used to control an individual nozzle. Two counters checked and stored the sum of three decision units for an individual nozzle by comparing the decision unit values. These counters were finally used for switching the nozzle to "ON" or "OFF" state by using the following comparison condition:

$$Nozzle\ State = \begin{cases} \text{Open} & \text{if Counter} > 1 \\ \text{Close} & \text{else} \end{cases} \tag{4-2}$$

In order to physically trigger the nozzles, a U3-HV output control protocol was added in the GDS. An opening signal was sent through USB port to set up the communication rule between

computer and U3-HV module. This protocol automatically detected the USB location of module while communicating. The eight channels of this module were individually controlled by using (Eq. 4-2) along with the camera ID. The even and odd numbered channels were controlled by first and second counter separately. All parameters of this protocol except the communication signal were disposed of after sending the power pulse to VRC.

The serial communication control for interfacing the GPS was updated to accommodate any variations in COM port names available on different computers. A button on the GUI was provided to query the registry of current computer for a list of valid serial port names and to add them on the GUI. The default port settings and in case the user manually typed the port name was set to first port available in list. The error handling mechanism for serial communication was also improved by adding the new exception handlers for port detection, port name change, and GPS signal outage during serial communication. The channel, foam marker, and artificial lighting controls included all necessary signal triggering codes to perform the respective operations. They were checked and tested in laboratory for their respective use but were not operated in real-time applications because of the limited number of channels (8) available on VRC.

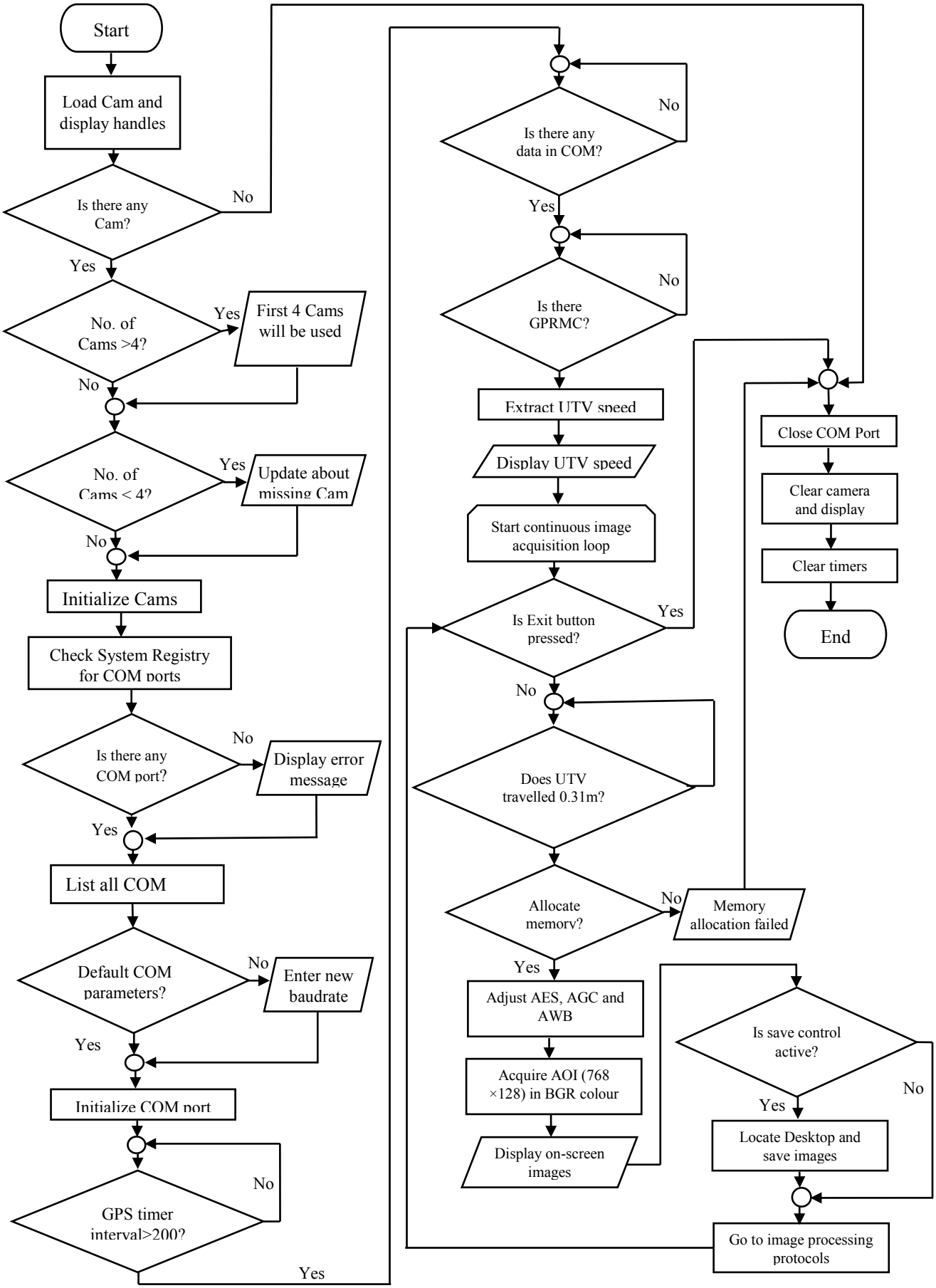
Start
Load Cam and display handles
Is there any Cam?
No
Yes
No. of Cams >4?
Yes
First 4 Cams will be used
No
No. of Cams < 4?
Yes
Update about missing Cam
No
Initialize Cams
Check System Registry for COM ports
Is there any COM port?
No
Display error message
Yes
List all COM
Default COM parameters?
No
Enter new baudrate
Yes
Initialize COM port
GPS timer interval>200?
No
Yes
Is there any data in COM?
No
Yes
Is there GPRMC?
No
Extract UTV speed
Display UTV speed
Start continuous image acquisition loop
Is Exit button pressed?
Yes
No
Does UTV travelled 0.31m?
Allocate memory?
No
Memory allocation failed
Yes
Adjust AES, AGC and AWB
Acquire AOI (768 ×128) in BGR colour
Display on-screen images
Is save control active?
No
Yes
Locate Desktop and save images
Go to image processing protocols
Close COM Port
Clear camera and display
Clear timers
End

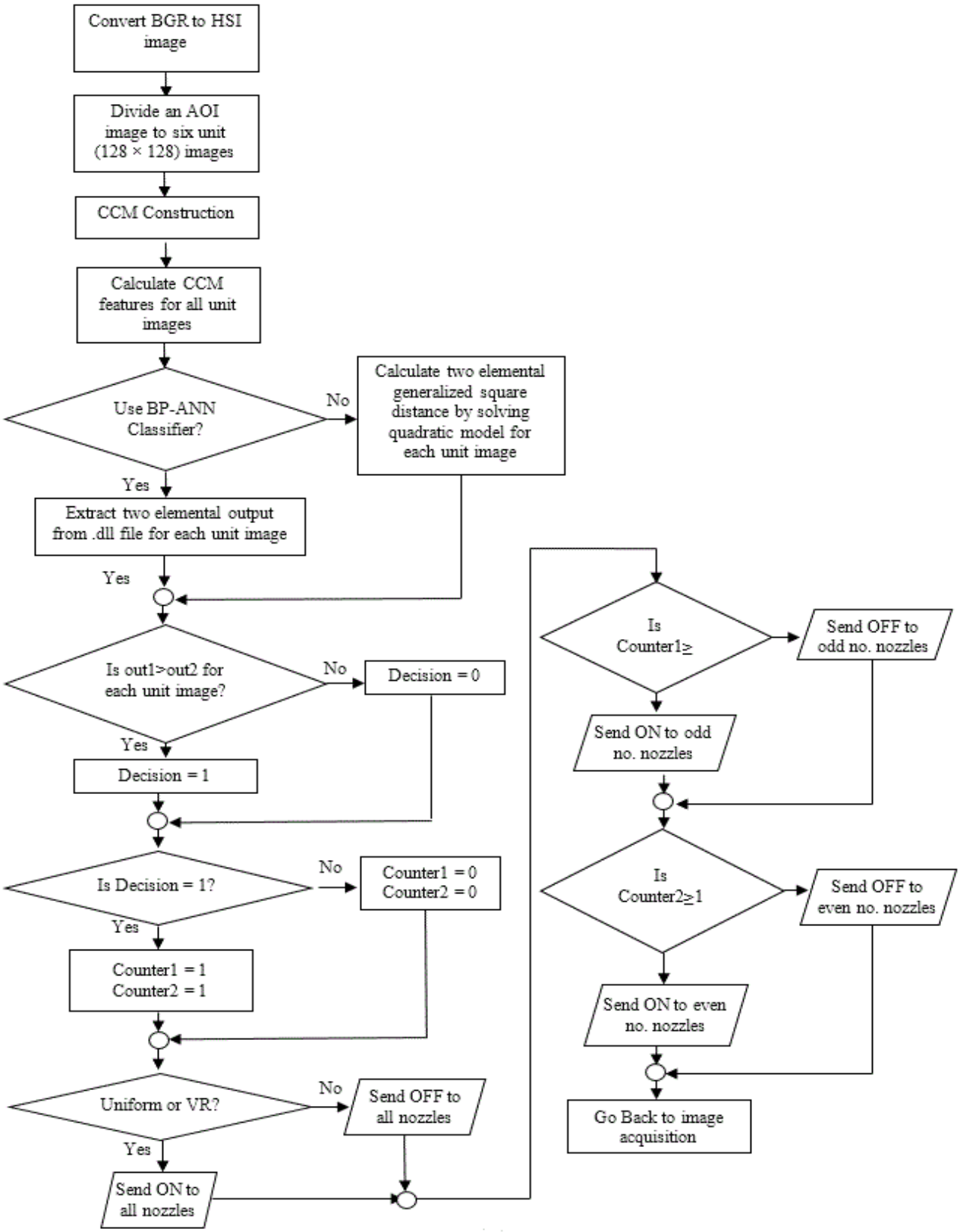

Figure 4-2: Flowchart of GDS from image acquisition and goldenrod detection to herbicide application.

4.2.2 Factors influencing the real-time application of CCMs

The real-time application of CCMs can be affected by intrinsic and extrinsic parameters. Intrinsic parameters include image size and intensity levels from an individual CCM. Extrinsic parameters are related to the performance of particular computer hardware/internal architecture and different methods available in any particular programming language/environment to perform a similar operation. The following intrinsic and extrinsic parameters were compared in this study.

4.2.2.1 Image Reading from RAM- The Pointer Arithmetic

Three different methods (Marshal.copy, unsafe pointers, and get pixel) are available in C# programming language to access image data contained in the RAM of the computer. A laboratory experiment was conducted to select the best method for accessing real-time image data. The method was selected on the basis of performance in terms of time and overall safety of code. In order to test their performance, three different codes were written to read an AOI image (768 × 128) data from RAM for three different methods separately. The AOI image set with 256 intensity levels was used for this analysis. The time difference (%) and speed up ratio of the particular image reading method were calculated with reference to the average time of "get pixel" method.

The first code was written to utilize the Marshal.copy method for copying the image data to a managed 1D array. The "BitmapData.LockBits" method was utilized to lock the bits of the bitmap image in the memory. This method was parameterized by specifying the image lock mode as "ReadWrite", and pixel format similar to source image. The "BitmapData.Scan0" property was utilized to define a memory handler (IntPtr) to get the address of first pixel data in an AOI image. The copied image data were utilized to develop HSI image. After manipulating the image contents, the complete information was handed back from 1D array to IntPtr to dispose of image contents by setting all the controls to "null". The second code was written to perform pointer arithmetic in

unsafe context to handle the image data in RAM. This method had some similarities with the Marshal.copy in terms of locking the image bits and utilizing the Scan0 property. The memory handler (IntPtr) in this case was changed to a pointer by using an unsafe keyword to perform pointer arithmetic. This pointer was utilized to store the address of particular pixel during new HSI image development. The image contents were released after extracting the desired colour information. The third code utilized the get pixel method of "Colour" structure to access the colour information contained in individual pixel of an image. The parameters for this method were set to the coordinates (x, y) of each pixel. Two "for" loops were utilized for reading the number of pixels in image width (x) and height (y). This extracted colour information was utilized to generate HSI image by using the set pixel method.

The processing time was measured by using "elapsed milliseconds, elapsed ticks, and date-time" code profiling techniques to accurately measure the execution time. All other methods measured the execution time in ms directly except elapsed ticks. This method counted the number of elapsed ticks and was utilized as it provided the precise smallest measurement of processing time. The "frequency (number of ticks/second)" field was utilized to convert the elapsed ticks values in real world time (ms) by dividing the elapsed ticks with frequency. The codes were written to accommodate any frequency fluctuations caused by CPU clock speed due to power saving modes taken by operating system. Moreover, the computer was connected to continuous power supply in order to avoid any possible fluxes caused by low battery power. During the processing of individual image, codes checked the frequency of CPU, counted the elapsed ticks for all timers and generate a database of this information by writing it in a CSV file along with image location by processing images in batch file handling mode.

4.2.2.2 Selection of Intensity Levels and Computational Time

The dimensions of CCMs were governed by the maximum intensity levels of pixels in the image. More levels would mean more accurate textural information, with a bigger size CCM and increased computational cost. In order to test the effect of intensity levels on computational complexity, an experiment was performed by modifying the QGDS for quantizing the eight-bit images down to three bits, converting the BGR images to HSI images, and constructing the CCMs. The Marshal.copy method was utilized for this test because of its fast processing results. The displacement vector and orientation angle during this experiment were fixed to the 1 and 0°, respectively. Six different intensity levels (8, 16, 32, 64, 128, and 256) were included in this study, while keeping the image size (128 × 128) constant. The extraction of one-sixth portion of an AOI image (768 × 128) set resulted into the use of 2244 unit images (128 × 128) for this experimentation. The computational time calculation task was broken into three sections and three stopwatch components were created to precisely measure the time for HSI colour conversion, CCMs construction, and textural features extraction. The elapsed ticks property was utilized to count the number of elapsed ticks for all timers. The intensity level with minimum execution time was utilized as a benchmark to calculate the average time difference (%).

In order to examine the effect of intensity levels on classification accuracy, textural features were extracted from an image library of 2112 unit images (128 × 128). This image library consisted of 1229 goldenrod (weed) and 883 wild blueberry (crop) images. The image library was divided into two datasets containing 70% of data for developing and training a model and 30% for validating the model. The QGDS program for different intensity levels was executed to extract the 39 textural features by processing the images in the library. The SAS PROC DISCRIM procedure was used for training the different quadratic models based on different intensity levels. All 39

features from three different colour planes were used for training the classifier, and results were reported for both training and test data.

4.2.2.3 Effect of image size on processing time

The effect of image size on the computational time was analyzed by processing the different sized images with QGDS. The image acquisition GUI was modified to acquire the full frame images (1280 × 1024) thereby covering the wide variety of image sizes. The full frame field images were cropped into different sizes (256 × 256, 512 × 512, and 1024 × 1024) along with different unit images (16 × 16, 32 × 32, 64 × 64, and 128 × 128) extracted from AOI images. The time required for colour conversion, CCMs construction, and extraction of 39 features were measured by using elapsed ticks property of stopwatch component. The intensity levels were fixed to 256 during this experimentation. The average time difference (%) of the particular image size was computed with reference to the image size with the least execution time.

The classification accuracy for different sized unit images (32 × 32, 64 × 64, and 128 × 128) was studied by using a set of 1424 images. There were 484 goldenrod and 484 wild blueberry images in training data, while the test data contained 200 goldenrod and 256 wild blueberry images. The QGDS program was used for extracting textural features from different sized unit images. The SAS PROC DISCRIM procedure was again used for training different quadratic models based on different image sizes. All 39 features from three different colour planes were used for classifier training.

4.2.3 Image Reading Experimentation Test Setup

A set of 2244 AOI images (768 × 128 pixels) and a set of 2244 full frame images (1280 × 1024) were utilized to study the effect of different intrinsic and extrinsic parameter included in this

study. The image set contained a wide variety of real field agronomic images, varying from dense lush green images, with more information confined in the green channel to very sparse images, mostly covering bare soil or twigs and few green plants (Figure 4-3). To ensure that test results were not biased by any particular computer hardware environment, the experiment was performed on four different machines equipped with a 64-bit Windows-7 operating system (Table 4-1). These choices were made to ensure that performance differences occurred due to the algorithmic differences rather than other machine factors.

Table 4-1: Computer architecture information about four different test machines.

CPU Type	CPU Chipset	Clock Speed	Cache			Memory	Bus Speed	RAM Type
			L1	L2	L3			
		(GHz)	(KB)	(KB)	(MB)	(GB)	(MHz)	
Core i5 4200 M	Haswell	2.50	64	512	3	4	1600	DDR3
Core i7 3740QM	Ivy Bridge	2.70	128	1024	6	8	1333	DDR3
Core i7 860	Lynnfield	2.80	128	1024	8	4	1333	DDR3
Core i7 6700K	Skylake	4.00	128	1024	8	8	2133	DDR4

The L1, l2, and L3 indicates level-1, level-2, and level-3, respectively.

(a)

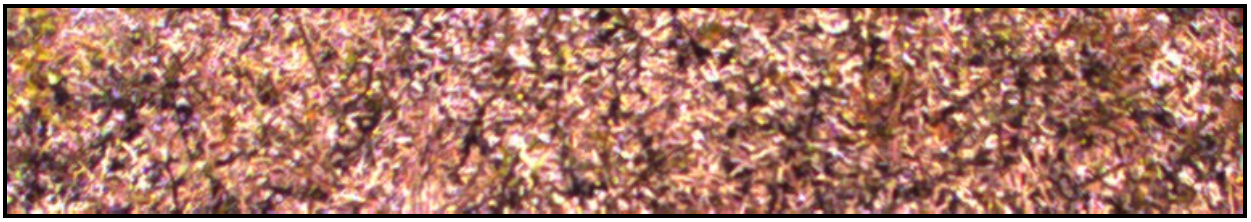

(b)

Figure 4-3: Images used for experimental analysis, (a) dense lush green image and (b) sparse image with twigs and soil.

4.2.4 Statistical Analysis

One-way Analysis of variance (ANOVA) was performed to study the effect of different extrinsic parameters individually on execution time using Minitab 17. The significantly different time measurement means were determined by performing the Tukey's honestly significant difference (HSD) test as multiple means comparison at a significance level of 5%.

4.3 Results and Discussion

4.3.1 Comparison of Execution Time for Image Reading

The time required to read the image from computer RAM and to convert the acquired BGR colour image to HSI was measured using three different codes. The results of image reading experiment indicated that maximum time with elapsed milliseconds method was 154.68 ms taken by the get pixel method, followed by 8.00 ms with unsafe pointers, and 2.61 ms with Marshal.copy method, respectively (Table 4-2). The time differences between unsafe pointers and Marshal.copy methods were found to be 94.82% and 98.31%, respectively, from get pixel method. The maximum speed-up ratio of 59.26 was observed for Marshal.copy method followed by a speed-up ratio of 19.34 for unsafe pointers. A similar experiment was performed with two other benchmark timer routines to minimize the biases associated with particular method or property. The results of these experiments showed similar results (Table 4-2).

Table 4-2: Summary of execution time for three different image reading methods along with three different code profiling techniques (core i7 6700K).

Timer Routines	Image Reading Method						
	Get Pixel	Unsafe Pointers			Marshal.Copy		
	Time (ms)	Time (ms)	Difference (%)	Speed Up Ratio	Time (ms)	Difference (%)	Speed Up Ratio
Milliseconds	154.68	8.00	94.82	19.34	2.61	98.31	59.26
Date Time	155.2016	8.2727	94.66	18.76	3.2395	97.91	47.90
Elapsed Ticks	155.1836	8.2161	94.70	18.88	3.1766	97.95	48.88

The real drawback of utilizing get pixel method was the higher time required to extract the colour information contained in an image resulting in a poor selection for real-time applications. The Marshal.copy method took least time, with the highest speed-up ratios making it a suitable choice for real-time applications. The unsafe pointer method can be a good alternative of Marshal.copy method from a speed-up ratio perspective, but this code was not being verified by Common Language Runtime (CLR) during code execution. This can result in an unexpected crash of program due to non-trusted assembly codes generated from unsafe codes (C# Programming Guide, 2015).

Results of different time measuring routines revealed that time measured by these three methods was approximately the same. However, the resolution of elapsed milliseconds method was found to be insufficient to measure the elapsed period of microseconds. The other two routines had nanoseconds resolution, therefore resulting in more precise elapsed time measurement. However, results obtained from date-time method with code implemented on a high-speed

computer (core i7 6700K) showed the risk of inaccurate measurements associated with this method (Table 4-3). This inaccuracy may be due to fluctuation of computer timer clock and inaccuracy of computer timer synchronization with official Gregorian calendar. The elapsed ticks method was observed to be accurate code profiling tool among these methods along with a high resolution of about 200 nanoseconds.

Table 4-3: Summary of the execution time of three different image reading methods using three different code profiling techniques on Core i7 6700K architecture.

Image No.	Image Reading Method								
	Get Pixel			Unsafe Pointer			Marshal.Copy		
	Milli -Sec.	Date Time	Elapsed Ticks	Milli -Sec.	Date Time	Elapsed Ticks	Milli -Sec.	Date Time	Elapsed Ticks
1.	162	156.0001	162.5485	9	0.0000	9.0486	4	0.0000	4.5556
2.	156	156.0001	156.8104	8	15.6001	8.8158	3	0.0000	3.1007
3.	155	156.0001	155.1961	8	0.0000	8.3920	4	0.0000	4.0644
4.	157	156.0001	157.6444	8	0.0000	8.0673	2	15.6001	2.8812
5.	161	156.0001	161.8349	8	14.6090	8.2392	3	0.0000	3.0563
6.	154	156.0001	154.9695	8	0.0000	8.2678	2	0.0000	2.4479
7.	157	156.0001	157.3792	8	15.3012	8.1670	3	0.0000	3.0427
8.	159	156.0001	159.5225	8	0.0000	8.3465	4	0.0000	3.0384
9.	155	156.0001	155.7147	8	0.0000	8.0919	3	15.6001	3.4489
10.	155	156.0001	155.4289	8	15.6001	8.3619	3	0.0000	3.1776

A consistent relative performance was shown by three image reading codes on each test platform. The execution results of different image reading codes on four different computer architecture (Table 4-1) showed that core i7 6700K architecture took the least time for manipulating and converting the colour information contained in any image (Table 4-4). This is due to high-end CPU clock speed, better processor architecture (sixth generation- Skylake series) and the highest front-side bus speed (FSB) causing minimal memory data delivery delays. Despite having higher clock speed and faster processor, the timing results on core i7 860 followed that of core i5 4200M, with the former typically larger than the later. The possible reason for this time lag can be the relatively lower FSB of core i7 860 architecture causing this CPU to spend a significant amount of time waiting for the data to arrive from computer memory. The maximum processing time was taken by core i7 3740QM architecture among all other platforms included in this study. Possible reason could be a better CPU architecture of the core i5 4200M (fourth generation-Haswell series) as compared to the core i7 3740QM processor (third Generation-Ivy Bridge series).

Table 4-4: Execution timing measurements for four different computer architectures.

	Image Reading Method				
	Get Pixel	Unsafe Pointers		Marshal.Copy	
	Time (ms)	Time (ms)	Speed Up	Time (ms)	Speed Up
Core i7 6700K					
Milliseconds	154.68	8.00	19.34	2.61	59.26
Date Time	155.2016	8.2727	18.76	3.2395	47.90
Elapsed Ticks	155.183691	8.216092	18.88	3.176588	48.88
Core i5 4200M					
Milliseconds	224.66	12.72	17.66	5.40	41.60
Date Time	225.1653	13.2587	16.98	5.7276	39.31
Elapsed Ticks	225.163101	13.238470	17.00	5.710997	39.42
Core i7 860					
Milliseconds	275.63	17.56	15.69	8.03	34.32
Date Time	275.8567	17.9849	15.33	8.4559	32.62
Elapsed Ticks	275.864002	18.00735	15.26	8.448458	32.65
Core i7 3740QM					
Milliseconds	315.44	17.08	18.46	9.19	34.32
Date Time	315.9631	17.78292	17.76	9.5727	33.03
Elapsed Ticks	315.944302	17.731011	17.81	9.602078	32.90

4.3.2 Selection of Intensity levels and Classification Accuracy

The effect of image intensity levels on the processing time was investigated by quantizing the eight-bit images down to three-bits along with all other steps involved in CCM construction and feature extraction (Table 4-5). Results showed that average total time required for performing

a complete process from colour conversion to features extraction reduced with a reduction in intensity levels. The mean total time reduced from 10,650.264 µs to 534.718 µs with down quantization of eight-bit (256 levels) image to three-bit (8 levels). Time during colour conversion was found to be significantly higher (505.261 µs) for 256 levels when compared to other intensity levels. The colour conversion time for images with intensity levels of 16, 32, and 64 were not found to be significantly different at a level of 5%. The least time (310.503 µs) for colour conversion operation was observed for images with 8 intensity levels.

Table 4-5: Execution time with different intensity levels and a fixed image size of 128 × 128 pixels on core i7 6700K.

Intensity Levels	Mean Time (µs)				Difference
	HSI Conversion	Co-Occurrence Matrix	Textural Features	Total	(%)
8	310.503 d	212.694 d	11.521 f	534.718 f	------
16	316.066 c	214.106 d	37.556 e	567.728 e	6.17
32	316.086 c	222.688 d	142.803 d	681.578 d	27.46
64	316.481 c	253.599 c	560.590 c	1130.670 c	111.40
128	319.837 b	472.803 b	4234.359 b	5026.999 b	840.12
256	505.261 a	1330.402 a	8814.601 a	10,650.264 a	1891.75

Means with no letter shared in same column are statistically different at p=0.05

Results of Tukey's HSD test showed non-significant difference between mean CCMs construction time for intensity levels of 8, 16, and 32. A clear increment in the CCMs construction time was observed for images with 64, 128, and 256 levels. The increased time was due to larger sized CCMs caused by more intensity levels. The computational time for feature extraction was

found to be highly dependent on intensity and decreased by a factor of 765 as intensity levels were reduced from 256 to 8. The reduced iterations resulted from lower intensity levels caused QGDS to loop relatively fewer times over CCMs to extract the features.

The analysis of weed-crop classification accuracy showed an improvement in accuracy with increase in CCM intensity levels (Table 4-6). It was observed that intensity levels from 8 to 32 achieved good overall accuracy (>89%) on training data, while was not able to perform satisfactorily for test data. A low accuracy (<35%) was demonstrated by WBB class, whereas GR class showed good (>85 %) accuracy for these intensity levels. The highest overall classification accuracy was observed for 256 intensity levels during both training and test phase when compared to all other intensity levels included in study. A compromise between intensity levels and processing time was made by selecting the 256 intensity levels. They were selected because of plenty of information lost during the down quantization, which decreased the accuracy of machine learning algorithms (Table 4-6).

Table 4-6: Effect of reduced CCM intensity levels on the classification accuracy for fixed image size of 128 × 128 pixels.

Intensity Levels	Training Accuracy (%)			Testing Accuracy (%)		
	Category			Category		
	GR	WBB	Total	GR	WBB	Total
8	98.26	86.99	93.55	87.22	15.09	57.07
16	93.26	88.08	91.09	86.25	16.23	56.98
32	90.23	89.43	89.90	88.67	33.58	65.65
64	92.56	90.79	91.82	91.42	71.70	83.18
128	96.86	91.33	94.55	93.37	83.77	89.36
256	95.70	94.04	95.00	94.34	93.58	94.02

4.3.3 Effect of Image Size on Processing Time and Classification Accuracy

A comprehensive analysis in time space was performed to calculate the execution time required to convert a colour image to HSI, generate three CCMs and extract 39 textural features on a core i7 6700K computer (Table 4-5). Full frame and AOI image sets were used to examine the effect of image size on overall processing time. The experimental results indicated that total time required for colour conversion to feature extraction increases with an increase in image size. An increment of 6.46 times was observed as the image size grew from 16 × 16 to 1024× 1024 pixels. The computational time break-up showed that the increase in image size from 16 × 16 to 1024× 1024 pixels resulted in an escalation in colour conversion time from 25.930 µs to 37,079.122 µs. Significantly higher colour conversion time was observed for images having a size of 128 × 128, 256 × 256, 512 × 512, and 1024 × 1024 pixels. This might be due to large number of trigonometric calculations needed to convert the colour information contained in an individual pixel of relatively larger sized images.

The time required for CCMs construction varied from 1024.392 µs to 17,854.930 µs. A visible increment in construction time was observed for images larger than 64 pixels and was found to be second highest processing time for 1024 × 1024 images in overall time space. This increasing trend was due to an increase in lookup time required to search and fill the particular intensity level information contained in larger images. The computational time for textural features extraction was not affected by image size and varied from 8813.606 µs to 8816.116 µs. The non-significant difference in mean features extraction time was observed for all image sizes involved in this study. This behavior revealed that time required for textural feature extraction was independent at least for these image sizes. This was due to fixed spatial dimensions (256 × 256) of CCMs causing the constant 256 iterations to extract each textural feature from individual CCM without being

influenced by image size. Therefore, computational time for textural features was found to be dominant for small images and as image size increases, computational time for colour conversion and CCMs construction gets larger and gradually becomes dominant.

Table 4-7: Detailed analysis of the colour conversion, CCM construction, and textural features extraction time for different sized images on core i7 6700K architecture.

Image Size (Pixels)	Average Time (µs)				Difference (%)
	HSI Conversion	Co-occurrence Matrix	Textural Features	Total	
16 × 16	25.930 e	1024.392 e	8813.606 a	9863.928 e	--------
32 × 32	44.615 e	1025.162 e	8813.893 a	9883.670 e	0.20
64 × 64	136.065 e	1037.787 e	8814.393 a	9988.245 e	1.26
128 × 128	505.261 d	1330.402 d	8814.601 a	10,650.264 d	7.97
256 × 256	2210.559 c	2149.351 c	8815.610 a	13,175.520 c	33.57
512 × 512	9194.725 b	5667.850 b	8815.705 a	23,678.280 b	140.05
1024 × 1024	37,079.122 a	17,854.930 a	8816.116 a	63,750.168 a	546.29

Means with no letter shared in the same column are significantly different at p=0.05

The extrapolation of different unit image sizes (16 × 16, 32 × 32, 64 × 64, 128 × 128) for an AOI image (768 × 128) revealed that average total time for an AOI image with 384 of 16 × 16 pixels unit images was highest (3,787,748.352 µs) (Table 4-8). However, only 63,901.584 µs were required to convert, construct, and extract all textural information contained in an AOI image with

6 of 128 × 128 pixels unit images. The overall processing time was reduced by a factor of 59.26 as number of unit images decreased from 384 to 6 or as size of the unit image increased from 16 × 16 to 128 × 128 pixels. This was due to constant average time required for textural feature extraction. Therefore, smaller unit image size resulted in large number of unit images from an AOI, which ultimately lead to greater overall processing time.

Table 4-8: Summary of computational time for an AOI image with different sizes of unit images on core i7 6700K.

Unit Image Size	No. of Unit images in an AOI	Average Total Time (µs)		Difference
(Pixels)		1 Unit Image	1 AOI Image	(%)
128 × 128	6	10,650.264	63,901.584	---------
64 × 64	24	9988.245	239,717.88	275.13
32 × 32	96	9883.670	948,832.32	1384.55
16 × 16	384	9863.928	3,787,748.352	5826.36

The effect of unit image size on classification accuracy showed a decrease in overall and individual class accuracy with decrease in image size (Table 4-9). The 16 × 16 unit image was not included in this analysis because of difficulty involved in manually labeling the category of different images used for training purposes. All unit image sizes included in study achieved very high overall classification accuracy (>95%) during training phase. However, unit images of 32 × 32 size were only able to identify 53.94% of observations included in test data. A drastic decrease from 97.11% to 48.82% was observed for WBB class with GR accuracy decreased from 94.63% to 60.5%. Increase in unit image size to 64 × 64 helped to correctly identify 73.44% of test WBB observations. The highest performing unit image size was found to be 128 × 128 with overall test accuracy of 90.79% when compared to all other unit image sizes included in this study.

Table 4-9: Effect of different unit image sizes on the classification accuracy for fixed intensity levels of 256.

Image Size	Training Accuracy (%)			Testing Accuracy (%)		
	Category			Category		
	GR	WBB	Total	GR	WBB	Total
32 × 32	94.63	97.11	95.87	60.5	48.82	53.94
64 × 64	98.76	97.73	98.34	82.00	73.44	77.19
128 × 128	97.93	99.17	98.55	89.5	91.80	90.79

4.3.4 Comparison of Individual CCMs in Computational Time Frame

Hue, saturation, and intensity CCMs took almost the same time for colour conversion, CCMs construction, and features extraction. A quantification procedure was adopted to process a set of 2244 unit images (128 × 128). The intensity levels of these images were fixed to 256 during this experimental setup and core i7 6700K architecture was used. Results of Tukey's HSD indicated that mean time required for colour conversion was significantly different for all three colour planes. The maximum time was required to extract hue information from a BGR colour image (Figure 4-4). The minimum time taken during colour conversion was for intensity (52.638 μs) followed by saturation (98.336 μs). The relatively lower time requirement for intensity was due to the simple arithmetic operations involved in its extraction. A similar concept can be used to explain the low extraction time needed for saturation colour plane.

The time required for CCM construction was also found to be significantly different with highest (449.980 μs) and lowest (397.054 μs) times observed for saturation and intensity CCMs, respectively. A similar trend of significantly different execution time was observed for textural

features. The highest time (3601.741 µs) during feature extraction was required by saturation colour plane, followed by intensity colour plane (3585.643 µs). The hue features took 3568.160 µs. Overall performance of CCMs based algorithms can be improved by reducing the time required for hue conversion. A colour conversion look-up table (LUT) might be an acceptable solution to reduce the processing overhead involved with hue extraction. The reduction of features could also be helpful for reducing the overall processing time of CCMs.

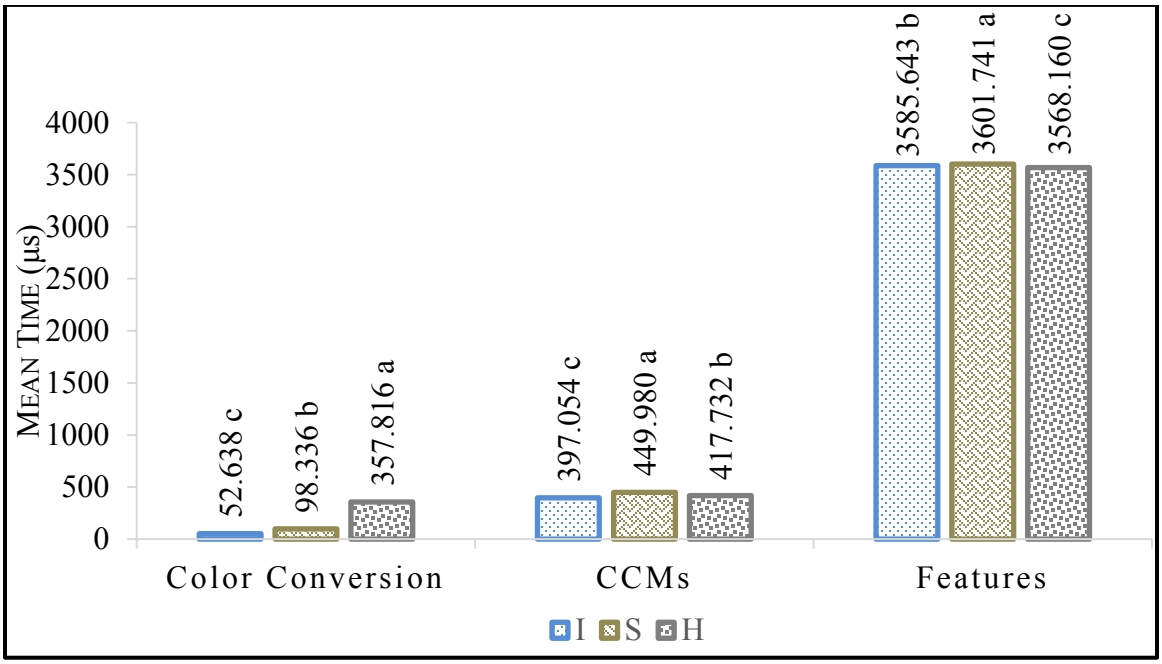

Figure 4-4: Mean execution time from colour conversion to feature extraction for individual CCM using core i7 6700K (Means with no letter shared are statistically different at P = 0.05).

4.4 Conclusions

The goldenrod detection system consisting of a graphical user interface, CCM based image processing algorithm for extracting textural features in real-time, and machine learning techniques was developed. Parameters influencing the real-time application of CCMs were also optimized with their potential effect on goldenrod identification accuracy. The Marshal.copy method of C# programming language was found to be most suitable for reading the image from computer RAM

as it took the least time. There was a significant difference between mean execution time of CCMs for different intensity levels. Images with 256 and 128 intensity levels took 10,650.264 μs and 5026.999 μs, respectively and were able to achieve an overall accuracy of 94% and 89%, respectively on test images. Reduction of intensity levels also resulted in the reduction of goldenrod classification accuracy. The colour conversion and CCM construction time were found to be dominant for the images larger than 256 × 256 pixels. A unit image size of 128 × 128 pixels can be adopted for real-time applications because of the highest classification accuracy. It also helped to minimize the computational time for processing an AOI image with current camera settings. The textural features extracted from CCMs were intensity dependent rather than image size. The highest time for colour conversion was needed by hue, while CCM construction and feature extraction required the most time for saturation colour plane. Based on the results of this study, it can be concluded that Marshal.copy method, intensity levels of 128 or 256, and a unit image size of 128 × 128 pixels can help to minimize the computational burden without compromising the classification accuracy for real-time applications. The quantitative textural features extracted from CCMs in combination with statistical and artificial neural network techniques can be used to develop classification criterions to target the goldenrod site-specifically in wild blueberry fields.

CHAPTER 5: DEVELOPMENT OF WILD BLUEBERRY AND GOLDENROD SEGMENTATION CLASSIFIERS USING STATISTICAL AND ARTIFICIAL NEURAL NETWORK TECHNIQUES

5.1 Introduction

Despite complex plant, residue, and soil ecosystem's dynamics, CCMs along with non-linear, multifactor modeling techniques have the potential to systematically identify different plant covers (Burks et al., 2005). The quantitative textural features can be employed to classify the members of two or more mutually exclusive data groups by mining the underlying relationships between these features and respective group (Pao, 1989). These modeled relationships can learn from externally supplied successive real field plant cover instances to make predictions about similar future instances (Marchant and Onyango, 2003) and will be able to adapt any unforeseen changes in data on the basis of the similarity of supplied instances (Pao, 1989). Modeling these classifying relationships from textural features is possible by using statistical and artificial neural network (ANN) techniques based on the dimensional nature of input data and output classes (Burks et al., 2005).

The statistical methods for developing the classification relationships are based on the process of calculating the instance probability of belonging to an individual class followed by a decision condition of classifying the instance to a class with the highest probability (Klecka, 1980). These methods were reported to be effective for weed crop classification in a variety of plant covers (Shearer and Holmes, 1990; Mayer et al., 1998; Lee et al., 1999; Burks et al., 2001; Gebhardt et al., 2006; de Castro et al., 2013). Shearer and Holmes (1990) used textural features to develop a discriminant model based on generalized square distances between two classes to classify seven different cultivars of nursery plants. They were able to achieve a maximum classification accuracy of 90.9% on test image data using a quadratic model.

The ANN based techniques can be effectively used to relate the multifactor linear or non-linear associativity of textural features with different groups (Burks et al., 2005). The key element of this paradigm is the novel structure of information processing system capable of extracting the useful classifying non-linear functional relationships (Pao, 1989). Tang et al. (1999) characterized images into broadleaf and grass categories with 100% classification accuracies using the Gabor wavelet algorithm followed by three-layered feedforward back-propagation ANN model. Cho et al. (2002) modeled the canopy shape features to an ANN classifier trained with logistic sigmoid function for delineating the weed plants in radish fields. They achieved approximately 93% accuracy in both cases. Burks et al. (2005) compared the performance of four ANN classifiers modeled through CCM features. The results of this study indicated that BP-ANN classifier resulted in the highest classification accuracy of 97% along with the low computational requirements. Chang et al. (2012a) were able to classify 98.9% of wild blueberry and 93.9% of weeds correctly by using a linear discriminant model. A large number of studies have been carried out for different cropping systems, however, to date no work has been reported regarding the application of statistical and ANN classifying models specifically for goldenrod identification in wild blueberry cropping system.

Wild blueberry producers are currently looking for technologies to minimize the cost of production due to continuously shrinking profit margins. The cost associated with traditional uniform application of herbicides can be cut down by developing a VR spraying system capable of targeting goldenrod site -specifically. Therefore, there is a need to develop classifying models from textural features by employing statistical and ANN techniques for goldenrod detection in real-time that can control the individual nozzle of VR spraying system accordingly. The classification accuracy of these developed relationships needs to be compared and evaluated on

independent test dataset to select highly accurate classifying model for practical applications. These models will help the wild blueberry growers to minimize the cost of production by reducing today's herbicide influx.

5.2 Materials and Methods

5.2.1 Image Acquisition

Four wild blueberry fields were selected in central Nova Scotia, Canada to develop an image library containing the images of goldenrod, wild blueberry, bare spots, and mixed canopies. The wild blueberry field images were acquired during summer of 2015 and 2016. A set of 2701 full frame (1280 × 1024) images was added to the library from North River I and Cattle Market fields during 2015. Another set of 9,669 AOI images was added to image library by collecting data from North River II and Londonderry fields using mobile field imaging system equipped with four cameras during summer 2016. Test tracks containing goldenrod patches were selected and data was acquired from two cardinal directions. The images were acquired in the natural illumination conditions along with any artifacts caused by UTV/boom shade, and variation in lightning caused by clouds. To accommodate the effect caused by sun angle, the image acquisition process was repeated at different times throughout the day.

5.2.2 Data Division and Processing

The image library was partitioned into two datasets containing 70% of data for developing and training a model and 30% for validating the model. The images were randomized before including in any of these datasets on the basis of their acquisition time. The AOI images were cropped from full frame images acquired during 2015 by using IrfanView. In order to isolate the individual class specimen, 128 × 128 pixels unit images were extracted from AOI images of both years. There were six unit images (128 × 128) from an individual AOI image. The extracted unit images were manually classified into wild blueberry and goldenrod and were labeled with "spray"

or “no spray” tags. The unit images were processed in laboratory using QGDS program and two databases of textural features were developed for GR and WBB classes.

5.2.3 Classifying Variables Selection

The SAS PROC STEPDISC procedure was used for sifting through a large number (39) of potential independent features from a unit image and then for fine-tuning an existing model. The stepwise procedure consisting of forward selection and backward elimination opted during feature selection. The feature having the highest F-statistics and R^2 was added first in model during forward selection followed by the exclusion of non-significant feature during backward elimination. The feature addition and removal was assisted by defining 0.00015 as significance level to enter (F-to-enter) and 0.0001 as significance level to remove (F-to-remove). This procedure was used for individual colour plane and their possible combinations along with control model containing all 39 features for monitoring the relative performance of all developed DMs. The feature selection procedure was further aided by developing the matrix plots in Minitab 17 to identify features strongly relating to class memberships.

5.2.4 Development of Statistical Classifiers

The SAS PROC DISCRIM procedure was used to define a statistical classification criterion. The univariate and multivariate normality tests were performed to select from parametric and non-parametric methods. The normality tests also helped to identify outliers in training data set resulting in the exclusion of these extreme scenarios from classifers. The test of homogeneity was performed for selection of within group or group covariance matrices. The linear and quadratic classifying criterions were developed for all DMs extracted during previous step. The prior probabilities of goldenrod and wild blueberry classes were set to the same level.

5.2.5 Development of BP-ANN Classifiers

The multilayer, feedforward, supervised, back-propagation neural networks were trained by using Peltarion Synapse software. The same arrays (DMs) of input variables selected by STEPDISC were used for BP-ANN classifiers development. The BP-ANN classifiers were developed using DMs with the highest classification accuracy during DISCRIM procedure along with DM containing all 39 features to compare the relative accuracy of other DMs. For the individual DM, the network was trained on trial and error basis. The adjusted networks were extracted using the deployment post-processing tool of Peltarion Synapse software to make a separate and stand-alone WorkArea0.dll (.NET dynamic linking library) file. A C# based command prompt program was written to predict and validate both external and internal data sets by using WorkArea0.dll file and save processed result as a comma separated value (CSV) file. These networks for internal and external validations were tested and evaluated to achieve highest overall and individual species classification accuracy with MSE as a supplementary criterion to assist the evaluation process. Each parameter was tweaked individually at a time to determine the best choice for each parameter. The performance of these networks at the end of each tweak was tested by evaluating it on both training and testing data sets. The detailed procedure of statistical and BP-ANN classifiers development can be seen in Chapter 3.

5.3 Results and Discussion

5.3.1 Feature Selection Results

The SAS STEPDISC resulted in development of seven different reduced DMs along with a control DM containing all 39 features (Table 5-1). The features of three models (DM-H_{SD}, DM-S_{SD}, and DM-I_{SD}) were reduced by removing the CCMs and features of other planes followed by the implementation of feature reduction procedure. The least number of features (5) were observed for intensity CCMs followed by hue and saturation features (7). The other three models (DM-

HS_{SD}, DM-HI_{SD}, and DM-SI_{SD}) were developed by reducing the features from all possible combinations of two colour planes. The final model (DM-HSI_{SD}) was extracted by reducing the features of all three colour planes in order to get the list of features having the highest possible classification accuracy with minimal computational load. The number of required features in this model was reduced from 39 to only 7 with complete exclusion of features from intensity colour plane. This significant reduction of H and S features along with complete removal of intensity colour plane could reduce the computation required in the analysis by at least one-third, given that this model will comparatively achieve the highest classification accuracy. The removal of intensity features from this model might be due to their limited discriminatory power as this colour plane is majorly affected by any variation in outdoor illumination condition (Burks, 1997).

Table 5-1: Summary of SAS STEPDISC function for selection of different textural features from different colour planes.

Data Model	Colour Spaces Used	Selected Textural Features
DM-H_{SD}	H	Hf2, Hf3, Hf4, Hf5, Hf7, Hf8, Hf13
DM-S_{SD}	S	Sf2, Sf4, Sf5, Sf7, Sf9, Sf10, Sf13
DM-I_{SD}	I	If1, If3, If5, If9, If12
DM-HS_{SD}	H and S	Hf3, Hf5, Hf9,Hf8, Hf11, Hf13, Sf3, Sf7
DM-HI_{SD}	H and I	Hf2, Hf13, If1, If3, If5, If9, If12
DM-SI_{SD}	S and I	Sf4, Sf5, Sf7, Sf9, Sf11, If9
DM-HSI_{SD}	H, S, and I	Hf3, Hf4, Hf5, Sf5, Sf7, Sf10, Sf13
DM-HSI	H, S, and I	All 39 features

The subscript SD indicates the STEPDISC models with reduced features, Hf2 indicates the second feature of the hue term, and so on.

The matrix plots of different textural features were developed for both classes in order to guard against the over and under specified data models (Figures A-3, A-4; Appendix A). The

matrix plot of hue features indicated that several features are correlated thereby shared same discriminatory information and can be reduced further. Taking help from this plot Hf2 feature was removed from DM-H_{SD} model and another feature HF12 was added in it (Table 5-2). The matrix plot of saturation and intensity features indicated the addition of Sf2, Sf5 features in DM-HSI_{SD}, DM-HS_{SD} and If7 in DM-$I_{SD,}$ respectively. These fine-tuned models were used for the development of classifiers.

Table 5-2: Modified models with new features added or removed by using matrix plots.

Data Model	Colour Spaces Used	Feature(s)		List of New Textural Features[1]
		Added	Removed	
DM-H_{SD}	H	Hf12	Hf2	Hf3, Hf4, Hf5, Hf7, Hf8, **Hf12**, Hf13
DM-S_{SD}	S	----	Sf10	Sf2, Sf4, Sf5, Sf7, Sf9, Sf13
DM-I_{SD}	I	If7	----	If1, If3, If5, **If7**, If9, If12
DM-HS_{SD}	H and S	Sf5	----	Hf3, Hf5, Hf8, Hf9, Hf11, Hf13, Sf3, **Sf5**, Sf7
DM-HI_{SD}	H and I	-----	-----	Hf2, Hf13, If1, If3, If5, If9, If12
DM-SI_{SD}	S and I	----	Sf11	Sf4, Sf5, Sf7, Sf9, If9
DM-HSI_{SD}	H, S, and I	Sf2	----	Hf3, Hf4, Hf5, **Sf2**, Sf5, Sf7, Sf10, Sf13
DM-HIS	H, S, and I	----	----	All 39 features

[1] *Bold face letters indicate newly entered features*

5.3.2 Normality Test

The multivariate and univariate (Shearer, 1987) normality tests were performed for both training and testing datasets using Minitab 17 in order to make a decision between parametric or non-parametric methods of generating the discriminant criterion. The results of univariate normality tests indicated that most of textural features of both classes were normally distributed

with exception to the few that were found to be skewed. The data was transformed using different techniques (square root, cube root, natural log, log, square, and cube) to induce the normality. While these transformations helped to induce normality in some features, they actually skewed the distribution of other features in same class or other class. None of these transformations were founded to normalize the whole dataset of both classes. Although some features exhibited the skewness, but none of them were found to be bimodal leading us to approximate that all features in both classes were normally distributed (Shearer and Homes, 1990). Furthermore, the discriminant analysis is a robust technique which can tolerate skewness in real field data (Lachenbruch, 1975) thus minimizing the effect of this approximation.

The scatter plots of squared Mahalanobis distance against chi-square quantiles for the hue, saturation, and intensity indicated that most of data in multivariate space were normal for both classes (Figures A-1 and A-2; Appendix A). The analysis of these plots indicated that outliers have squared Mahalanobis distance notably greater than their chi-quantiles for these data points. It was also observed that the outliers in all three hue, saturation, and intensity plots were from same goldenrod and/or wild blueberry images. It was found that outlier images had relatively high saturated pixels caused by variation in outdoor illumination conditions and/or reflections from UTV/boom (Figure 5-1). The outlier images were removed from training data resulting into the datasets, which were more representative of two classes.

Figure 5-1: Sample images responsible for generating the relatively erroneous data in hue, saturation, and intensity colour planes.

5.3.3 Statistical Classifiers

The parametric methods were used for developing the decision criterion using discriminant analysis. The significance of homogeneity test at level of 10% indicated the use of within-group covariance matrices to derive quadratic discrimination criterion for all DMs. However, the linear classifiers were also developed and compared to quantify the cost of misclassification. The linear and quadratic classifiers were trained by running each DM individually. In each case, same training and testing data sets were utilized in order to have a fair comparison between DMs. The results of quadratic classification criterion indicated that model DM-HSI_{SD} achieved the highest accuracy among all other models (Table 5-3). The overall classification accuracy achieved by this model was 95.39% and 93.08% for training and testing datasets, respectively. The accuracies for GR and WBB classes were 94.13% and 97.18% during the training phase, and 93.27% and 92.74% during the test run. The model (DM-HSI) containing all 39 features showed relatively lower overall classification accuracy when compared with DM-HSI_{SD}. The DM-HSI_{SD} misclassified the 2,993 GR observations to WBB class along with 1,825 WBB observations categorized as GR from the test data (Table 5-4). Out of 44,473 GR observations, the DM-HSI model misclassified 3,385 as WBB. The misclassification rate of this model was approximately 28.66% higher when compared with the DM-HSI_{SD} for WBB data (Table 5-4). This relatively high WBB misclassification rate

might be due to the similarity of class membership means at some features included in DM-HSI model thereby increasing the misclassification rate (Klecka, 1980).

Table 5-3: Classification accuracies of quadratic classifiers developed by using different DMs.

Data Model	Training Accuracy (%)			Testing Accuracy (%)		
	Category			Category		
	GR	WBB	Total	GR	WBB	Total
DM-H_{SD}	77.77	90.14	82.86	70.60	85.16	75.86
DM-S_{SD}	93.96	91.77	93.06	91.92	87.36	90.27
DM-I_{SD}	85.30	69.15	78.65	75.76	66.04	72.25
DM-HS_{SD}	91.34	91.71	91.49	88.89	91.18	89.72
DM-HI_{SD}	87.93	79.12	84.30	87.40	76.37	83.42
DM-SI_{SD}	92.39	95.77	93.78	90.91	86.26	89.23
DM-HSI_{SD}	94.13	97.18	95.39	93.27	92.74	93.08
DM-HSI	93.96	92.96	93.55	92.39	90.66	91.77

The model (DM-S_{SD}) containing the reduced features from the saturation classified the 93.96% of GR and 91.77% of WBB on training data. The accuracies of GR and WBB were reduced to 91.92% and 87.36% respectively during the test run. The accuracies of this model in comparison of DM-HSI_{SD} were lower for WBB class. However, only one CCM was required for this model thereby reducing the processing time by at least two-third along with the exclusion of most time-consuming hue CCM. This model categorized 3,593 GR observations as WBB and 3,178 WBB observations as GR. This model can be used for real-time applications with little compromise made

on over spray in WBB patches. The remaining individual CCM models (DM-H_{SD}, DM-I_{SD}) showed less than 90% overall accuracy. The model DM-H_{SD} achieved 85.16% accuracy for WBB classification with very high misclassification of GR on test data. The DM-I_{SD} model showed poor performance (<70%) for classifying WBB during both training and test run. The lower accuracy of this model for WBB could be due to variation in illumination conditions affecting the intensity colour plane thereby causing the rapid variability in CCM features (Burks et al., 2001). These results for DM-I_{SD} for WBB were similar to Chang et al. (2012a).

Table 5-4: Misclassified observations of three different models from the test data.

Category	Number of Observations Classified into Category					
	DM-HSI_{SD}		DM-HSI		DM-S_{SD}	
	GR	WBB	GR	WBB	GR	WBB
GR	41,480	2,993	41,088	3,385	40,879	3,593
WBB	1,825	23,319	2,348	22,796	3,178	21,966

The models (DM-HS_{SD}, DM-HI_{SD}, and DM-SI_{SD}) developed from the combination of two different CCMs achieved overall accuracies ranging from 84% to 94% for training data and 83% to 90% for test data. The least accurate model among these was DM-HI_{SD}, as it just classified 84.30% and 83.42% of observation correctly in training and resting respectively. The overall accuracy of this model was reduced because of lower accuracy showed by this model for WBB class. The model DM-SI_{SD} showed some promise over DM-HI_{SD} for GR (92.39%) and WBB (95.77%) during training. However, it performed relatively poor for WBB (86.26%) on test data while maintaining the acceptable classification accuracy for GR. The WBB class affected the

performance of both of these models that might be again due to poor identification capacity of intensity features.

The overall classification accuracies of all linear DMs were less than their respective quadratic DMs for test data (Table 5-5). None of the linear models showed the classification accuracy of 90% for GR class on test data. The only model that achieved the highest classification accuracy was DM-HSI_{SD} for both GR and WBB during training and testing phase. Another model with the comparable performance was DM-$S_{SD,}$ which showed an accuracy of 91.86% and 90.23% in training and 85.86% and 91.21% in testing for GR and WBB respectively. The DM-HSI model with all 39 features showed good overall accuracy (96.64%)during the training phase but was not up to the mark for GR classification in the testing phase.

Table 5-5: Classification accuracies of linear classifiers developed by using different DMs.

Data Model	Training Accuracy (%)			Testing Accuracy (%)		
	Category			Category		
	GR	WBB	Total	GR	WBB	Total
DM-H_{SD}	87.88	63.38	77.79	86.09	51.65	73.65
DM-S_{SD}	91.86	90.23	91.19	85.86	91.21	87.79
DM-I_{SD}	90.03	50.70	73.83	87.88	41.21	71.02
DM-HS_{SD}	93.44	97.59	95.15	80.81	91.21	84.57
DM-HI_{SD}	88.98	85.92	87.72	82.83	74.73	79.90
DM-SI_{SD}	92.13	95.77	93.63	84.88	90.11	86.77
DM-HSI_{SD}	92.87	97.18	94.64	86.87	93.92	89.42
DM-HSI	95.28	98.59	96.64	81.82	92.86	85.81

5.3.4 BP-ANN Classifiers

The BP-ANN classifiers were developed using two DMs (DM-HSI_{SD}, DM-S_{SD}) that showed the highest classification accuracy (>87%) with quadratic classifiers on both training and testing data sets during DISCRIM procedure along with a control DM-HSI containing all 39 features. Only two DMs were selected for BP-ANN classifiers because of the difficulty involved with tweaking the topology and learning parameters for individual DM on trial and error basis. The similar training and testing data sets were used for evaluating the relative performance of BP-ANN over respective statistical classifiers. All discussion about topology design and parameters selection was made for only DM-HSI_{SD} model due to limitation of space, however, similar procedure was adopted for DM-S_{SD}, DM-HSI used to develop BP-ANN classifiers.

5.3.4.1 Back-Propagation Topology Design

The network topology of the BP-ANN classifier based on DM-HSI_{SD} model was evaluated by adopting the experimental approach of constructive algorithms. The numbers of input and output neurons for all these topologies were remained fixed along with variable number of hidden layer neurons (Table 5-6). The eleven topologies were developed during this experimentation and classification accuracies for both training and testing datasets were recorded for evaluation and comparison purposes. The topology design evaluation also compared the symmetrical (same number of neurons in each hidden layer) and asymmetrical two hidden layer topologies. The results indicated that all topologies showed higher GR classification accuracies (>91%) during training and testing phases. However, none of these topologies achieved greater than 90% accuracy for WBB class in testing phase. This may be due to limited training epochs thereby lowering the WBB test classification accuracy.

The DM-HSI_{SD} model showed the highest overall classification accuracy on training and testing data sets for TM6 topology (Table 5-6). This topology achieved classification accuracies of 97.80%, 94.93% for GR class and 91.99%, 88.74% for WBB class during training and testing. A similar number of hidden neurons with one hidden layer (TM2) did not perform as closely to TM6 during test run. A reduction of approximately 4.73%, 4.12%, and 3.41% was observed in overall classification accuracies of TMI, TM2, and TM3 topologies in comparison to TM6. Even though TM2 contained nine hidden neurons like TM6 but exclusion of a hidden layer resulted in a drop of in WBB classification accuracy on test data. The comparison of symmetrical two hidden layer topologies indicated that overall classification accuracy increased with increasing number of hidden neuron until TM8 (5×5) and then reduced with six neurons at each hidden layer (TM10). The better performance of TM8 over the other symmetrical topologies was majorly due to WBB classification accuracy of 87.03% on test dataset. The GR classification accuracy of this topology was approaching to asymmetrical TM6, thereby making it a good alternative of this asymmetrical topology. It was observed that TM10 was over-trained symmetrical topology with least MSE at a cost of decrement in classification accuracy of test WBB. The least value of MSE indicated the closeness of fit of TM10 topology to training data only thereby losing the accuracy for overall population of WBB class. This topology tried to suit the particularities of training data being used along with the loss of network ability to generalize the ranges of input values to cover the entire population of (LeCun et al., 2012) WBB class.

The MSE reduced with increase in number of hidden neurons. The MSE showed by the TM6 was lower than all other bigger networks, but higher overall classification accuracy (92.26%) of this topology on test data made it more appropriate selection for further analysis. Moreover, the computational complexity of TM6 was relatively less than TM8 and TM9. It was therefore

concluded from these results that asymmetrical TM6 was appropriate selection among these topologies based on 94.93% and 88.74% test accuracies for GR and WBB, respectively.

Table 5-6: Classification accuracy of different topologies tested for the DM-HSI$_{SD}$ data model at an epoch size of 1,000.

Topology Model	Model Structure	MSE	Training Accuracy (%)			Testing Accuracy (%)		
			Category			Category		
			GR	WBB	Total	GR	WBB	Total
TM1	8×5×2	0.093	96.45	88.28	92.14	91.44	81.89	87.89
TM2	8×9×2	0.089	94.56	90.88	93.16	91.74	84.50	88.45
TM3	8×3×3×2	0.084	96.45	91.90	94.65	92.93	83.80	89.11
TM4	8×4×3×2	0.083	97.16	93.90	95.67	93.93	88.03	91.47
TM5	8×4×4×2	0.083	96.79	90.09	94.65	92.92	84.50	89.11
TM6	8×5×4×2	0.082	97.80	91.99	95.91	94.93	88.74	92.26
TM7	8×4×5×2	0.081	96.80	91.90	95.16	93.43	88.03	91.17
TM8	8×5×5×2	0.075	97.16	90.90	95.67	93.94	87.03	91.47
TM9	8×6×5×2	0.075	96.80	91.90	95.20	93.43	88.03	91.17
TM10	8×6×6×2	0.073	96.45	90.99	94.94	93.43	83.80	89.41
TM11	8×7×6×2	0.078	96.45	90.99	94.91	94.44	87.32	91.47

5.3.4.2 Back-Propagation Parameter Selection

The TM6 topology was used further for the selection of the appropriate training parameters. The TM6 topology, tanh sigmoid mathematical function, MT of 0.7, and online training mode was used to locate the best LR at 1000 epochs for these particular settings. Results showed that all LRs

attained high (>93%) classification accuracy for GR class for both training and testing data (Table 5-7). However, only two LRs (0.075 and 0.085) showed a classification accuracy of approximately 90% for WBB class during the test phase. It was also observed that increasing the LR beyond 0.09 enabled TM6 topology to learn better during training phase while causing noticeable drop of in WBB accuracy for test data. These high LRs resulted into the over-trained networks with the lower MSE, thereby reducing the accuracy of TM6 topology. By keeping in view the results of classification accuracies and MSE, the LR of 0.085 was selected for the further parameter selection.

Table 5-7: Classification accuracy of different learning rates for the DM-HSI$_{SD}$ data model at an epoch size of 1,000.

Learning Rate	MSE	Training Accuracy (%)			Testing Accuracy (%)		
		Category			Category		
		GR	WBB	Total	GR	WBB	Total
0.025	0.106	96.10	87.39	92.51	93.94	85.92	90.76
0.040	0.095	96.45	89.19	93.46	93.44	85.92	90.72
0.045	0.093	96.45	89.19	93.46	92.93	85.21	90.14
0.050	0.091	96.10	89.19	93.25	94.44	86.62	91.62
0.075	0.086	96.81	91.89	94.78	93.94	89.44	92.31
0.085	0.076	97.16	92.09	95.07	93.94	91.14	92.93
0.090	0.081	96.81	91.89	94.78	93.94	88.73	92.06
0.100	0.071	96.81	91.01	94.42	93.44	86.62	90.98
0.125	0.068	97.16	92.80	95.36	94.44	88.73	92.38
0.150	0.064	96.81	91.40	94.58	93.94	85.92	91.04

The batch and online LMs were tested for adjusting the weights and biases either on the system or pattern error for TM6 topology with previously selected parameters. The results indicated that the overall performance of batch mode was poor (Figure 5-2). The TM6 topology with this mode of weight updates was not able to learn appropriately for GR class as indicated by very low accuracy (<4%) of this class during training. On the other hand, online mode indicated the potential of classifying approximately 96% of GR correctly during both training and testing phase. It showed relatively lower performance for WBB class when compared with the batch mode. A balance between the accuracy of both classes resulted in the selection of online LM for further analysis.

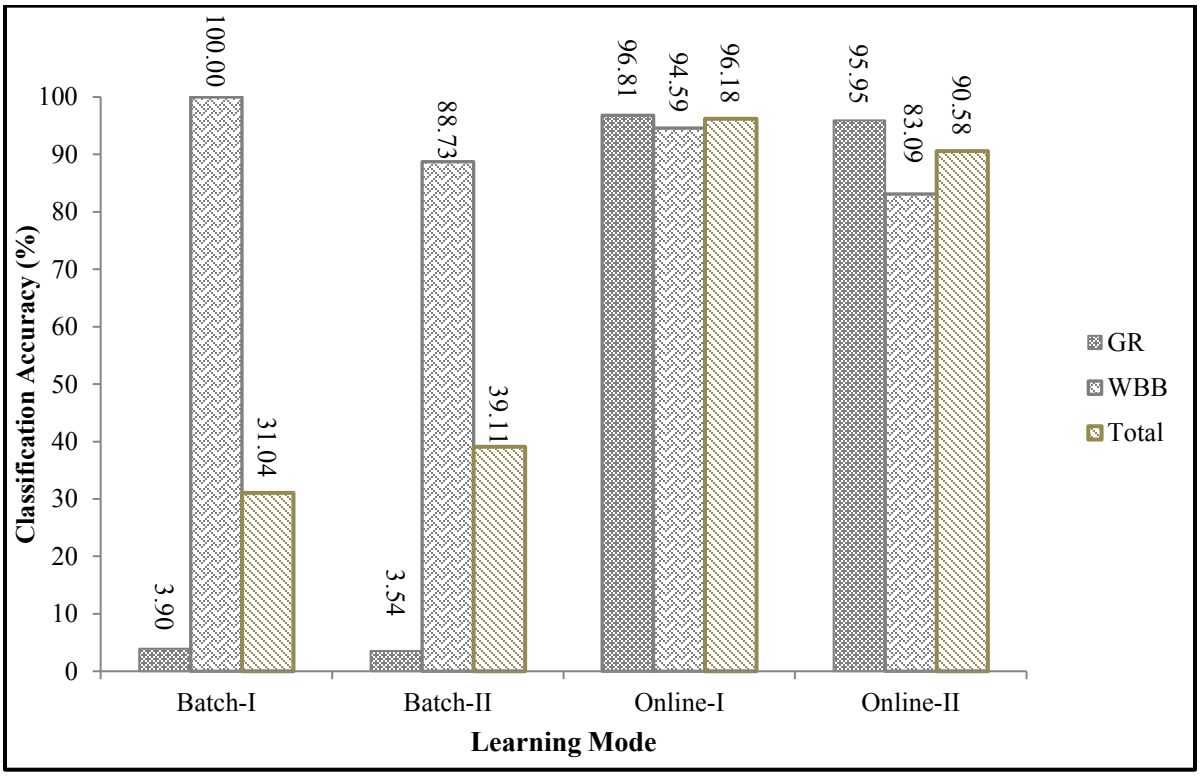

Figure 5-2: Effect of batch versus the online learning mode on the classification accuracy for DM-HSI_{SD} data model at an epoch size of 1,000 (I and II represent the training and test data, respectively).

The MT was varied from 0.70 to 0.95 for TM6 topology along with all previously adjusted parameters. It was observed that MT of 0.80 achieved comparatively highest classification accuracy (89.44%) for the WBB class of test data and all MTs indicated GR accuracy of at least 92% during test phase (Table 5-8). Despite having high classification accuracy for both classes during a training session and low MSE, the relative decrement in WBB accuracy for test data at MT of 0.95 was due to the over-training of this topology.

Table 5-8: Effect of the MT on the classification accuracy for the DM-HSI$_{SD}$ data model at an epoch size of 1,000.

Momentum Term	MSE	Training Accuracy (%)			Testing Accuracy (%)		
		Category			Category		
		GR	WBB	Total	GR	WBB	Total
0.70	0.077	97.16	91.89	94.99	92.93	88.73	91.41
0.75	0.083	96.45	90.99	94.20	92.93	83.80	89.63
0.80	0.067	97.16	91.89	94.99	95.45	89.44	93.28
0.85	0.072	97.16	91.89	94.99	94.45	88.03	92.13
0.90	0.070	97.16	92.79	95.36	94.94	87.32	92.19
0.95	0.030	98.93	96.40	97.89	97.47	78.87	90.75

Eight mathematical functions were tested with TM6 topology, LR of 0.085, MT of 0.80, and online training mode at 1000 epochs to find a suitable mathematical function (Table 5-9). Results showed that superposed logistic sigmoid-I, superposed logistic sigmoid-II, and Gaussian functions were not able to identify the WBB class at all, thereby classifying all the observations as GR for both training and test data. These functions did not allow TM6 topology to converge to a

trainable solution during training and were found to be inappropriate for this classification task. The Morlet and sine functions also showed relatively very less classification accuracy for WBB class during both training and testing phase along with MSE approaching to other poor performing functions. Results indicated that three functions, tanh sigmoid, logistic sigmoid, and linear had capabilities to classify GR and WBB with a reasonably high (>80%) accuracy for both training and test data (Table 5-9). It was found that tanh sigmoid achieved the highest training and testing classification accuracies for both GR and WBB classes among all functions tested. Furthermore, this function also indicated the least MSE. Based on the results of classification accuracies and MSE, the tanh sigmoid was selected for the further parameter selection.

Table 5-9: Tested mathematical activation functions for the DM-HSI$_{SD}$ data model at an epoch size of 1,000.

Mathematical Function	MSE	Training Accuracy (%)			Testing Accuracy (%)		
		Category			Category		
		GR	WBB	Total	GR	WBB	Total
Tanh Sigmoid	0.071	97.16	92.10	95.08	94.44	91.14	93.28
Logistic Sigmoid	0.128	96.10	88.73	93.07	93.93	85.59	90.92
Superposed Logistic Sigmoid-I	0.388	100.00	0.00	58.82	100.00	0.00	63.88
Superposed Logistic Sigmoid-II	0.388	100.00	0.00	58.82	100	0.00	63.88
Gaussian	0.387	100.00	0.00	58.82	100	0.00	63.88
Morlet	0.342	98.23	28.82	69.65	96.46	28.87	72.05
Linear	0.173	93.97	91.89	93.11	91.41	81.69	87.90
Sine	0.337	95.04	17.11	62.95	96.96	14.08	67.03

The results of epoch testing indicated that epoch size of 2,500 was enough for TM6 topology to classify the GR and WBB classes accurately, as a marked drop in the accuracy of test WBB was observed with greater epochs (Table 5-10). The results showed that with increase in epoch size MSE continues to decrease thus resulting in increased classification accuracy of both classes during training. While this increase caused the reduced accuracy of WBB class during test session especially beyond 4,000 epochs (Table 5-10). Results suggested the LR of 0.085, online LM, MT of 0.80, tanh sigmoid function, and an epoch size of 2,500 was suitable for TM6 topology.

Table 5-10: Relationship between epoch size and classification accuracy for the DM-HSI$_{SD}$ data model.

Epochs	MSE	Training Accuracy (%)			Testing Accuracy (%)		
		Category			Category		
		GR	WBB	Total	GR	WBB	Total
500	0.085	96.45	91.01	94.21	92.93	85.92	90.40
1,000	0.075	96.81	91.90	94.79	94.44	90.14	92.89
1,500	0.047	98.94	76.58	89.73	95.96	68.31	85.97
2,000	0.059	97.87	95.52	96.90	95.45	86.61	92.26
2,500	0.044	98.23	96.41	97.48	96.96	94.89	96.21
3,000	0.043	98.23	95.52	97.11	94.95	88.73	92.70
3,500	0.040	98.58	95.52	97.32	97.47	80.28	91.26
4,000	0.039	98.23	97.30	97.85	96.96	84.50	92.46
4,500	0.028	99.29	96.41	98.10	97.47	77.46	90.24
5,000	0.027	98.94	96.41	97.90	96.97	71.17	87.65

5.3.4.3 Comparison of BP-ANN Classifiers Only Based On DM-HSI_{SD}, DM-HSI, DM-S_{SD}

Two different DMs showing highest classification accuracy for both classes during DISCRM procedure were compared with a control DM containing all 39 features by developing three different BP-ANN classifiers for these DMs. The results showed that DM-HSI_{SD} based BP-ANN classifier was able to classify at least 97% of the GR with 95% of WBB classified correctly during both training and test session (Figure 5-3). The individual class and overall classification accuracy of this DM was highest when compared to other DMs included in this study. The test performance of this BP-ANN classifier increased approximately 3.69%, 2.15%, and 3.13% for the GR, WBB, and overall categories as compared to its quadratic statistical counterpart. The DM-HSI based BP-ANN classifier also showed the decent performance with approximately 1.82% and 3.93% less accuracy for test GR and WBB, respectively, when compared with the DM-HSI_{SD} classifier. The model (DM-S_{SD}) with least number of features showed relatively lower accuracy for the test WBB (87.17%) as compared to other models. It can be a good selection for real-time applications with a little compromise on classification accuracy. The optimum topologies and learning parameters used to achieve these accuracies for all three different DMs are given in Table 5-11. Based on the results DM-HSI_{SD} based BP-ANN classifier was used for field evaluation.

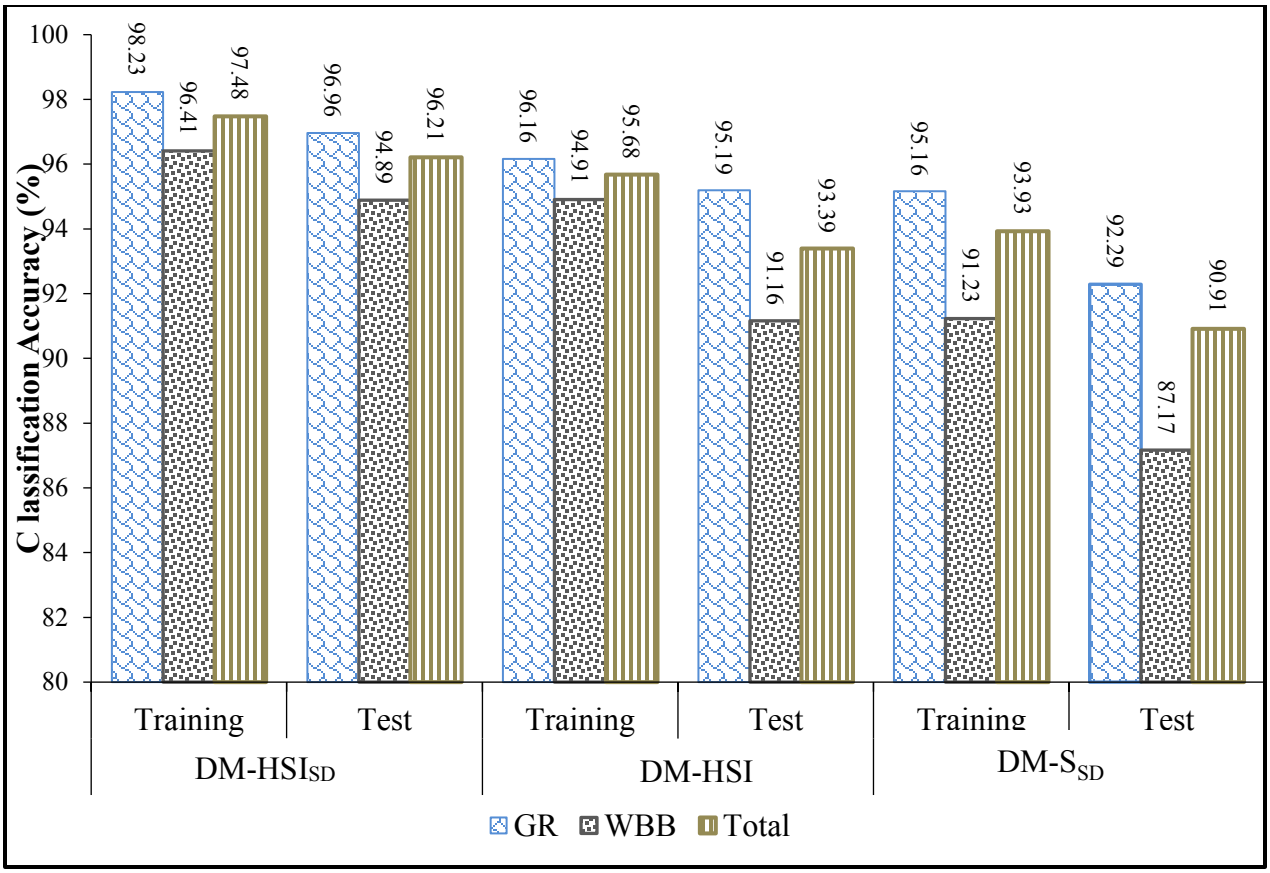

Figure 5-3: Performance comparison three different BP-ANNs developed from different DMs.

Table 5-11: Topologies and learning parameters used for different DMs based BP-ANN classifiers.

Optimum Parameters	$DM\text{-}HSI_{SD}$	DM-HSI	$DM\text{-}S_{SD}$
Topology	8×5×4×2	39×4×3×3×2	6×4×2×2
Mathematical Function	Tanh Sigmoid	Tanh Sigmoid	Tanh Sigmoid
Learning Rate	0.085	0.05	0.09
Momentum Term	0.80	0.75	0.90
Training Mode	Online	Online	Online
Epoch Size	2,500	2,000	4,500

5.4 Conclusions

In this study, plant cover imagery from wild blueberry fields was used to design and evaluate the statistical and BP-ANN classifying models to differentiate goldenrod from wild blueberry plants. The textural features extracted from image data using QGDS program were used to develop the different DMs with an effort to incorporate the most qualifying features for classifiers development. The performance of developed classifying models was evaluated using both training and test datasets. The optimal statistical classification model was quadratic in nature and was able to achieve highest overall classification accuracy of 93.08% on test data, when compared to all other quadratic models. The comparison of the quadratic and linear classifiers showed lower performance of all linear models developed in this study.

Two different DMs and a control DM were used to train the back-propagation based BP-ANN models. It was observed that topology and training parameters needs to be adjusted individually for different DMs to achieve the highest classification accuracy without being entrapped in the risk of over training. The same procedure of adjusting the individual network parameters was used for developing and evaluating the selected DMs. The BP-ANN model with the highest classification accuracy consisted of two hidden layers, a tanh sigmoid function, learning rate of 0.085, momentum term of 0.8, online training mode, and epoch size of 2,500. The comparison indicted the superiority of BP-ANN model (DM-HSI_{SD}) over respective statistical counterpart with better classification of both training and test data. In both (statistical and BP-ANN) cases, same model achieved the highest classification accuracy. On the basis of these results, it was decided to use the highest performing quadratic and BP-ANN classifiers for the field evaluation purposes thereby allowing us to quantify their actual performance experimentally.

CHAPTER 6: PERFORMANCE EVALUATION OF DEVELOPED GOLDENROD DETECTION SYSTEM FOR SPOT-APPLICATION OF HERBICIDE IN WILD BLUEBERRY FIELDS

6.1 Introduction

The response accuracy of machine vision and machine learning algorithms needs to be critically characterized, quantified, compared, and evaluated in real-life outdoor conditions (Haralick, 1993). Random variations and imperfections of input images caused by highly variable and adverse operating environments can easily influence the accuracy and precision of machine vision systems specifically used in agricultural fields (Romeo et al., 2013). Field evaluations of GDS can systematically unravel its potential for real-time applications by serving as a knowledge base to identify the sources responsible for reduced accuracy. These evaluations may also be helpful in identifying the loss of accuracy caused by over-generalization or non-convergence of network towards the desired results during laboratory scale training and evaluations of back-propagation artificial neural network (BP-ANN). The field experience gained can further be used enhance the accuracy of such systems by addressing the sources of error inside the algorithms (Jeon et al., 2011) and/or by adjusting the extrinsic parameters of the imaging devices (Romeo et al., 2013). The feedback of such critical investigations may also help to find the range of most suitable parameters for the algorithm to improve overall weed classification accuracy (Chang et al., 2014).

Lee et al. (1999) compared the performance of a robotic weed control system in outdoor and indoor conditions for tomato cotyledons. Results of indoor trials showed that only 8% of simulated tomato cotyledons were incorrectly sprayed with complete control of simulated weeds achieved by correct spraying. The system was only able to spray 47.6% of weeds properly with 24.2% over-sprayed tomato plants in a real-time commercial application. Tian et al. (1999)

evaluated a discrete wavelet transform based algorithm in corn and soybean fields for proper weed detection and spray. It was observed that maximum and minimum weed identification accuracies achieved by algorithm were 87.5% and 66.1%, respectively.

Esau et al. (2014) tested a prototype VR sprayer for foliar application of fungicides in wild blueberry cropping system. They reported that the prototype sprayer was able to correctly target the plant area with no significant difference in chemical application coverage when compared with uniform application (UA). The savings achieved by VR sprayer in bare soil zones were reported to be 9.90% to 51.22% compared to uniform application. Chang et al. (2014) used VR sprayer hardware developed by Esau et al. (2012) with an updated spectral reflectance based algorithm for identification of common weeds in wild blueberry cropping system. Results indicated that there was no significant difference between VR and UA on targeted weed spots. A significant difference was observed between weed and non-weed targets included in the study. A similar concept of successive field evaluations can be used to compare the performance of developed GDS (CCM algorithm and highly competitive BP-ANN and quadratic classifiers) in real-time field conditions. Results of these experimentations will be helpful in identifying the factors influencing the overall accuracy of GDS and can be used to increase the efficiency by addressing the sources of error inside of algorithm and classifiers or by adjusting the hardware related issues. Therefore, the major goal of this chapter was to quantify the real-time performance of a developed goldenrod detection system with different classifiers over the span of two years in different wild blueberry fields.

6.2 Materials and Methods

Field experiments were performed by using GDS containing two high performance classifiers in Londonderry, North River II, Portapique, and Robie Glenn wild blueberry fields during 2016 and 2017. Two experiments including a target spot based method with water sensitive

papers (WSPs) and coverage area (CA) detection approach with a non-permanent blue colour dye marker were performed in two fields during 2016. Experiment with WSPs helped to quantitatively compare the two different classifiers with UA in goldenrod and wild blueberry spots. Eight goldenrod (targets) and eight wild blueberry spots (non-targets) were randomly selected Londonderry and North River II field. Sixteen WSPs were placed on the selected points and were sprayed with two classifiers and UA. The paired t-test was used to compare the percentage area coverage (PAC) results of individual classifier with UA. The CA experiment was performed to compare classifier accuracy in real-time with an emphasize to determine any under-sprayed and over-sprayed areas. Goldenrod patches were mapped with RTK-GPS and tracks were sprayed with a tank mix of water and blue dye using two different classifiers. The same procedure was repeated by switching the models in two different fields to ensure the randomization of treatment application. Sprayed patches as indicated by colour dye were mapped again and superimposed maps were generated. Two-sample t-test was used to compare the CA of different sprayed polygons.

The goldenrod damage was assessed by spraying Portapique, and Robie Glenn wild blueberry fields with a tank mix of Callisto® 480SC (480 g L^{-1} Mesotrione) herbicide, Agral® 90 (92% Nonylphenoxy polyethoxy ethanol) non-ionic spreading agent and water in 2017. A completely randomized design was used to setup field plots of 6.1 m × 5 m for data collection. The stem height (SH), damage rating (DR), and percentage of green pixels (PGP) calculated from digital images were used as measures to compare the performance of two classifiers along with UA and CN. One-way analysis of variance (ANOVA) was used to compare three different treatment means, followed by a least significance difference (LSD) test as a post hoc method for identifying any significantly different mean. The DR data were analyzed by performing a rank-

based non-parametric Kruskal-Wallis H test using Proc Npar1Way procedure in SAS 9.3. The detailed procedure adopted for experimental purposes are shown in Chapter 3. The results reported during 2016 were achieved by training the classifiers using only the image library of 2015. The image library of 2016 was used for the experiments performed in 2017.

6.3 Results and Discussion

6.3.1 Results of Field Experiment 1

The PAC was calculated from WSPs sprayed on VR mode using two different classifiers with GDS (Tables 6-1 to 6-4; Figures 6-1 to 6-3; Figures B-1 to B-9; Appendix B). The mean PAC of WSPs placed at wild blueberry and goldenrod spots varied from 0.61% to 43.02% in Londonderry field and from 2.27% to 42.30% in North River II field respectively, using BP-ANN classifier. The quadratic classifier showed that mean PAC of WBB and GR spots varied from 1.65% to 41.78% in Londonderry field and from 3.30% to 36.91% in North River II field, respectively (Table 6-3; 6-4). The results of paired t-test indicated that there was no significant difference between mean PAC of GR spots sprayed uniformly and with BP-ANN classifier at a significance level of 5% in both fields (Table 6-1; 6-2).

Table 6-1: Results of paired t-test for percent area coverage (PAC) of the sprayed targets (GR) and non-targets (WBB) using BP-ANN classifier in Londonderry field.

Application (n)	Minimum (%)	Maximum (%)	Mean (%)	S.D. (%)	P-Value
GR					
VR-T1+T2 (16)	27.68	68.23	43.02	12.76	0.632
UA-T1+T2 (16)	33.50	62.31	45.13	9.03	
WBB					
VR-T1+T2 (16)	0.002	4.860	0.61	1.23	<0.001
UA-T1+T2 (16)	29.36	67.57	45.32	9.08	

VR for variable rate, UA stands for uniform application, T1 for track 1, and T2 for track 2.

Table 6-2: Results of paired t-test for percent area coverage (PAC) of the sprayed targets (GR) and non-targets (WBB) using BP-ANN classifier in North River II field.

Application (n)	Minimum (%)	Maximum (%)	Mean (%)	S.D. (%)	P-Value
GR					
VR-T1+T2 (16)	29.31	74.67	42.30	10.56	0.450
UA-T1+T2 (16)	27.42	62.64	45.48	10.26	
WBB					
VR-T1+T2 (16)	0.003	30.51	2.27	7.56	<0.001
UA-T1+T2 (16)	29.54	68.48	52.68	12.57	

VR for variable rate, UA stands for uniform application, T1 for track 1, and T2 for track 2.

The GR mean PAC differences between BP-ANN classifier and UA mode were 2.11% in Londonderry field and 3.18% in North River II field and therefore were found to be sufficient enough to eradicate goldenrod. The mean PAC of WBB spots was found to be significantly different ($P < 0.05$), when comparing the performance of BP-ANN classifier and uniform applications in both fields (Table 6-1, 6-2). The PAC values of WBB spots were in the range of 0.002% to 4.860% in Londonderry field. The fluctuation in PAC values might be caused by spray drift due to wind gusts (Figure B-1; Appendix B). The average speed of wind gusts on June 4 of 2016 was 7 km hr^{-1} with a maximum of 14 km hr^{-1} directed towards West (National Climate Data and Information Archive, 2016). The WSPs placed at WBB spots in North River II and sprayed with BP-ANN classifier had the highest standard deviation of 7.56% among all other WBB spots sprayed on VR mode. It was observed that a non-target (WBB) WSP was sprayed even with BP-ANN classifier (Figure B-7; Appendix B), thus resulting into high standard deviation. During the data checking, it was found that WSP at a WBB spot number 3 was quite close to GR patch, which may have caused this WSP to get over-sprayed.

The comparison between the quadratic classifier and UA application revealed that there was no significant difference in the mean PAC of GR spots in Londonderry field (Table 6-3). However, in North River II, the mean PAC was found to be marginally non-significant with a relatively lowest p-value among all variably sprayed field tracks (Table 6-4). The reason of lower PAC value was found to be under-sprayed WSPs in first test track of this field (Figure B-5; Appendix B). A WSP at targeted spot (GR) was completely missed with a PAC of only 2.64%. The spray pattern of droplets on this WSP further revealed that a PAC of 2.64% was even due to the drift of sprayed liquid caused by wind. A relatively lower accuracy of achieved by quadratic classifier during laboratory evaluations could be a reason that it was not able to recognize GR as a target spot in real-time field conditions. Additionally, it was also observed that this field was not properly mowed during fall of 2015 compared to Londonderry field, which may also have contributed towards relatively high fluctuation in PAC (SD = 18.65%). The average PAC of 41.78% and 36.91% in Londonderry and North River II fields was sufficient enough to eradicate goldenrod. However, the minimum PAC (2.64%) in GR spots should preferably be higher to minimize the risk of under-spray.

Table 6-3: Results of paired t-test for percent area coverage (PAC) of the sprayed targets (GR) and non-targets (WBB) using quadratic classifier in Londonderry field.

Application (n)	Minimum (%)	Maximum (%)	Mean (%)	S.D. (%)	P-Value
GR					
VR-T1+T2 (16)	21.19	71.41	41.78	15.86	0.484
UA-T1+T2 (16)	33.50	62.31	45.13	9.03	
WBB					
VR-T1+T2 (16)	0.003	4.97	1.65	1.82	<0.001
UA-T1+T2 (16)	29.36	67.57	45.32	9.08	

VR for variable rate, UA stands for uniform application, T1 for track 1, and T2 for track 2.

Table 6-4: Results of paired t-test for percent area coverage (PAC) of the sprayed targets (GR) and non-targets (WBB) using quadratic classifier in North River II field.

Application (n)	Minimum (%)	Maximum (%)	Mean (%)	S.D. (%)	P-Value
GR					
VR-T1+T2 (16)	2.64	79.79	36.91	18.65	0.162
UA-T1+T2 (16)	27.42	62.64	45.48	10.26	
WBB					
VR-T1+T2 (16)	0.001	28.23	3.30	7.21	<0.001
UA-T1+T2 (16)	29.54	68.48	52.68	12.57	

VR for variable rate, UA stands for uniform application, T1 for track 1, and T2 for track 2.

The WBB WSPs sprayed with quadratic classifier showed significantly different PAC ($P < 0.05$) as compared to uniform applications in both fields. A maximum PAC (28.23%) was again due to WSP located at a WBB spot number 3 (Figure B-8; Appendix B). The results of this experiment suggested that both BP-ANN and quadratic classifiers had ability to target goldenrod spots in real-time with a potential of chemical savings in wild blueberry spots. Similar to laboratory evaluations, results of this experiment indicated that BP-ANN classifier outperformed its quadratic counterpart.

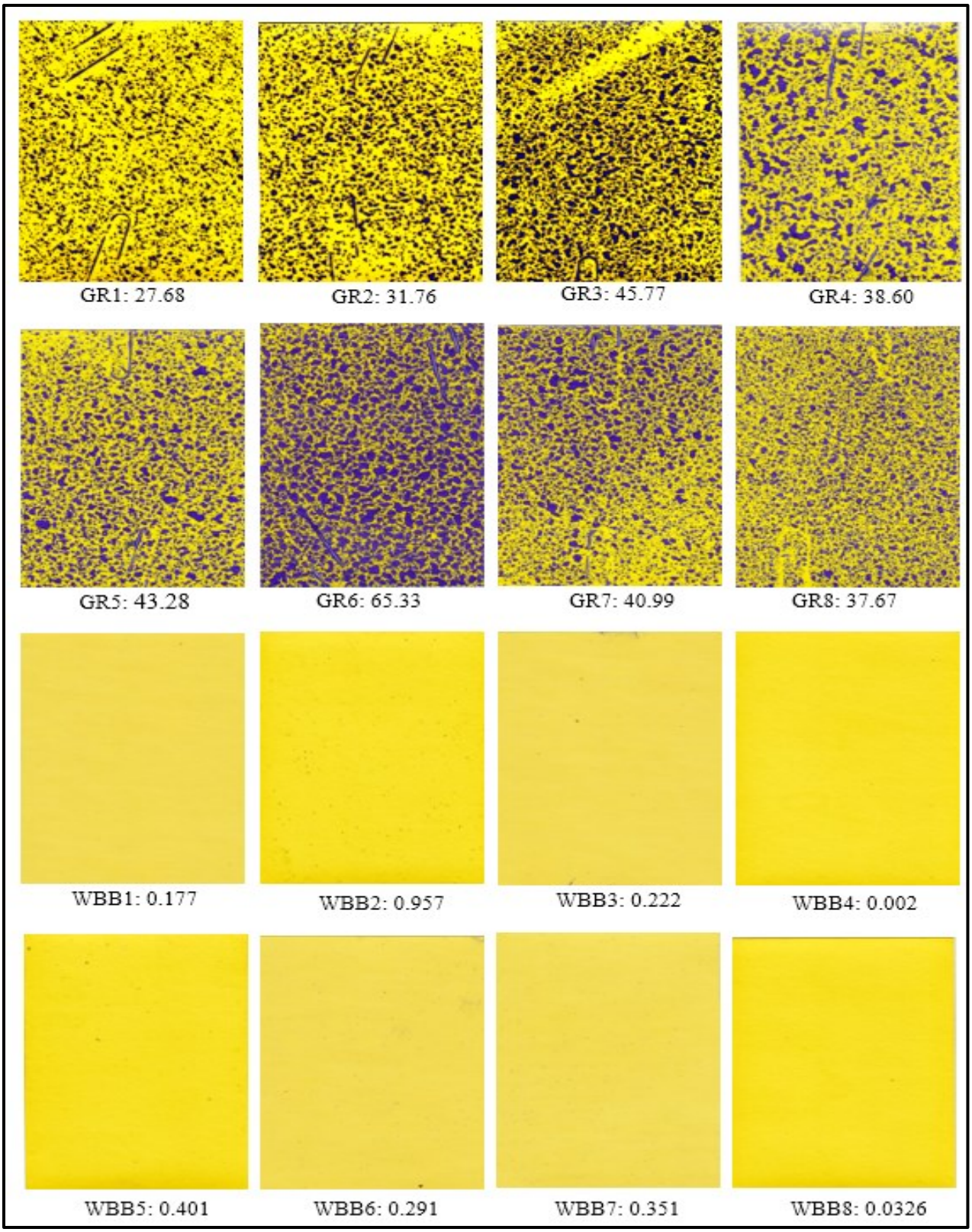

Figure 6-1: First track (T1) of Londonderry field sprayed with BP-ANN classifier (GR represents the selected goldenrod spots and WBB represents selected wild blueberry spots).

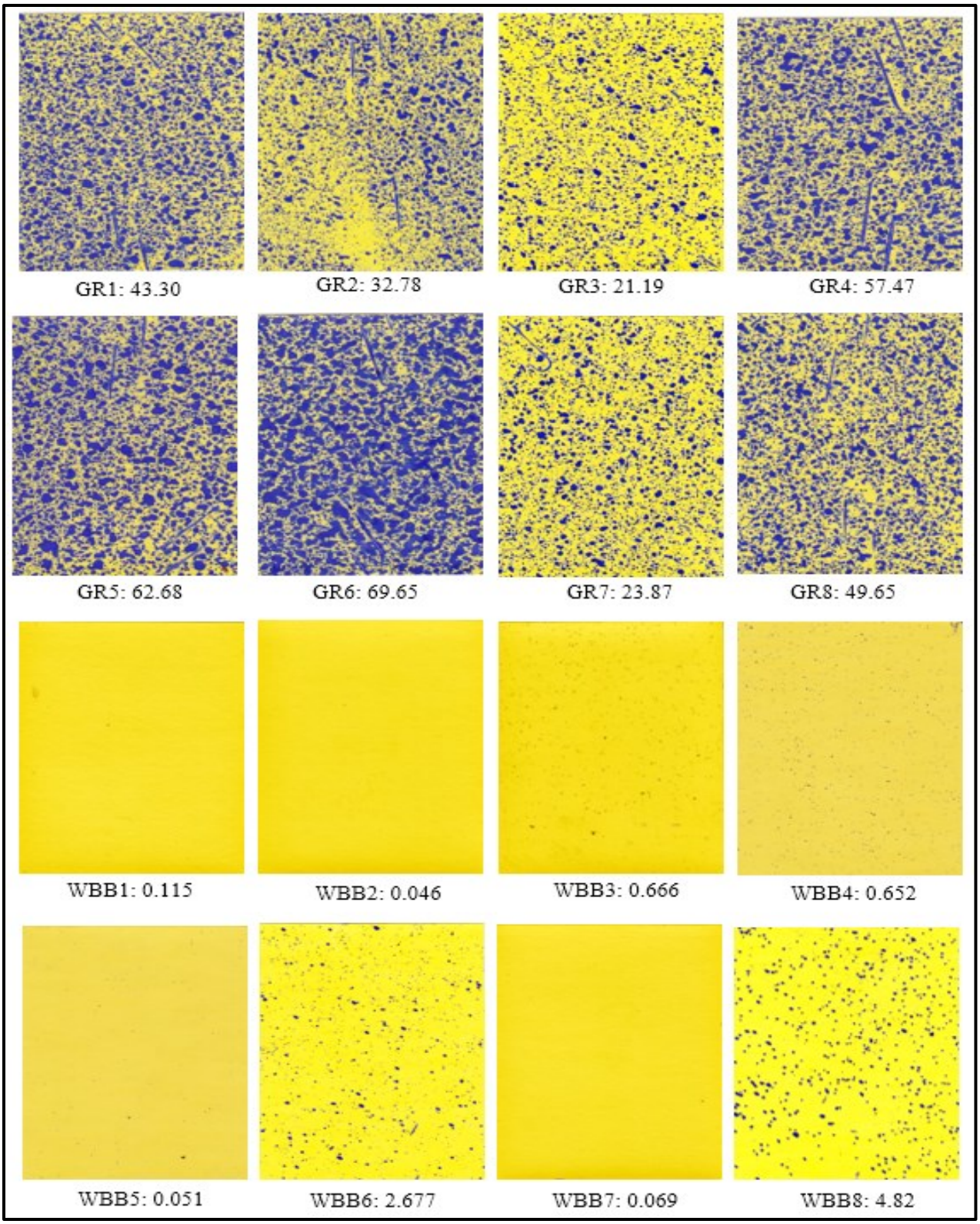

Figure 6-2: First track (T1) of Londonderry field sprayed with quadratic classifier (GR represents the selected goldenrod spots and WBB represents selected wild blueberry spots).

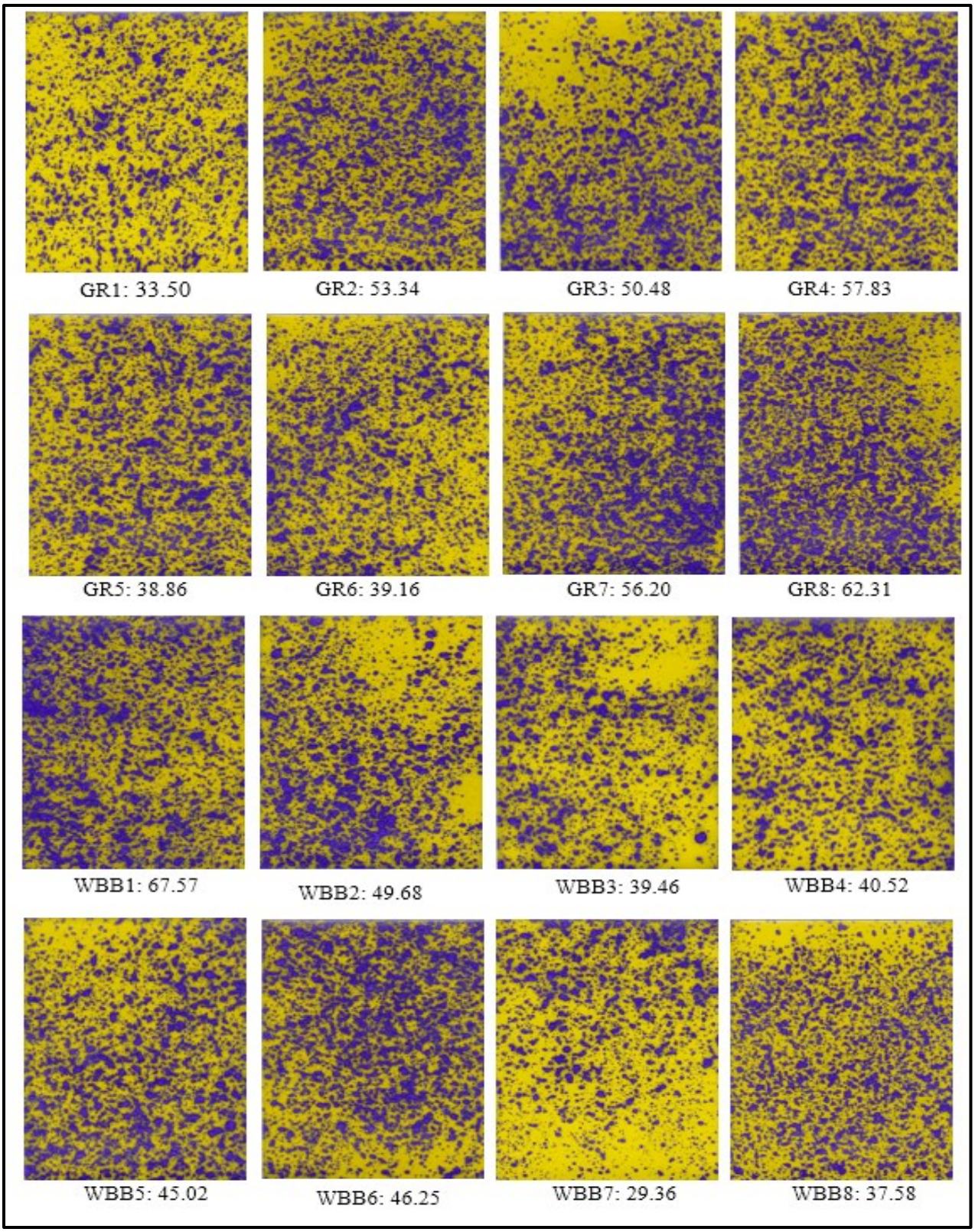

Figure 6-3: First track (T1) of Londonderry field sprayed uniformly (GR represents the selected goldenrod spots and WBB represents selected wild blueberry spots).

6.3.2 Results of Field Experiment 2

The comparison of BP-ANN and quadratic classifier at field scale was done by spraying the test tracks in both fields using a non-permanent dye marker. The CA calculated using ArcGIS was imported in the Minitab 17 to perform group comparison using two sample t-test (Table 6-5). The results of Anderson-Darling (AD) normality test indicated that CA of BP-ANN and quadratic classifier were normally distributed at a significance level of 5% in both fields. The CA obtained from two classifiers were found to have equal variance in both fields and therefore, allowed the use of pooled standard deviation (Sp) for further analysis. The results of two sample t-test revealed that mean CA of sprayed patches with both classifiers was not significantly different at a level of 5%. A total goldenrod coverage of 607.33 m^2 in Londonderry field was sprayed with a mean of 84.95 m^2 using BP-ANN algorithm and 83.5 m^2 using quadratic classifiers. Similarly, a goldenrod coverage of 407.6 m^2 was sprayed with a mean of 56 m^2 using BP-ANN and 48.9 m^2 using quadratic classifiers in North River II field.

Table 6-5: Results of two sample t-test and summary statistics of coverage area in Londonderry and North River II field using BP-ANN and quadratic algorithm.

Application (n)	Minimum (m^2)	Maximum (m^2)	Mean (m^2)	S.D. (m^2)	P-Value
Londonderry					
BP-ANN (9)	12.7	159.2	84.95	51.2	0.919
Quadratic (10)	6.5	163.8	83.54	54.7	
North River II					
BP-ANN (10)	22.1	127.5	56.0	35.4	0.687
Quadratic (12)	4.0	145.9	48.9	43.8	

The subjective analysis of the sprayed maps of two fields indicated that BP-ANN classifier was able to correctly target and spray the goldenrod patches in both fields (Figures 6-4, 6-6). The over-sprayed dye marker before and after goldenrod patches could be due to a 25cm buffer

adjusted in VRC to ensure proper overlap of spray application on the targets (Zaman et al., 2011). The quadratic algorithm also properly targeted goldenrod patches in Londonderry field with only one spot as over-sprayed (Figure 6-5). However, its performance in the North River II field was not as good as BP-ANN with two over-sprayed spots and few missed goldenrod patches (Figure 6-7). It can be seen that the BP-ANN classifier was able to correctly target small goldenrod patches while the quadratic classifier missed these patches and was not able to spray them. The relatively poor performance of quadratic algorithm in North River II field might be due to the poor field management. It was noticed during the field applications that this field was not properly pruned and might increase variability and image noise acquired during spraying.

The goldenrod area and sprayed area were used to calculate the potential and actual chemical savings based on the goldenrod distribution within selected wild blueberry tracks. Results showed that potential savings ranged from 46.71% to 62.77% and 64.38% to 74.83% in Londonderry and North River II field, respectively based on goldenrod patches (Table 6-6; 6-7). Depending upon the classifier, the actual savings ranged from 30.12 to 53.95% and 49.22 to 65.19% in Londonderry and North River II field, respectively. The BP-ANN classifier showed an actual savings of 32.09% and 53.95%, while the quadratic classifier showed 30.12% and 45.33% actual savings in Londonderry field. Similarly, the actual savings from BP-ANN classifier were higher (65.19% and 51.31%) comparative to the quadratic classifier (60.58% and 49.22%) in North River II field. The actual chemical savings from goldenrod patches will not only lower the cost of production but also help to lower environmental hazards (Esau et al., 2014).

Table 6-6: Results of variable rate sprayer chemical savings in goldenrod patches in Londonderry field.

Track	Total Area (m^2)	Goldenrod Patches (m^2)	Sprayed Area (m^2)	Potential Savings (%)	Actual Savings (%)
BP-ANN					
1	671	357.57	455.62	46.71	32.09
2	671	249.76	308.96	62.77	53.95
Quadratic					
1	671	357.57	468.88	46.71	30.12
2	671	249.76	366.59	62.77	45.33

Table 6-7: Results of variable rate sprayer chemical savings in goldenrod patches in North River II field.

Track	Total Area (m^2)	Goldenrod Patches (m^2)	Sprayed Area (m^2)	Potential Savings (%)	Actual Savings (%)
BP-ANN					
1	671	168.87	233.51	74.83	65.19
2	671	238.99	326.25	64.38	51.31
Quadratic					
1	671	168.87	246.45	74.83	60.58
2	671	238.99	340.67	64.38	49.22

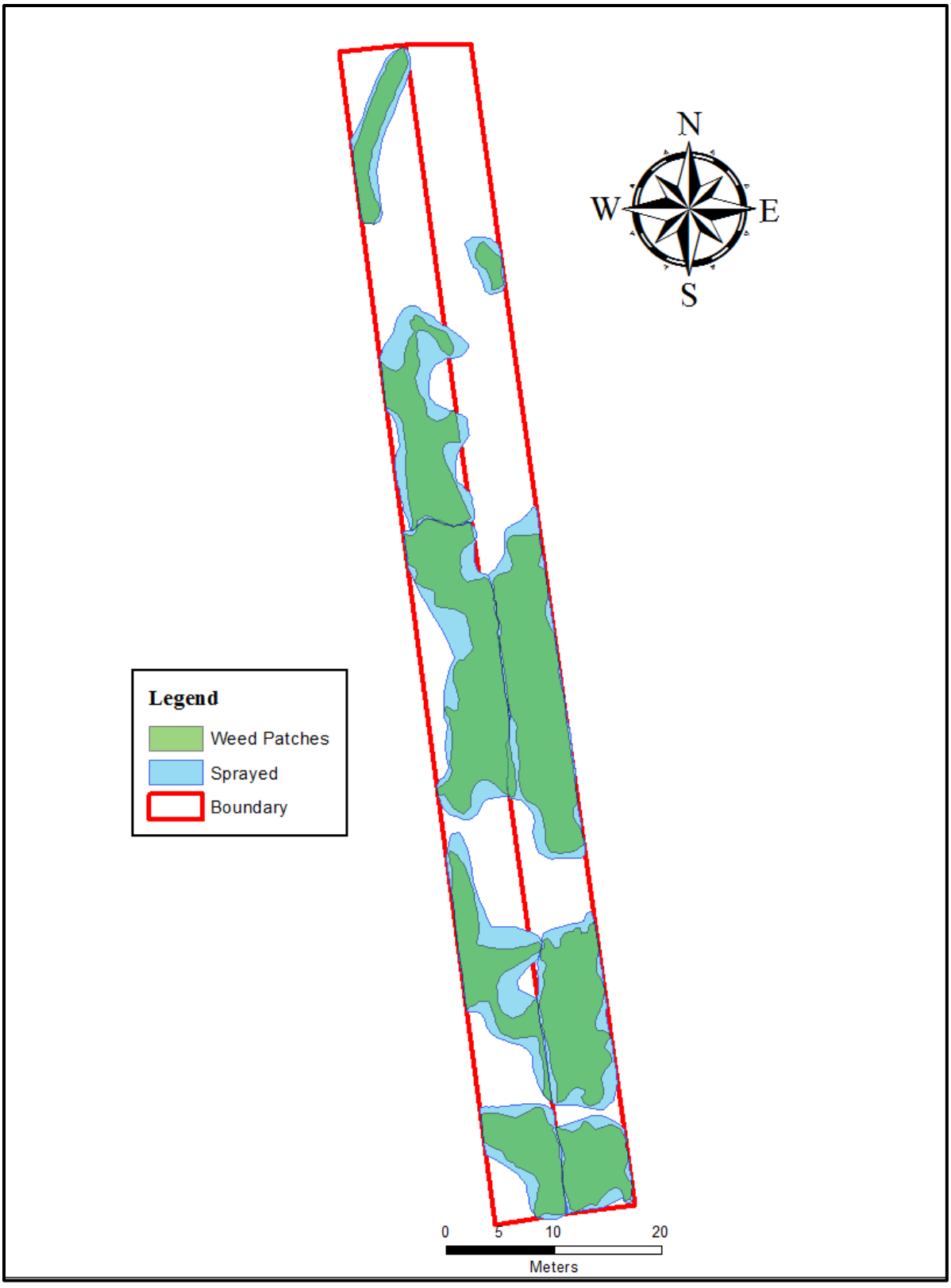

Figure 6-4: Londonderry test tracks layout showing goldenrod coverage and sprayed patches using BP-ANN classifier.

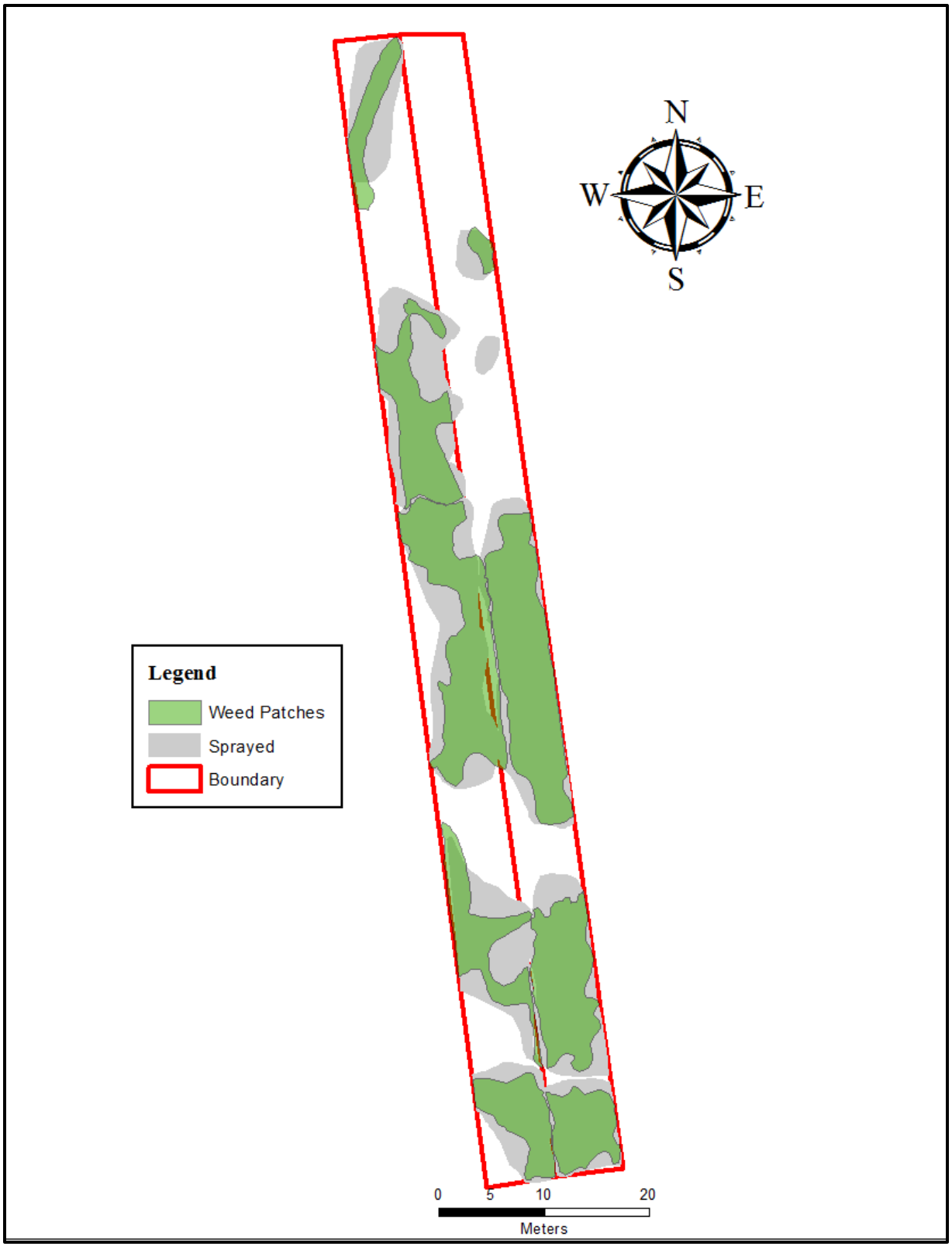

Figure 6-5: Londonderry test tracks layout showing goldenrod coverage and sprayed patches using quadratic classifier.

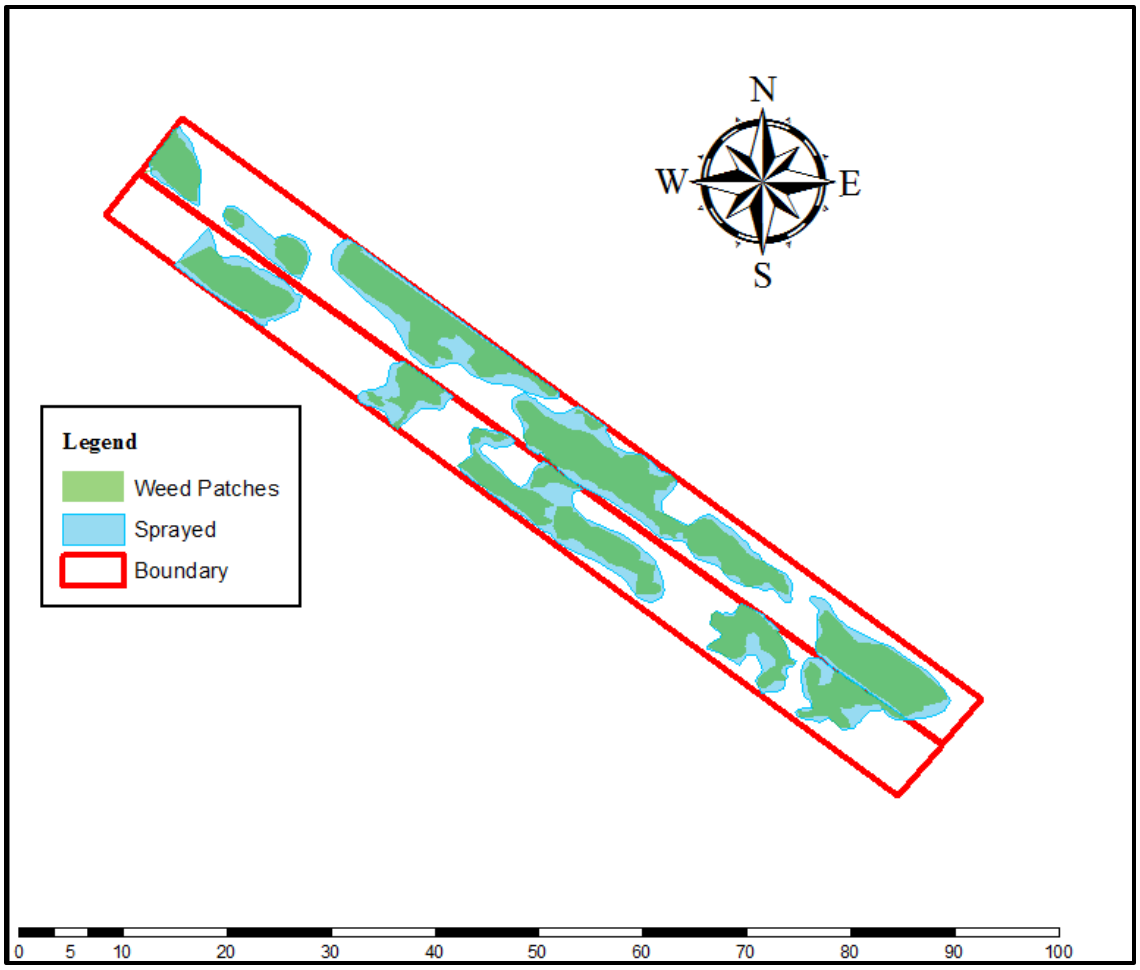

Figure 6-6: North River II test tracks layout showing goldenrod coverage and sprayed patches using BP-ANN classifier.

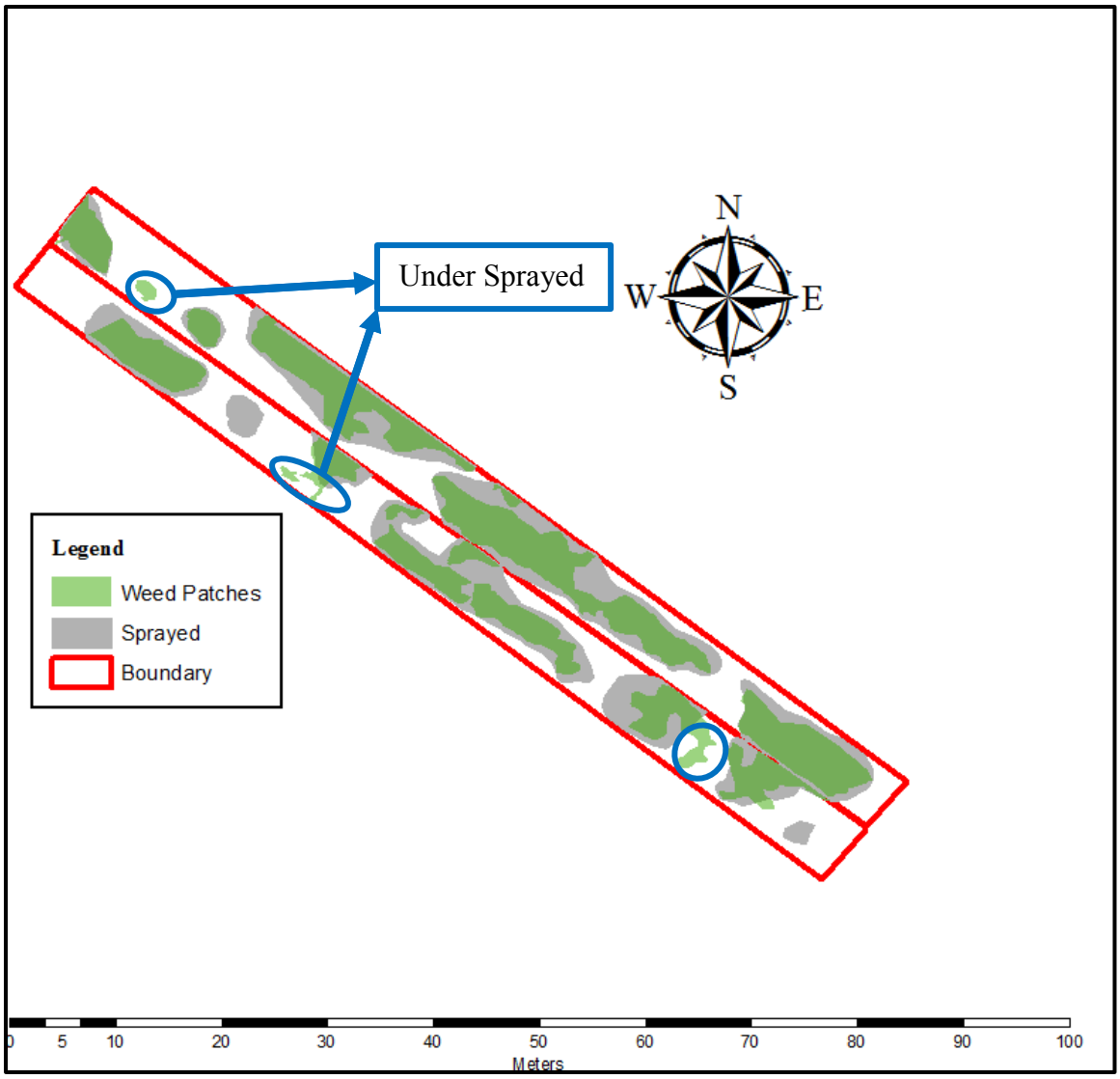

Figure 6-7: North River II test tracks layout showing goldenrod coverage and sprayed patches using quadratic classifier.

6.3.3 Results of Field Experiment during 2017

An experiment was performed by spraying the Callisto® herbicide to compare BP-ANN and quadratic classifiers with respect to UA and CN. Anderson-Darling test of normality indicated that stem height followed a non-normal distribution in Portapique field, while was normally distributed in Robie Glenn. Non-normal data ($P < 0.05$) were normalized using square root transformation for analysis and results were reported by back-transformation to original scale. The

PGP were found to be normal in both fields. Results of ANOVA indicated the significant difference between four treatments (BP-ANN, quadratic, UA, and CN) means for SH and PGP (Table 6-8). The BP-ANN, quadratic, and UA decreased the SH significantly compared to the untreated CN in both fields. Results of LSD further indicated no significant difference between the BP-ANN, quadratic, and UA at Portapique, however in Robie Glenn field quadratic classifier was significantly different as compared to BP-ANN and UA. The PGP was reduced significantly by the application of Callisto® using BP-ANN, quadratic, and UA when compared with CN (Figure 6-8). The results of LSD indicated no significant difference between BP-ANN, quadratic, and UA with mean values of 4.11, 5.89, 3.72, and 9.83, 11.33, 9.50 in Portapique and Robie Glenn fields, respectively. Based on the results of ANOVA and LSD, it can be concluded that developed classifiers (BP-ANN and quadratic) along with Callisto® have significant effect on goldenrod stem height and percentage of green pixels.

Table 6-8: Results of ANOVA for GD, SH, and PGP to compare the damage caused by BP-ANN and quadratic classifiers relative to the UA and CN in two different fields.

		Portapique		Robie Glenn	
Treatment (n)	Goldenrod damage parameters	Mean	P-Value	Mean	P-Value
BP-ANN (6)	SH (cm)	9.93 ± 1.28 b	<0.001	9.03 ± 0.91 c	<0.001
Quadratic (6)	SH (cm)	10.23 ± 1.56 b		11.53 ± 1.25 b	
UA (6)	SH (cm)	9.86 ± 1.17 b		8.49 ± 1.15 c	
CN (6)	SH (cm)	16.83 ± 1.23 a		19.15 ± 1.58 a	
BP-ANN (6)	PGP	4.11 ± 2.32 b	<0.001	9.83 ± 5.99 b	<0.001
Quadratic (6)	PGP	5.89 ± 5.1 b		11.33 ± 6.87 b	
UA (6)	PGP	3.72 ± 2.72 b		9.50 ± 4.72 b	
CN (6)	PGP	42.44 ± 12.16 a		47.39 ± 14.17 a	

Means with no letters shared in same column are statistically different at P= 0.05.

(a) (b)

Figure 6-8: Percentage of green pixels, (a) Callisto® application on the goldenrod using BP-ANN, (b) Untreated control.

The results of Kruskal-Wallis H test indicated that DR was significantly different among different treatment means (BP-ANN, quadratic, UA, and CN) in both fields (Table 6-9). The UA resulted into the highest damage to goldenrod, followed by BP-ANN and quadratic in both fields (Figure 6-8). The results of Dunn-Bonferoni pairwise post-hoc test indicated no significant difference between UA and BP-ANN treatments, whereas all other treatment pairs were found to be significantly different from others (Table 6-9). The DR caused by quadratic classifier was found to be significantly lower than UA and BP-ANN in both fields. As control was not treated with Callisto®, therefore no damage was observed in CN plots. On the basis of SH, PGP, and DR results, it can be concluded that BP-ANN classifier performed better than the quadratic classifier. Furthermore, results also suggested that the performance of BP-ANN classifier was comparable to the UA.

Table 6-9: Results of Kruskal-Wallis H test for goldenrod DR to compare the performance of BP-ANN and quadratic classifiers relative to the UA and CN in two different fields.

Treatment (n)	Minimum	Maximum	Mean	S.D.	P-Value
Portapique					
BP-ANN (6)	75.00	95.00	85.83 ^{NS}	7.36	<0.001
Quadratic (6)	60.00	90.00	81.60	11.14	
UA (6)	70.00	95.00	86.16 ^{NS}	9.31	
CN (6)	0.00	0.00	0.00	0.00	
Robie Glenn					
BP-ANN (6)	70.00	90.00	80.83 ^{NS}	6.83	<0.001
Quadratic (6)	65.00	85.00	72.50	8.22	
UA (6)	70.00	90.00	81.66 ^{NS}	6.65	
CN (6)	0.00	0.00	0.00	0.00	

Treatment pairs with NS are not significantly different at P= 0.05.

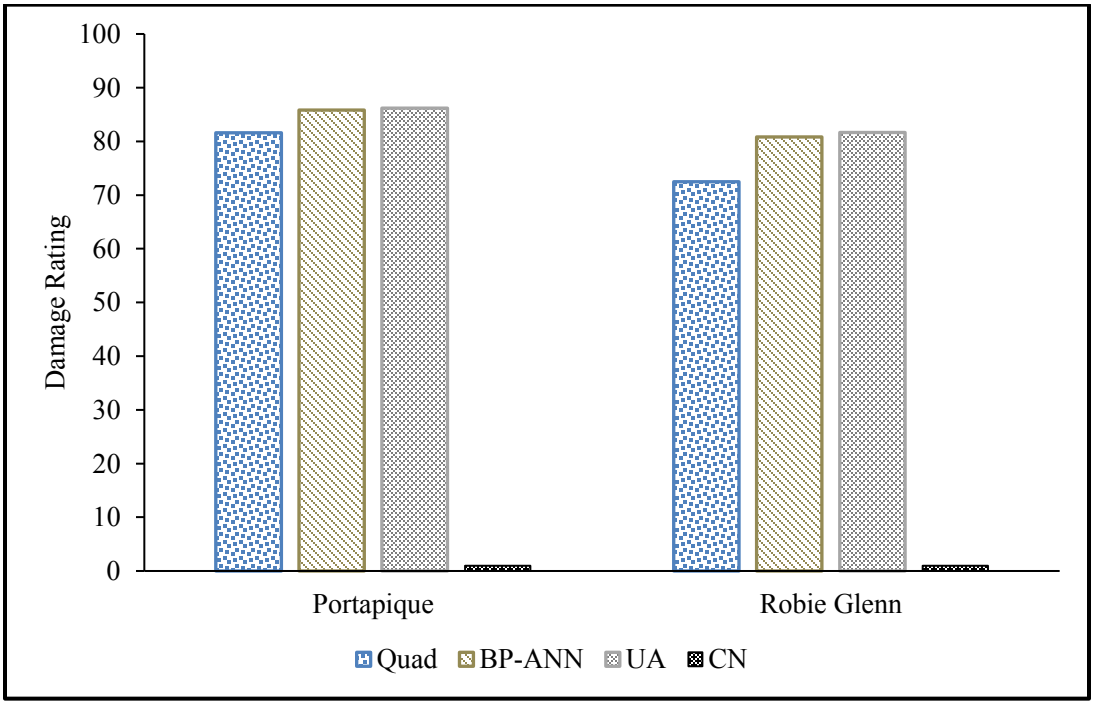

Figure 6-9: Mean goldenrod damage ratings caused by different treatments at Portapique and Robie Glenn fields.

6.4 Conclusions

The GDS with two different classifiers was evaluated and compared with UA in real field conditions. Results of field experimentation indicted that the developed system correctly targets goldenrod and triggers the nozzles to "off" state in wild blueberry zones. Results of PAC experiment indicated that quadratic classifier resulted in under-sprayed WSPs in one track of North River II field, while the BP-ANN targeted the goldenrod WSPs in both fields. The performance of quadratic and the BP-ANN classifiers was further compared by spraying blue coloured spray pattern indicator dye with water in selected blueberry tracks. It was found that CA of two classifiers was not statistically significant in both fields. The BP-ANN classifier showed a maximum water savings of 65% compared to 61% with quadratic classifier depending upon the goldenrod coverage with 25cm buffer to ensure proper application overlap. The Callisto® application helped to halt goldenrod growth, thereby resulting in reduced shoot height and percentage of green pixels along with increased damage ratings. Results of SH, PGP, and DR indicated no significant difference between BP-ANN and UA application. Results suggested that developed CCM algorithm with a BP-ANN classifier has potential of targeting the goldenrod in a site-specific manner. The visual performance of BP-ANN as indicated by WSPs, dye marker, and Callisto® experimentation was in line with model training and evaluation results reported in chapter 5. Based on the results of field evaluation it can be concluded that both BP-ANN and quadratic classifiers can be used for real-time application of Callisto® on goldenrod. However, the BP-ANN model showed more promising results compared to quadratic classifier.

CHAPTER 7: CONCLUSIONS AND RECOMMENDATIONS

7.1 Conclusions

The overall goal of this research was to develop and evaluate a graphical user interface based goldenrod detection system using CCMs as image processing algorithm and machine learning procedures to apply herbicide in wild blueberry fields. The hardware used for the evaluation of goldenrod detection system consisted of four µEye CMOS colour cameras, Garmin® GPS receiver, ruggedized field computer, LMC, LabJack® U3-HV I/O module, an 8-channel computerized VRC, and 8-solenoid valves assisted nozzles. The developed goldenrod detection system was evaluated by operating it with hardware through a UTV for real-time application of water and Callisto® 480SC in selected wild blueberry fields during summer of 2016 and 2017. Results of field evaluations using WSPs, blue coloured spray pattern indicator dye with application maps, and goldenrod damage ratings revealed that the developed goldenrod detection system has potential of targeting the goldenrod in a site-specific manner. Results of laboratory evaluation suggested that developed CCM algorithm with a BP-ANN classifier has ability to target the goldenrod with an accuracy of 97%, thereby can be used to apply Callisto® adequately only on targeted goldenrod patches.

The effect of different image parameters on computational complexity and goldenrod identification accuracy of CCMs was tested by studying three different image reading methods (get pixel, unsafe pointers, and Marshal.copy), six intensity levels (8, 16, 32, 64, 128, and 256), and seven image sizes (16 × 16, 32 × 32, 64 × 64, 128 × 128, 256 × 256, 512 × 512, and 1024 × 1024) on 2244 AOI and 2244 full frame field images. One-way ANOVA with Tukey's HSD test was performed for analyzing statistically different time measurement means. The Marshal.copy method of C# programming language was found to be most suitable for reading the image from

computer RAM as it took the least time. Images with 256 intensity levels took the highest processing time and were able to achieve an overall accuracy of 94% on test images. The 256 intensity levels were selected for the actual spray using goldenrod detection system in wild blueberry fields. A unit image size of 128 × 128 pixels minimized the computational time for processing an AOI image (768 × 128) with current camera settings and was adopted for real-time applications because of the highest (91%) overall classification accuracy on test data.

The quantitative textural features extracted from CCMs can aid in classifying the members of goldenrod and wild blueberry data groups by predicting the underlying relationships between these features and respective group. Feature reduction resulted in the reduction of 39 to only 8 of H and S features with complete exclusion of features from intensity colour plane. Comparison of statistical quadratic and linear classifiers revealed that quadratic performed better than linear classifiers for all reduced DMs. The BP-ANN network training on trial and error basis indicated that optimal network with the highest classification accuracy consisted of nine neurons on two hidden layers, a learning rate of 0.085, online training mode, a momentum term of 0.80, a tanh sigmoid mathematical function with linear function at output layer, and epoch size of 2,500. Results suggested that developed CCM algorithm with the BP-ANN classifier outperformed the statistical quadratic counterpart in terms of classification accuracy on both training and test datasets. The DM-HSI_{SD} model achieved the highest classification accuracy for both statistical quadratic and the BP-ANN classifiers. These classifiers trained on DM-HSI_{SD} model was thus selected for real-time field application tests.

In order to test and evaluate the performance of CCMs with the statistical and BP-ANN classifiers, two experiments were conducted in summer of 2016 in two commercial wild blueberry fields. Two test tracks (6.1 m × 110 m) were randomly constructed at each site and track boundaries

along with goldenrod patches were manually mapped. Sixteen WSPs were randomly placed in each test track. Results of PAC experiment indicated that quadratic classifier resulted in under-sprayed WSPs in one track of North River II field, while the BP-ANN targeted the goldenrod WSPs in both fields. The performance of statistical quadratic and the BP-ANN classifiers was further compared by spraying blue coloured spray pattern indicator dye with water in selected blueberry tracks. It was found that CA of two classifiers were not statistically significant in both fields. The water application with the BP-ANN classifier showed a maximum 65% savings, while quadratic classifier resulted in 61% savings depending upon the goldenrod coverage with 25 cm buffer to ensure proper application overlap. The Callisto® application helped to halt goldenrod growth, thereby resulting in reduced shoot height and percentage of green pixels along with increased damage ratings. Results of SH, PGP, and DR indicated no significant difference between BP-ANN and UA application. It can be concluded that developed CCM algorithm with a BP-ANN classifier has potential of targeting the goldenrod in a site-specific manner and can be operated at the growers recommended speed of 6 km hr^{-1}.

7.2 Recommendations

It is proposed that current goldenrod detection system with four cameras for 6.1m of spray coverage can be upgraded to complement a larger commercial size sprayer for spot-application on goldenrod. The transfer of GDS to a commercial sprayer may also include the removal of U3-HV I/O module from the hardware, thereby allowing for direct serial communication between the image processing computer and VRC. The developed GDS can be modified to detect other weeds in wild blueberry fields. The modification of GDS can help to transfer the technology to other fruit and vegetable cropping system for detecting and targeting the in-season weeds, thereby allowing the farmers to increase farm gate value with reduced environmental risk. Deep convolution neural

networks and other advanced techniques can also be used for modification in existing system to detect the goldenrod and other weeds in wild blueberry fields.

REFERENCES

Amadasun, M. and King, R. (1989). Textural features corresponding to textural properties. IEEE Transactions on Systems, Man, and Cybernetics. 19(5): 1264-1274.

Bai, X. D., Cao, Z. G., Wang, Y., Yu, Z. H., Zhang, X. F., and Li, C. N. (2013). Crop segmentation from images by morphology modeling in the CIE L* a* b* color space. Computers and Electronics in Agriculture. 99: 21-34.

Bennett, J. and Khotanzad, A. (1998). Multispectral random field models for synthesis and analysis of color images. IEEE Transactions on Pattern Analysis and Machine Intelligence. 20(3): 327-332.

Bishop, C. (2007). Pattern Recognition and Machine Learning (Information Science and Statistics). Springer, New York, NY, USA.

Blake, A. and Zisserman, A. (1987). Visual reconstruction. MIT Press, Cambridge, MA, USA.

Blostein, D., and Ahuja, N. (1989). Shape from texture: Integrating texture-element extraction and surface estimation. IEEE Transactions on Pattern Analysis and Machine Intelligence. 11(12): 1233-1251.

Boyd, N. and White, S. (2010). PRE and POST herbicides for management of goldenrods (*Solidago spp*.) and black bulrush (*Scirpus atrovirens*) in wild blueberry. Weed Technology. 24(4): 446-452.

Brady, M. and Xie, F. (1996). Feature Selection for Texture Segmentation. In: Bowyer K. W. and Ahuja A. (Eds.). Advances in Image Understanding. IEEE Computer Society Press, Los Alamitos, CA, USA.

Burks, T. F. (1997). Color Image Texture Analysis and Neural Network Classification of Weed Species. Ph.D. Dissertation, University of Kentucky, Lexington, Kentucky, USA.

Burks, T., Shearer, S., and Payne, F. (2001). Classification of weed species using color texture features and discriminant analysis. Transactions of the ASAE. 43(2): 441-448.

Burks, T., Shearer, S., Heath, J., and Donohue, K. (2005). Evaluation of neural-network classifiers for weed species discrimination. Biosystems Engineering. 91(3): 293-304.

Campbell, J. B. (1996). Introduction to Remote-Sensing. The Guilford Press, London, UK.

Carlucci, L. (1972). A formal system for texture languages. Pattern Recognition. 4(1): 53-72.

Chang, Y. K., Zaman, Q. U., Schumann, A. W., Esau, T. J., and Ayalew, A. (2012a). Development of color co-occurrence based machine vision algorithms for wild blueberry fields. Applied Engineering in Agriculture. 28(3): 315-323.

Chang, Y. K., Zaman, Q., Farooque, A. A., Schumann, A. W., and Percival, D. C. (2012b). An automated yield monitoring system II for commercial wild blueberry double-head harvester. Computers and Electronics in Agriculture. 81: 97-103.

Chang, Y. K., Zaman, Q. U., Esau, T. J., and Schumann, A. W. (2014). Sensing system using digital photography technique for spot-application of herbicide in pruned wild blueberry fields. Applied Engineering in Agriculture. 30(2): 143-152.

Chang, Y. K. (2016, May 22). Personal Interview.

Chellappa, R. and Chatterjee, S. (1985). Classification of textures using Gaussian Markov Random fields. IEEE Transactions on Acoustics, Speech and Signal Processing. 33(4): 959-963.

Cho, S., Lee, D., and Jeong, J. (2002). Weed–plant discrimination by machine vision and artificial neural network. Biosystems Engineering. 83(3): 275-280.

Coggins, J. M. and Jain, A. K. (1985). A spatial filtering approach to texture analysis. Pattern Recognition Letters. 3(3): 195-203.

Cohen, F. S. and Cooper, D. B. (1987). Simple parallel hierarchical and relaxation algorithms for segmenting noncausal Markovian Random fields. IEEE Transactions on Pattern Analysis and Machine Intelligence. 9(2): 195-219.

Cohen, L. (1989). Time-frequency distributions-a review. Proceedings of the IEEE. 77(7): 941-981. doi: 10.1109/5.30749.

Cross, G. R. and Jain, A. K. (1983). Markov Random field texture models. IEEE Transactions on Pattern Analysis and Machine Intelligence. 5(1): 25-39.

C# Programming Guide, 2015. Microsoft Developer Network. Retrieved from https://msdn.microsoft.com/en-CA/library/t2yzs44b.aspx. Date accessed: November 15, 2016.

Daugman, J. G. (1985). Uncertainty relation for resolution in space, spatial frequency, and orientation optimized by two-dimensional visual cortical filters. Journal of Optical Society of America. 2(7): 1160-1169.

Darling, E. M. and Joseph, R. D. (1968). Pattern recognition from satellite altitudes. IEEE Transactions on System, Man, Cybernetics. 4(1): 30-47.

Derin, H. and Elliott, H. (1987). Modeling and segmentation of noisy and textured images using Gibbs random fields. IEEE Transactions on Pattern Analysis and Machine Intelligence. 9(1): 39-55.

de Castro, A. I., López-Granados, F., and Jurado-Expósito, M. (2013). Broad-scale cruciferous weed patch classification in winter wheat using QuickBird imagery for in-season site-specific control. Precision Agriculture. 14(4): 392-413.

Deguchi, K. and Morishita, I. (1978). Linear estimation techniques. IEEE Transactions on Computers. 27(8): 739-745.

Eaton, L. J. and Nams, V. O. (2006). Second cropping of wild blueberries-effects of management practices. Canadian Journal of Plant Science. 86(4): 1189-1195.

Esau, T. J. (2012). Development and Evaluation of a Prototype Variable Rate Sprayer for Spot-Application of Agrochemicals in Wild Blueberry Fields. M.Sc. Thesis, Dalhousie University, Halifax, Nova Scotia, Canada.

Esau, T. J., Zaman, Q. U., Chang, Y. K., Schumann, A. W., Percival, D. C., and Farooque, A. A. (2014). Spot-application of fungicide for wild blueberry using an automated prototype variable rate sprayer. Precision Agriculture. 15(2): 147-161.

El-Faki, M., Zhang, N., and Peterson, D. (2000). Weed detection using color machine vision. Transactions of the ASAE. 43(6): 1969-1978.

Farooque, A. A., Chang, Y. K., Zaman, Q. U., Groulx, D., Schumann, A. W., and Esau, T. J. (2013). Performance evaluation of multiple ground based sensors mounted on a commercial wild blueberry harvester to sense plant height, fruit yield and topographic features in real-time. Computers and Electronics in Agriculture. 91: 135-144.

Franz, E., Gebhardt, M., and Unklesbay, K. (1991). Shape description of completely visible and partially occluded leaves for identifying plants in digital images. Transactions of the ASAE. 34(2): 673-681.

Galloway, M. M. (1975). Texture analysis using gray level run lengths. Computer graphics and image processing. 4(2): 172-179.

Gebhardt, S., Schellberg, J., Lock, R., and Kühbauch, W. (2006). Identification of broad-leaved dock (*Rumex obtusifolius L.*) on grassland by means of digital image processing. Precision Agriculture. 7(3): 165-178.

Geman, S. and Geman, D. (1984). Stochastic relaxation, Gibbs distributions, and the Bayesian restoration of images. IEEE Transactions on Pattern Analysis and Machine Intelligence. 6(6): 721-741.

Glass, V. M. and Percival, D. (2000). Challenges facing pollination and fruit set in indigenous blueberries (*Vaccinium angustifolium Ait.*). Journal of American Pomological Society. 54: 44-47.

Gonzalez, R. and Woods, R. (2008). Digital image processing: Pearson Prentice Hall, Upper Saddle River, NJ, USA.

Guyer, D. E., Miles, G., Schreiber, M., Mitchell, O., and Vanderbilt, V. (1986). Machine vision and image processing for plant identification. Transactions of the ASAE. 29(6): 1500-1507.

Guyer, D., Miles, G., Gaultney, L., and Schreiber, M. (1993). Application of machine vision to shape analysis in leaf and plant identification. Transactions of the ASAE. 36(1): 163-171.

Hall, I. V., Aalders, L. E., Nickerson, N. L., and Vander Kloet, S. P. (1979). Biological flora of Canada. 1. *Vaccinium angustifolium Ait.*, Sweet lowbush blueberry. Canadian Field-Naturalist. 93: 415-430.

Haralick, R. M., Shanmugam, K., and Dinstein, I. H. (1973). Textural features for image classification. IEEE Transactions on Systems, Man and Cybernetics. 3(6): 610-621.

Haralick, R. M. (1979). Statistical and structural approaches to texture. Proceedings of the IEEE. 67(5): 786-804. doi: 10.1109/PROC.1979.11328.

Haralick, R. M. (1993) Performance Characterization in Computer Vision. In: Chetverikov, D. and Kropatsch, W. (Eds.), Computer Analysis of Images and Patterns (pp. 1-9). Springer, Berlin, Heidelberg. doi: 10.1007/3-540-57233-3_1.

Jensen, K. I. and Yarborough, D. E. (2004). An overview of weed management in the wild low bush blueberry—past and present. Small Fruits Review. 3(4): 229-255.

Jeon, H. Y., Tian, L. F., and Zhu, H. (2011). Robust crop and weed segmentation under uncontrolled outdoor illumination. Sensors. 11(6): 6270-6283.

Julesz, B. (1962). Visual pattern discrimination. IRE Transactions on Information Theory. 8(2): 84-92.

Kavdır, İ. (2004). Discrimination of sunflower, weed and soil by artificial neural networks. Computers and Electronics in Agriculture. 44(2): 153-160.

Kennedy, K. J., Boyd, N. S., and Nams, V. O. (2010). Hexazinone and fertilizer impacts on sheep sorrel (*Rumex acetosella*) in wild blueberry. Weed Science. 58(3): 317-322.

Kim, D. G., Burks, T. F., Qin, J., and Bulanon, D. M. (2009). Classification of grapefruit peel diseases using color texture feature analysis. International Journal of Agricultural and Biological Engineering. 2(3): 41-50.

Kinsman, G. (1993). The History of the Low Bush Blueberry Industry in Nova Scotia, 1950-1990. Nova Scotia Dept. of Agriculture and Marketing, Truro, NS.

Klecka, W. R. (1980). Discriminant analysis. Sage University Press, London, UK.

Lachenbruch, P. A. (1975). Discriminant Analysis. Macmillan publishing Co, New York, NY, USA.

Lamm, R., Slaughter, D., and Giles, D. (2002). Precision weed control system for cotton. Transactions of the ASAE. 45(1): 231.

LeCun, Y. A., Bottou, L., Orr, G. B., and Müller, K. (2012). Efficient BackProp. Retrieved from: http://link.springer.com/chapter/10.1007%2F3-540-49430-8_2. Date accessed. March 16, 2017.

Lamb, D. and Brown, R. (2001). Remote-sensing and mapping of weeds in crops. Journal of Agricultural Engineering Research. 78(2): 117-125.

Lee, W. S., Slaughter, D., and Giles, D. (1999). Robotic weed control system for tomatoes. Precision Agriculture. 1(1): 95-113.

Levine, M. D. (1985). Vision in Man and Machine. McGraw-Hill, New York, NY, USA.

Mallat, S. G. (1989). Multifrequency channel decompositions of images and wavelet models. IEEE Transactions on Acoustics, Speech and Signal Processing. 37(12): 2091-2110.

Manjunath, B., and Chellappa, R. (1991). Unsupervised texture segmentation using Markov Random field models. IEEE Transactions on Pattern Analysis and Machine Intelligence. 13(5): 478-482.

Mao, W., Wang, Y., and Wang, Y. (2003). Real-time detection of between-row weeds using machine vision. ASAE Paper NO. 03-1004. St. Joseph, MI, USA.

Marchant, J. and Onyango, C. M. (2003). Comparison of a Bayesian classifier with a multilayer feed-forward neural network using the example of plant/weed/soil discrimination. Computers and Electronics in Agriculture. 39(1): 3-22.

Marchant, J. A., Tillett, N., and Onyango, C. M. (2004). Dealing with color changes caused by natural illumination in outdoor machine vision. An International Journal of Cybernetics and Systems. 35(1): 19-33.

Materka, A. and Strzelecki, M. (1998). Texture Analysis Methods–A Review. Technical university of Lodz, COST B11 Report of Institute of Electronics, Lodz, Poland. Retrieved from: http://www.eletel.p.lodz.pl/programy/cost/pdf_1.pdf. Date Accessed: March 16, 2017.

McCormick, B. H. and Jayaramamurthy, S. N. (1974). Time series model for texture synthesis. International Journal of Computer and Information Sciences. 3(4): 329-343.

McCully, K. V., Sampson, M. G., and Watson, A. K. (1991). Weed survey of Nova Scotia lowbush blueberry (Vaccinium angustifolium) fields. Weed Science. 3(2): 180-185.

Meyer, G., Mehta, T., Kocher, M., Mortensen, D., and Samal, A. (1998). Textural imaging and discriminant analysis for distinguishing weeds for spot spraying. Transactions of the ASAE. 41(4): 1189-1195.

Meyer, G., Hindman, T., Jones, D., and Mortensen, D. (2004). Digital camera operation and fuzzy logic classification of uniform plant, soil, and residue color images. Applied Engineering in Agriculture. 20(4): 519-526.

Meyer, G. E. (2011). Machine vision identification of plants. In: Krezhova, D. (Ed.), Recent Trends for Enhancing the Diversity and Quality of Soybean Products (pp. 401-420). InTech, Rijeka, Croatia. doi: 10.5772/1005.

Mirchandani, G., and Cao, W. (1989). On hidden nodes for neural nets. IEEE Transactions on Circuits and Systems. 36(5): 661-664.

Morrison, D. F. (1976). Multivariate Statistical Methods, 2nd Edition. McGraw-Hill, New York, NY.

Neto, J. C. and Meyer, G. E. (2005). Crop Species Identification Using Machine Vision of Computer Extracted Individual Leaves. In: Chen, Y-R., Meyer, G. E., and Tu S. I. (Eds.), Optical Sensors and Sensing Systems for Natural Resources and Food Safety and Quality (pp. 1-11). SPIE Digital Library Press, Cardiff, UK. doi: 10.1117/12.631715.

Panjwani, D. K. and Healey, G. (1995). Markov random field models for unsupervised segmentation of textured color images. IEEE Transactions on Pattern Analysis and Machine Intelligence. 17(10): 939-954.

Pao, Y. (1989). Adaptive Pattern Recognition and Neural Networks. Addison-Wesley Publishing Company, Inc., Boston, MA.

Pentland, A. P. (1984). Fractal-based description of natural scenes. IEEE Transactions on Pattern Analysis and Machine Intelligence. 6(6): 661-674.

Perez, A., Lopez, F., Benlloch, J., and Christensen, S. (2000). Colour and shape analysis techniques for weed detection in cereal fields. Computers and Electronics in Agriculture. 25(3): 197-212.

Percival, D., Brown, G., and Harrington, T. (2014). Improvements in vegetation management practices in wild blueberry (*Vaccinium angustifolium Ait*.) using precision agriculture

technologies. Proceedings of the North American Blueberry Research and Extension Workers Conference. 101: 281-286. doi: 10.7282/T3WH2RNQ.

Pesticide Risk Reduction Program (PMRA, 2005). Crop Profile for Lowbush Blueberry in Canada. Retrieved from: http://publications.gc.ca/collections/collection_2009/agr/A118-10-8-2007E.pdf. Date accessed: March 16, 2017.

Pesticide Risk Reduction Program (PMRA, 2014). Crop Profile for Lowbush Blueberry in Canada. Retrieved from: http://www.publications.gc.ca/site/eng/9.829861/publication.html. Date accessed: March 16, 2017.

Pydipati, R., Burks, T., and Lee, W. (2005). Statistical and neural network classifiers for citrus disease detection using machine vision. Transactions of American Society of Agricultural Engineers. 48(5): 2007.

Povlow, B. R. and Dunn, S. M. (1995). Texture classification using non-casual Hidden Markov models. IEEE Transactions on Pattern Analysis and Machine Intelligence. 17(10): 1010-1014.

Ramsey, H. (2015). Development and Implementation of Hay Yield Monitoring Technology. M.Sc. Thesis, Clemson University, Clemson, South Carolina, USA.

Romeo, J., Guerrero, J. M., Montalvo, M., Emmi, L., Guijarro, M., Gonzalez-de-Santos, P., and Pajares, G. (2013). Camera sensor arrangement for crop/weed detection accuracy in agronomic images. Sensors. 13(4): 4348-4366.

Rosenfeld, A. and Troy, E. (1970). Visual Texture Analysis. Retrieved from: https://books.google.ca/books/about/Image_Modeling.html?id=yzejBQAAQBAJ. Date accessed: March 16, 2017.

Rosenfeld, A. and Thurston, M. (1971). Edge and curve detection for visual scene analysis. IEEE Transactions on Computers. 100(5): 562-569.

Rosenfeld, A. and Weszka, J. S. (1976). Picture recognition. Springer, New York, NY, USA.

Rosenfeld, R. and Kak, A. (1982). Digital Picture Processing. Academic Press Orlando, FL, USA.

Roy, S. K., Shibusawa, S., and Okayama, T. (2006). Textural analysis of soil images to quantify and characterize the spatial variation of soil properties using a real-time soil sensor. Precision Agriculture. 7(6): 419-436.

SAS 9.3 User's Guide (2011). Retrieved from: https://support.sas.com/documentation/cdl/en/statugdiscrim/61779/PDF/default/statugdiscrim.pdf. Date Accessed: March 18, 2017.

Schumann, A. and Zaman, Q. (2005). Software development for real-time ultrasonic mapping of tree canopy size. Computers and Electronics in Agriculture. 47(1): 25-40.

Shearer, S. A. (1987). Plant Identification Using Color Co-Occurrence Matrices Derived from Digitized Images. Ph.D. Dissertation, The Ohio State University, Columbus, Ohio, USA.

Shearer, S. A. and Holmes, R. (1990). Plant identification using color co-occurrence matrices. Transactions of the ASAE. 33(6): 1237-1244.

Stafford, J. and Miller, P. (1993). Spatially selective application of herbicide to cereal crops. Computers and Electronics in Agriculture. 9(3): 217-229.

Swain, K. C., Zaman, Q. U., Schumann, A. W., Percival, D. C., and Bochtis, D. D. (2010). Computer vision system for wild blueberry fruit yield mapping. Biosystems Engineering. 106(4): 389-394.

Tahir, A., Neethirajan, S., Jayas, D., Shahin, M., Symons, S., and White, N. (2007). Evaluation of the effect of moisture content on cereal grains by digital image analysis. Food Research International. 40(9): 1140-1145.

Tang, L., Tian, L. F., Steward B. L., and Reid, J. F. (1999). Texture based weed classification using Gabor wavelets and neural network for real-time selective herbicide applications. ASAE Paper No. 99-3036. St. Joseph, MI., USA.

Tang, L., Tian, L. F., and Steward, B. L. (2003). Classification of broadleaf and grass weeds using Gabor wavelets and an artificial neural network. Transactions of the ASAE. 46(4): 1247.

Teuner, A., Pichler, O., and Hosticka, B. J. (1995). Unsupervised texture segmentation of images using tuned matched Gabor filters. IEEE Transactions on Image Processing. 4(6): 863-870.

Tian, L., Reid, J. F., and Hummel, J. W. (1999). Development of a precision sprayer for site-specific weed management. Transactions of the ASAE. 42(4): 893-902.

Tou, J., Kao, D., and Chang, Y. (1976). An approach to texture pattern analysis and recognition. Proceedings of IEEE Conference on Decision and Control. 23(1): 398-403. doi: 10.1109/CDC.1976.267765.

Tu, J. V. (1996). Advantages and disadvantages of using artificial neural networks versus logistic regression for predicting medical outcomes. Journal of Clinical Epidemiology. 49(11): 1225-1231.

Tuceryan, M., and Jain, A. (1998). Texture Analysis. In: Chen, C. H., Pau, L. F., and Wang P. S. P. (Eds.), Texture Analysis Handbook of Pattern Recognition and Computer Vision (pp. 207-248). World Scientific Publishing Co, River Edge, NJ, USA.

Turner, M. R. (1986). Texture discrimination by Gabor functions. Biological Cybernetics. 55(2): 71-82.

UI-1240-LE Camera Fact Sheet. Retrieved from: https://en.ids-imaging.com/store/ui-1240ml.html. Date accessed: March 18, 2017.

Voorhees, H. and Poggio, T. (1988). Computing texture boundaries from images. Nature. 333: 364-367.

Wang, Z., Chi, Z., and Feng, D. (2003). Shape based leaf image retrieval. Proceedings of IEEE on Vision, Image and Signal Processing. 150 (1): 34-43. doi: 10.1049/ip-vis:20030160.

Weszka, J., Dyer, C., and Rosenfeld, A. (1976). A comparative study of texture measures for terrain classification. IEEE Transactions on System, Man and Cybernetics. 6(4): 269-285.

White, H. (1989). Learning in artificial neural networks: A statistical perspective. Neural Computation. 1(4): 425-464.

Woebbecke, D., Meyer, G., Von Bargen, K., and Mortensen, D. (1995). Color indices for weed identification under various soil, residue, and lighting conditions. Transactions of the ASAE. 38(1): 259-269.

Wu, L. and Boyd, N. S. (2012). Management of spreading dogbane (*Apocynum androsaemifolium*) in wild blueberry fields. Weed Technology. 26(4): 777-782.

Yang, C., Prasher, S. O., and Landry, J. A. (2002). Weed recognition in corn fields using back-propagation neural network models. Canadian Biosystems Engineering. 44(7): 15-22.

Yang, C., Prasher, S. O., Landry, J., and Ramaswamy, H. S. (2003). Development of an image processing system and a fuzzy algorithm for site-specific herbicide applications. Precision Agriculture. 4(1): 5-18.

Yarborough, D. E. and Bhowmik, P. C. (1993). Lowbush blueberry-bunchberry competition. Journal of the American Society for Horticultural Science. 118(1): 54-62.

Zaman, Q., Percival, D., Gordon, R., and Schumann, A. (2008). Estimation of Wild Blueberry Fruit Yield Using Digital Color Photography. Proceedings of International Symposium on Application of Precision Agriculture for Fruits and Vegetables. 824: 57-66. doi: 10.17660/ActaHortic.2009.824.6.

Zaman, Q. U., Schumann, A. W., and Percival, D. C. (2010). An automated cost-effective system for real-time slope mapping in commercial wild blueberry fields. HortTechnology. 20(2): 431-437.

Zaman, Q. U., Esau, T. J., Schumann, A. W., Percival, D. C., Chang, Y. K., Read, S. M., and Farooque A. A. (2011). Development of prototype automated variable rate sprayer for real-time spot-application of agrochemicals in wild blueberry fields. Computers and Electronics in Agriculture. 76(2): 175-182.

Zucker, S. W. (1976). Toward a model of texture. Computer Graphics and Image Processing. 5(2): 190-202.

APPENDIX A: RESULTS OF MULTIVARIATE NORMALITY TESTS AND MATRIX PLOTS FOR DEVELOPMENT OF THE STATISTICAL AND BP-ANN CLASSIFIERS

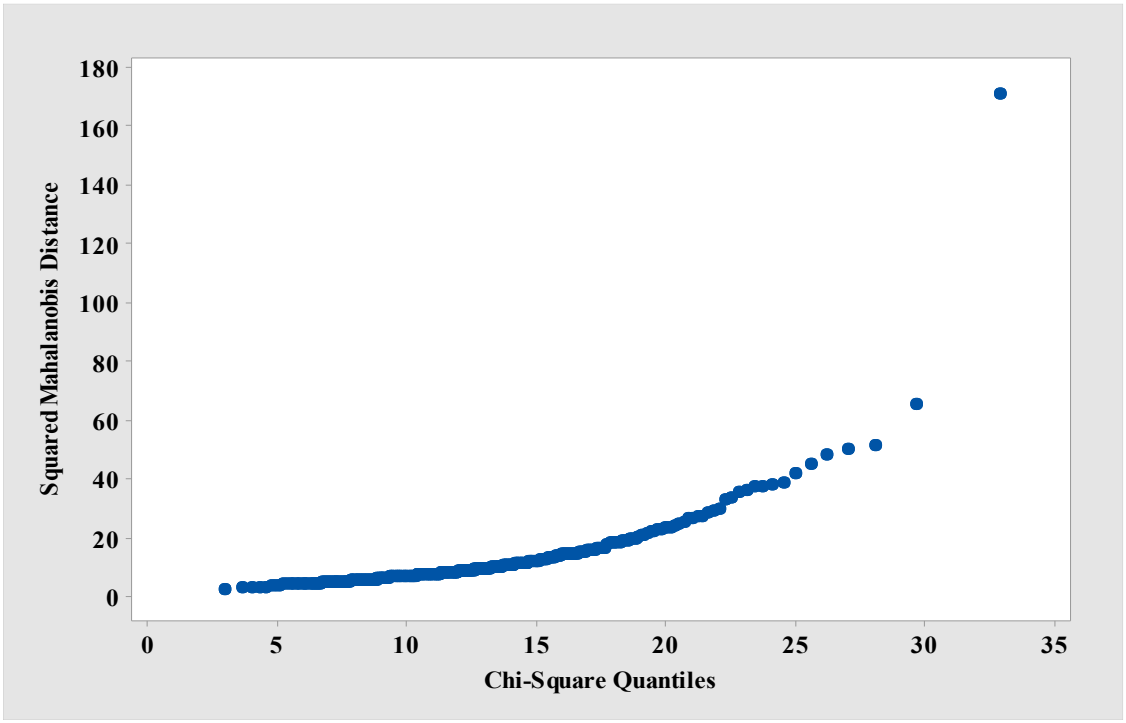

(a)

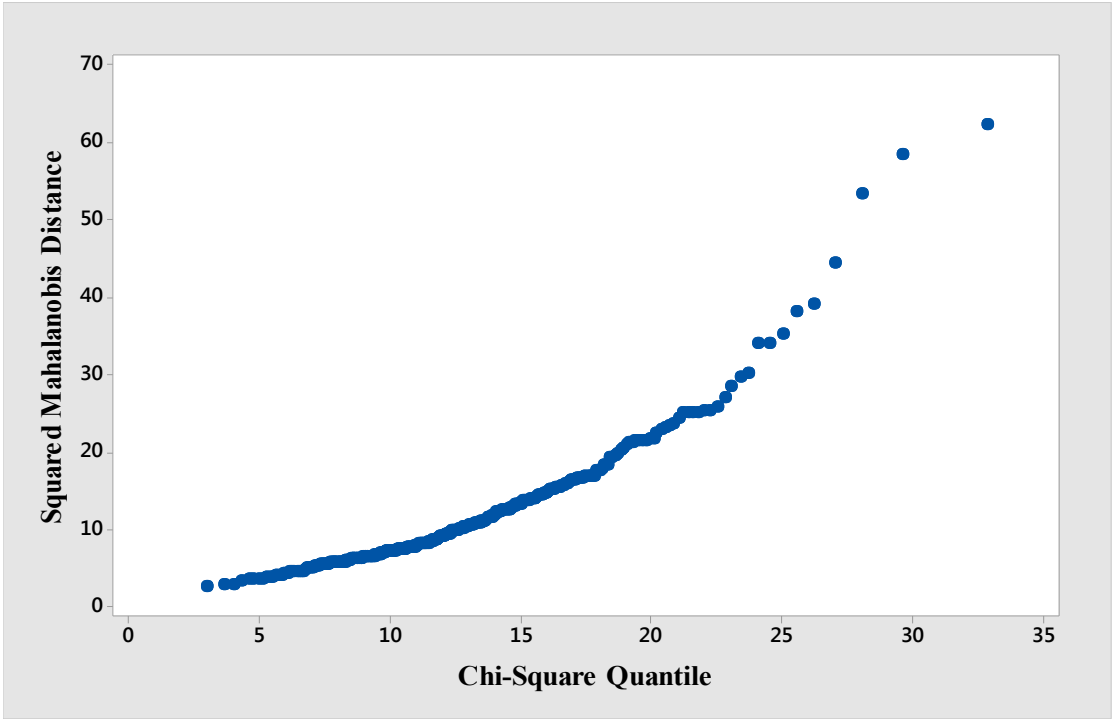

(b)

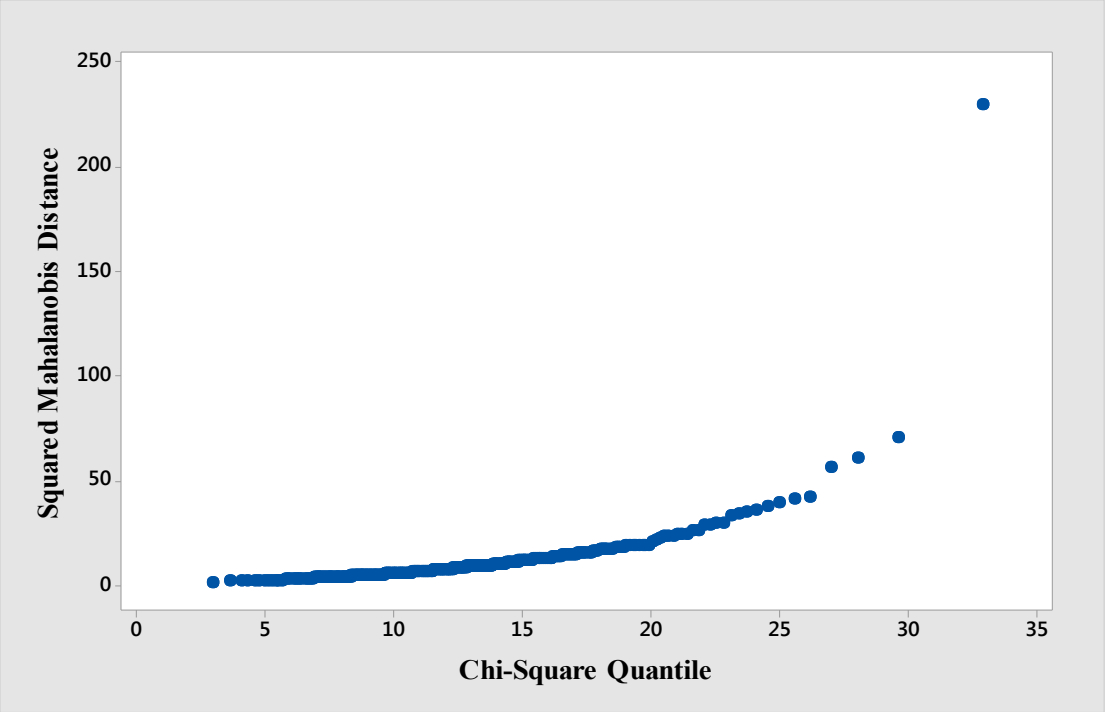

(c)

Figure A-1: Multivariate Normality Plots of Goldenrod Class (a) Hue features (b) Saturation features (c) Intensity features.

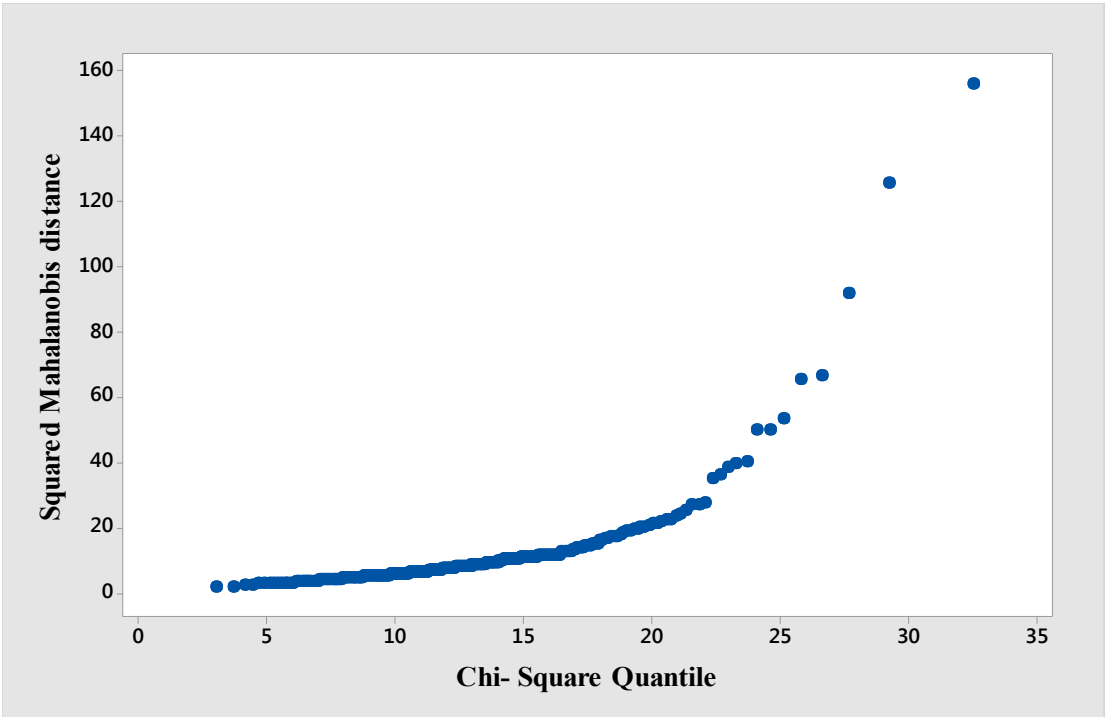

(a)

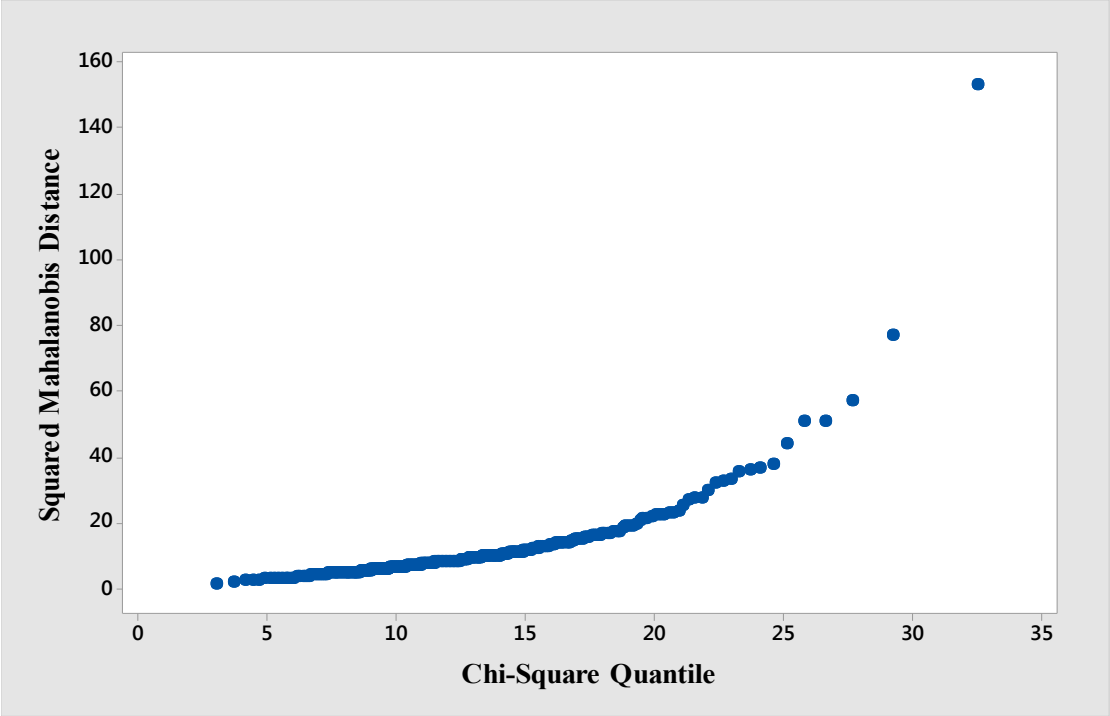

(b)

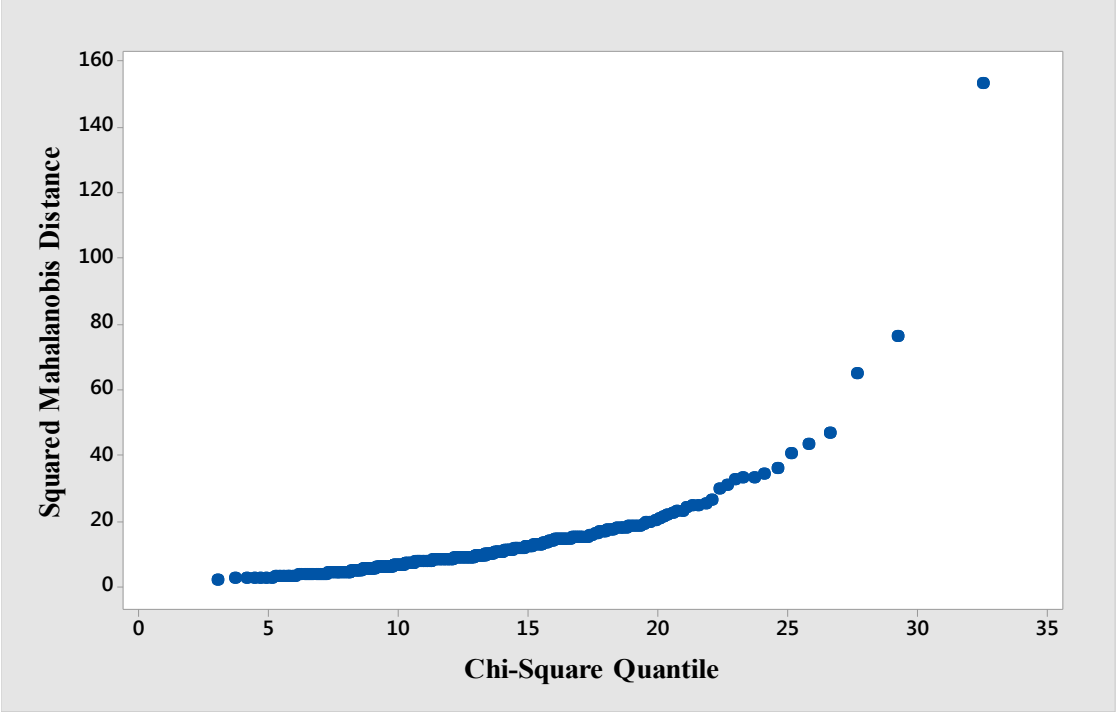

(c)

Figure A-2: Multivariate Normality Plots of Wild Blueberry Class (a) Hue features (b) Saturation features (c) Intensity features.

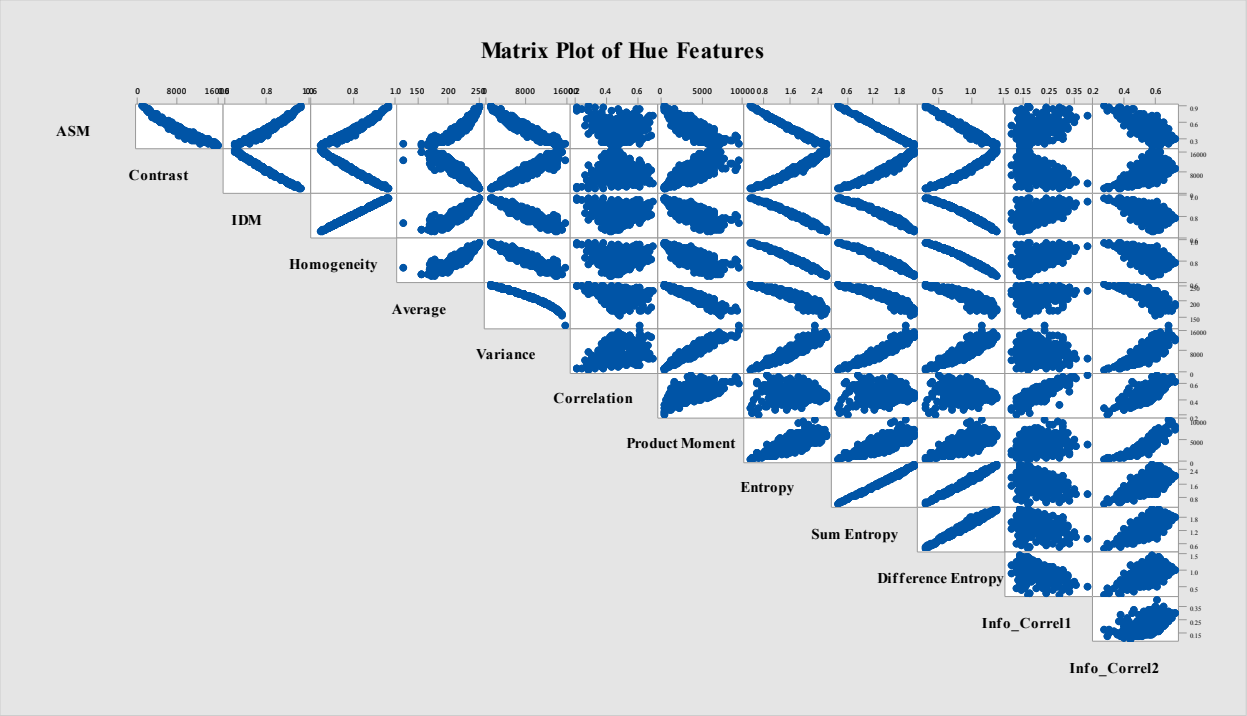
Matrix Plot of Hue Features
ASM
Contrast
IDM
Homogeneity
Average
Variance
Correlation
Product Moment
Entropy
Sum Entropy
Difference Entropy
Info_Correl1
Info_Correl2

(a)

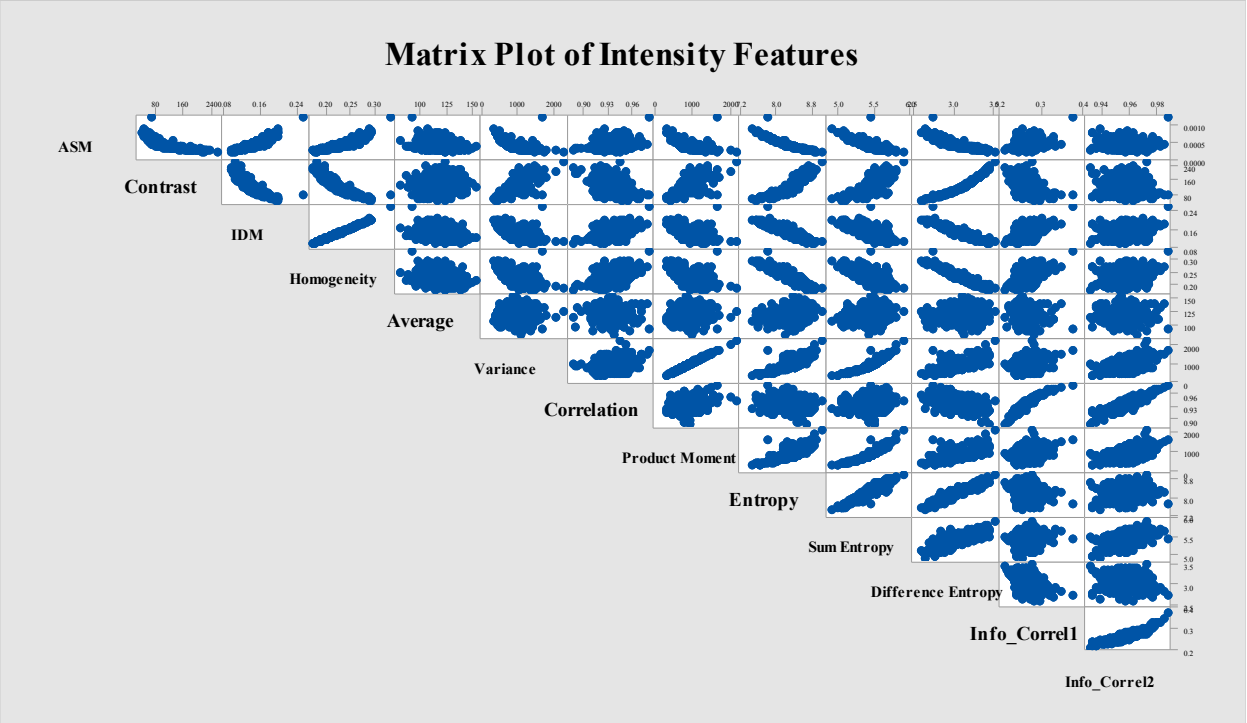
Matrix Plot of Intensity Features
ASM
Contrast
IDM
Homogeneity
Average
Variance
Correlation
Product Moment
Entropy
Sum Entropy
Difference Entropy
Info_Correl1
Info_Correl2

(b)

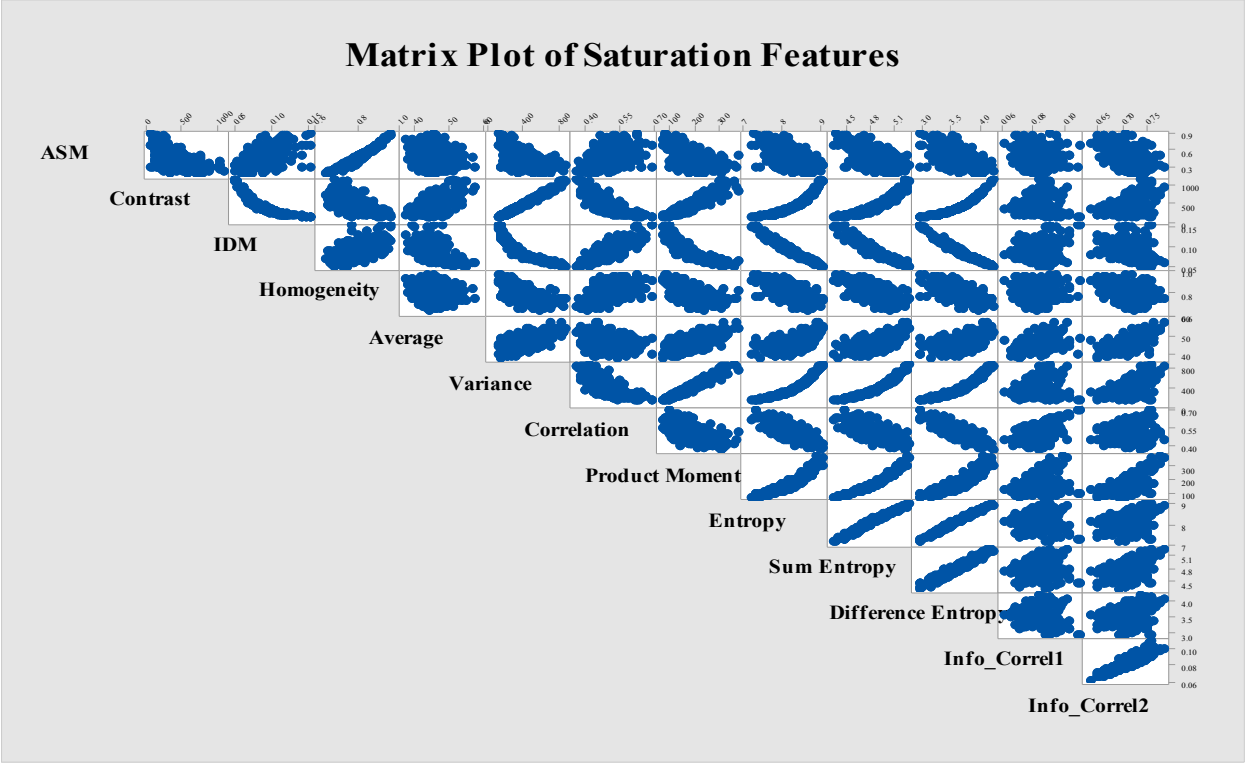

(c)

Figure A-3: Matrix Plots of Goldenrod Class (a) Hue featured (b) Saturation features (c) Intensity features.

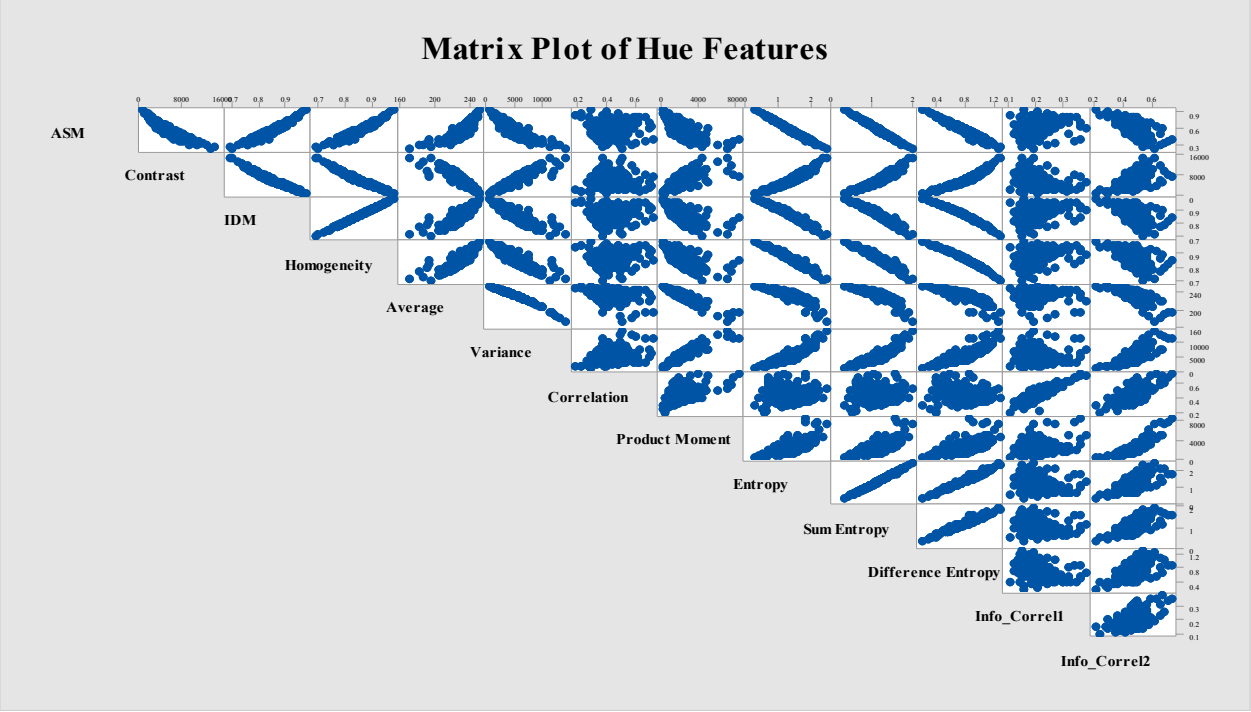

(a)

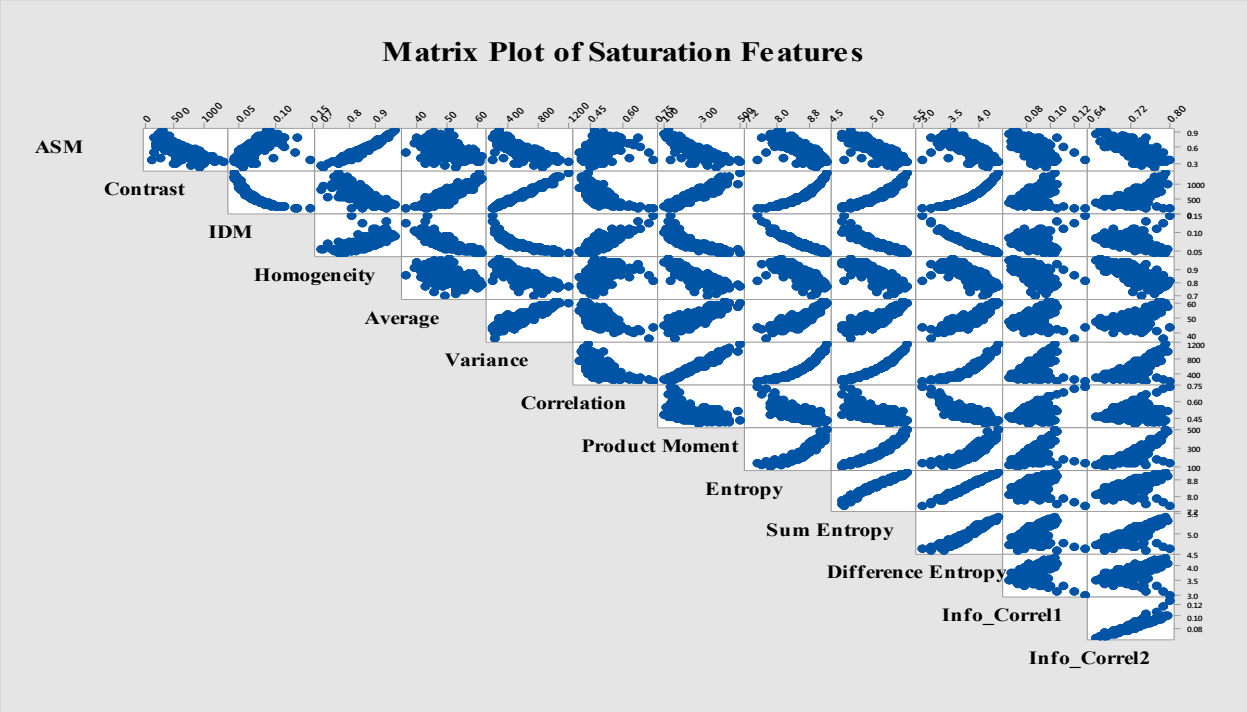

(b)

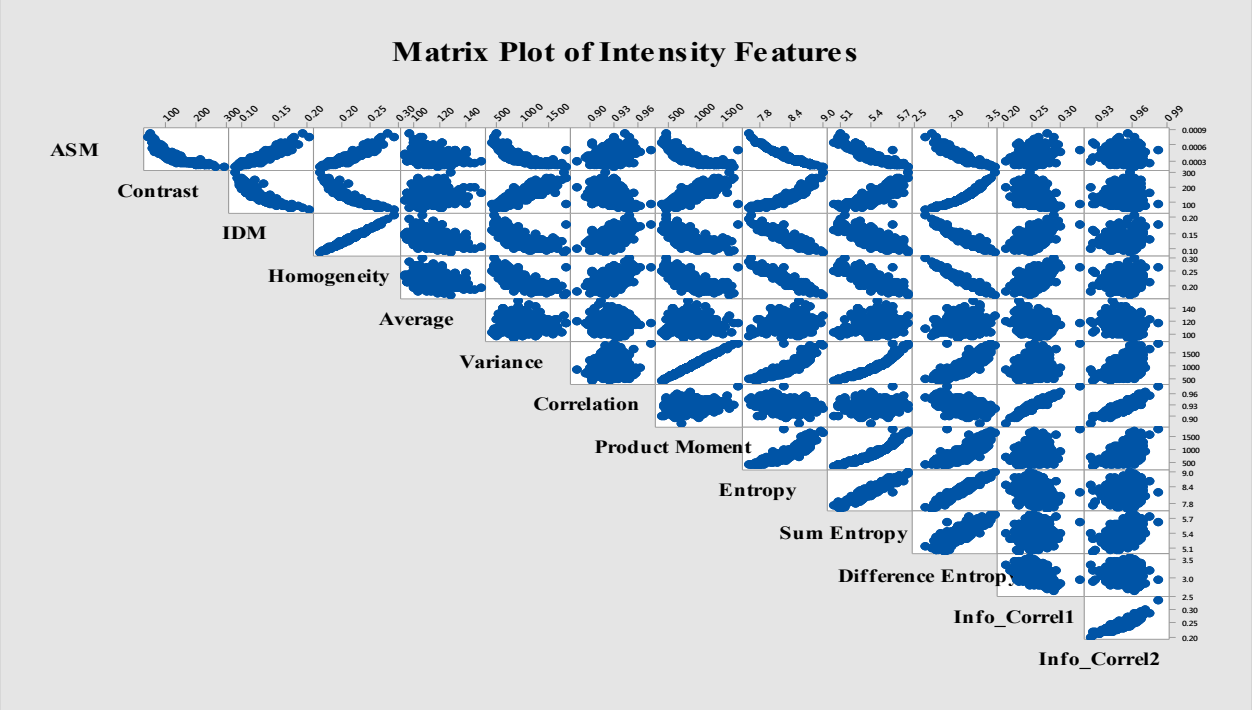

(c)

Figure A-4: Matrix Plots of Wild Blueberry Class (a) Hue Features (b) Saturation features (c) Intensity features.

APPENDIX B: RESULTS OF GOLDENROD DETECTION SYSTEM EVALUATION FROM DIFFERENT FIELD EXPERIMENTS

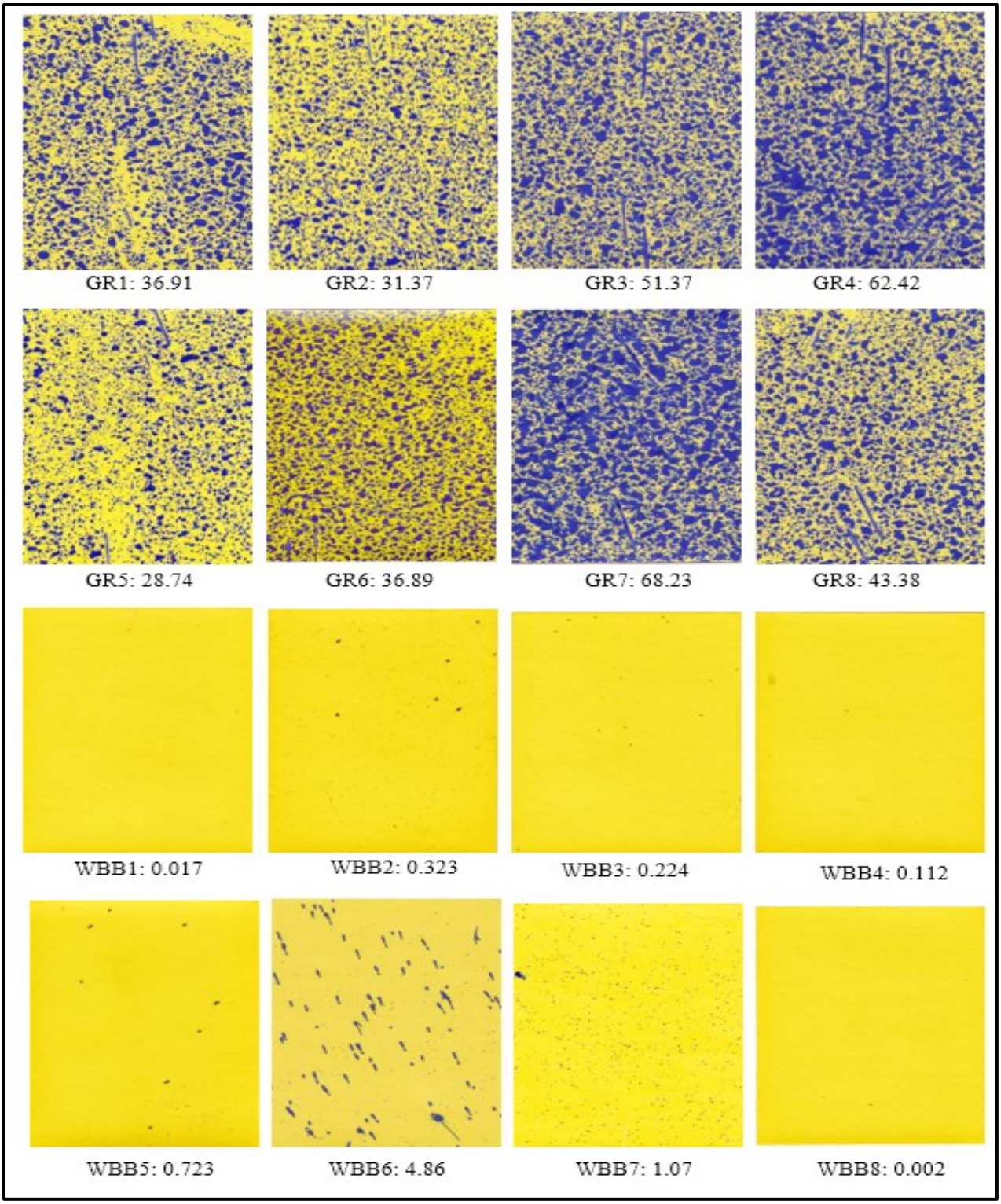

Figure B-1: Second track (T2) of Londonderry field sprayed with BP-ANN classifier (GR represents the selected goldenrod spots and WBB represents selected wild blueberry spots).

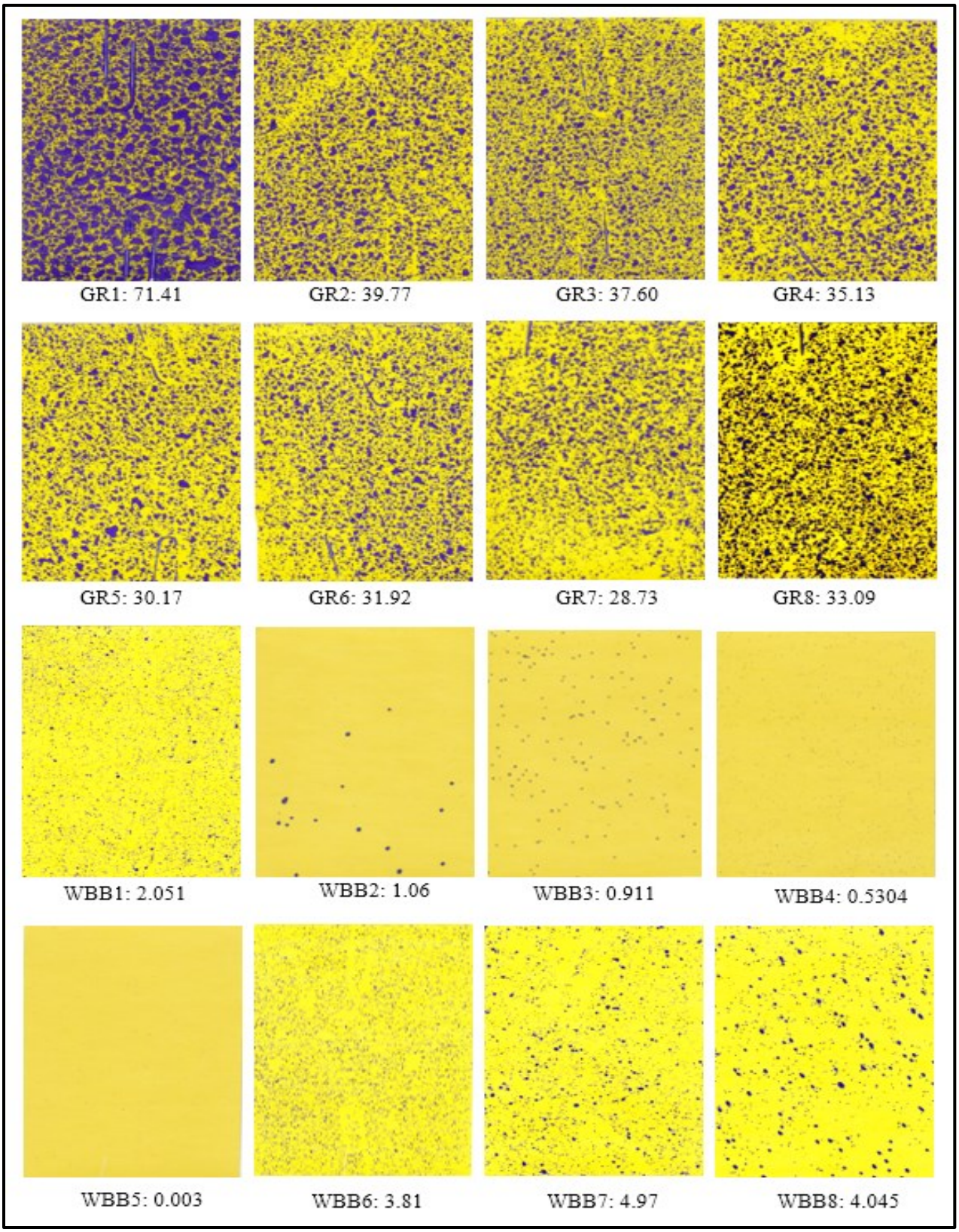

Figure B-2: Second track (T2) of Londonderry field sprayed with quadratic classifier (GR represents the selected goldenrod spots and WBB represents selected wild blueberry spots).

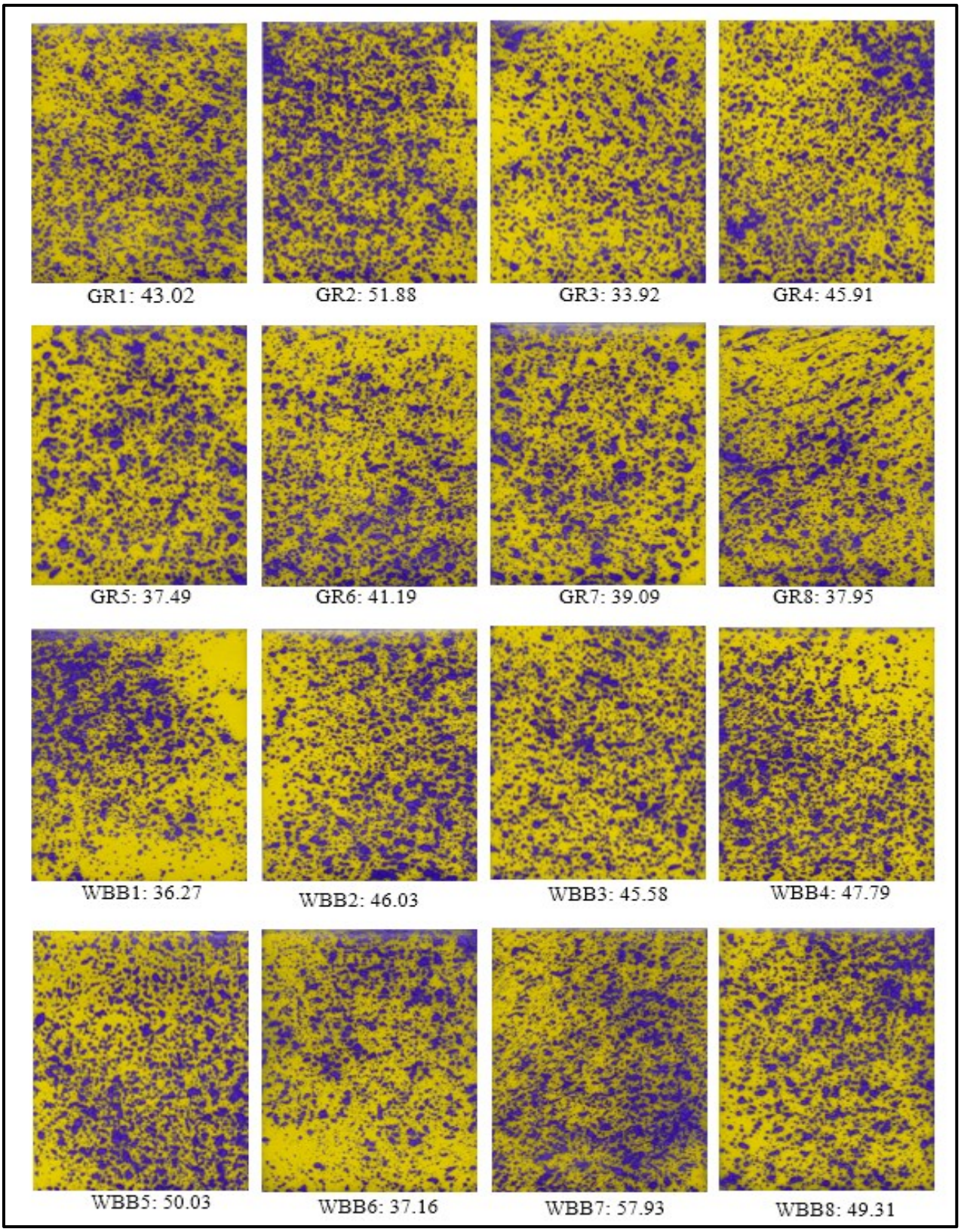

Figure B-3: Second track (T2) of Londonderry field sprayed uniformly (GR represents the selected goldenrod spots and WBB represents selected wild blueberry spots).

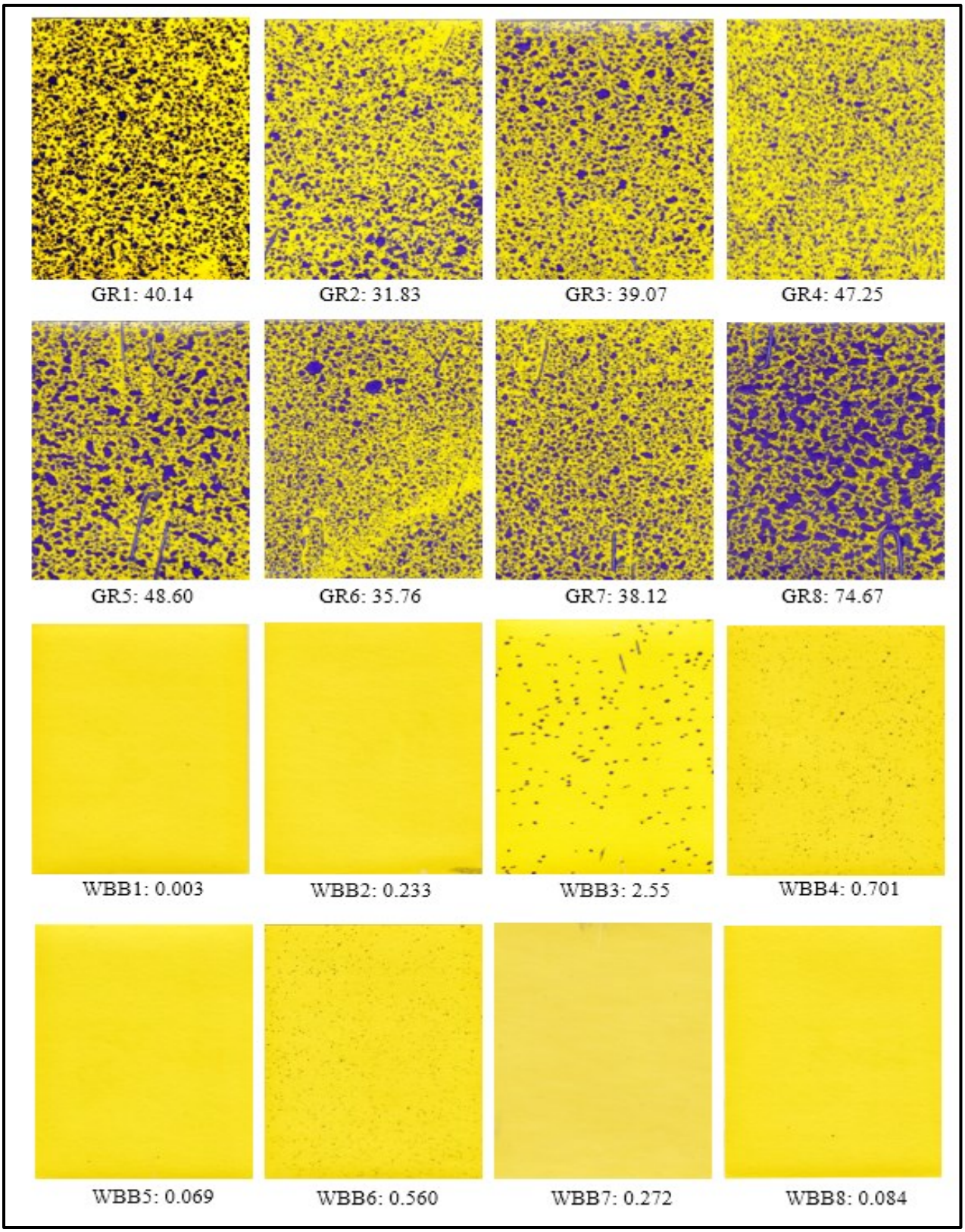

Figure B-4: First track (T1) of North River II field sprayed with BP-ANN classifier (GR represents the selected goldenrod spots and WBB represents selected wild blueberry spots).

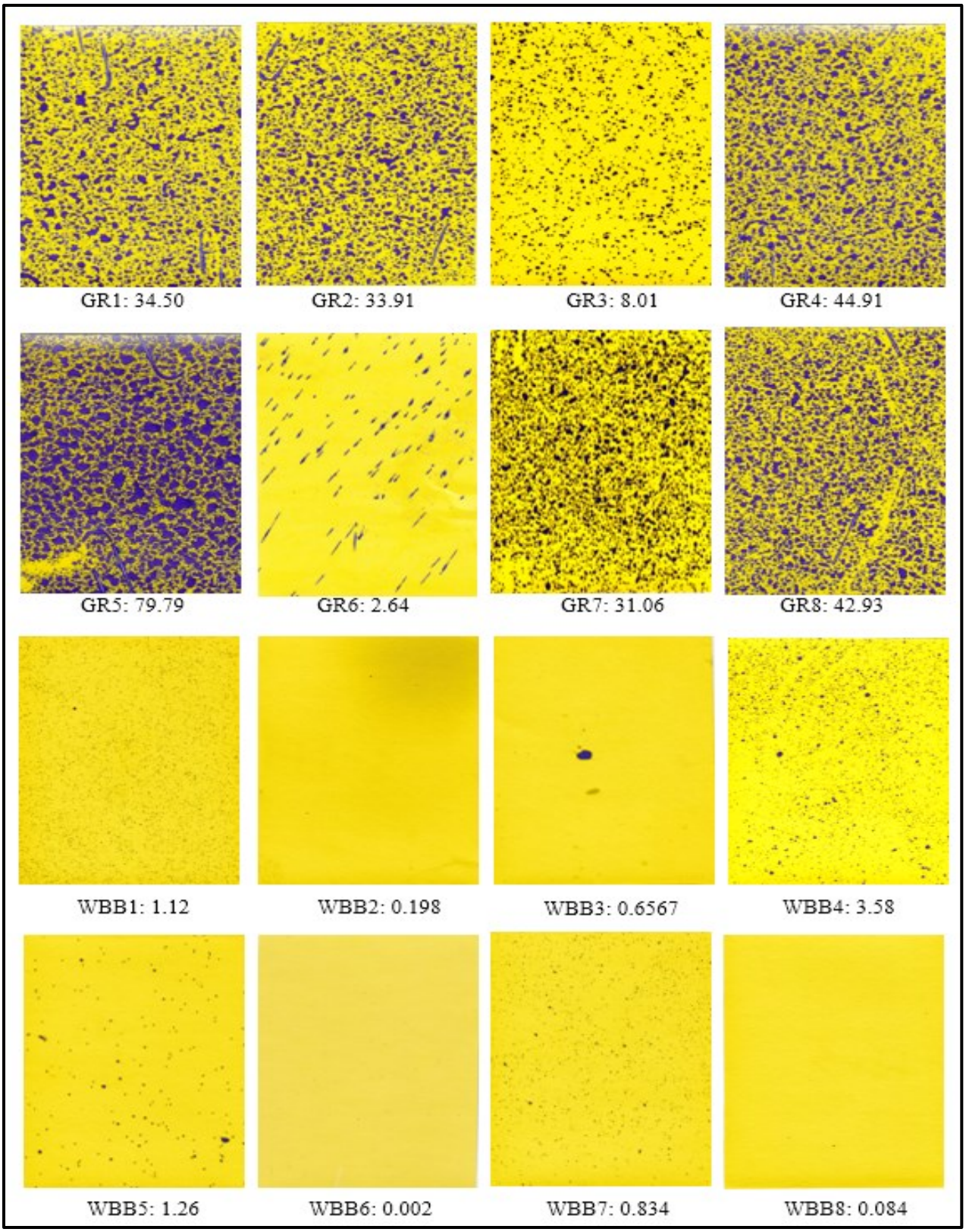

Figure B-5: First track (T1) of North River II field sprayed with quadratic classifier (GR represents the selected goldenrod spots and WBB represents selected wild blueberry spots).

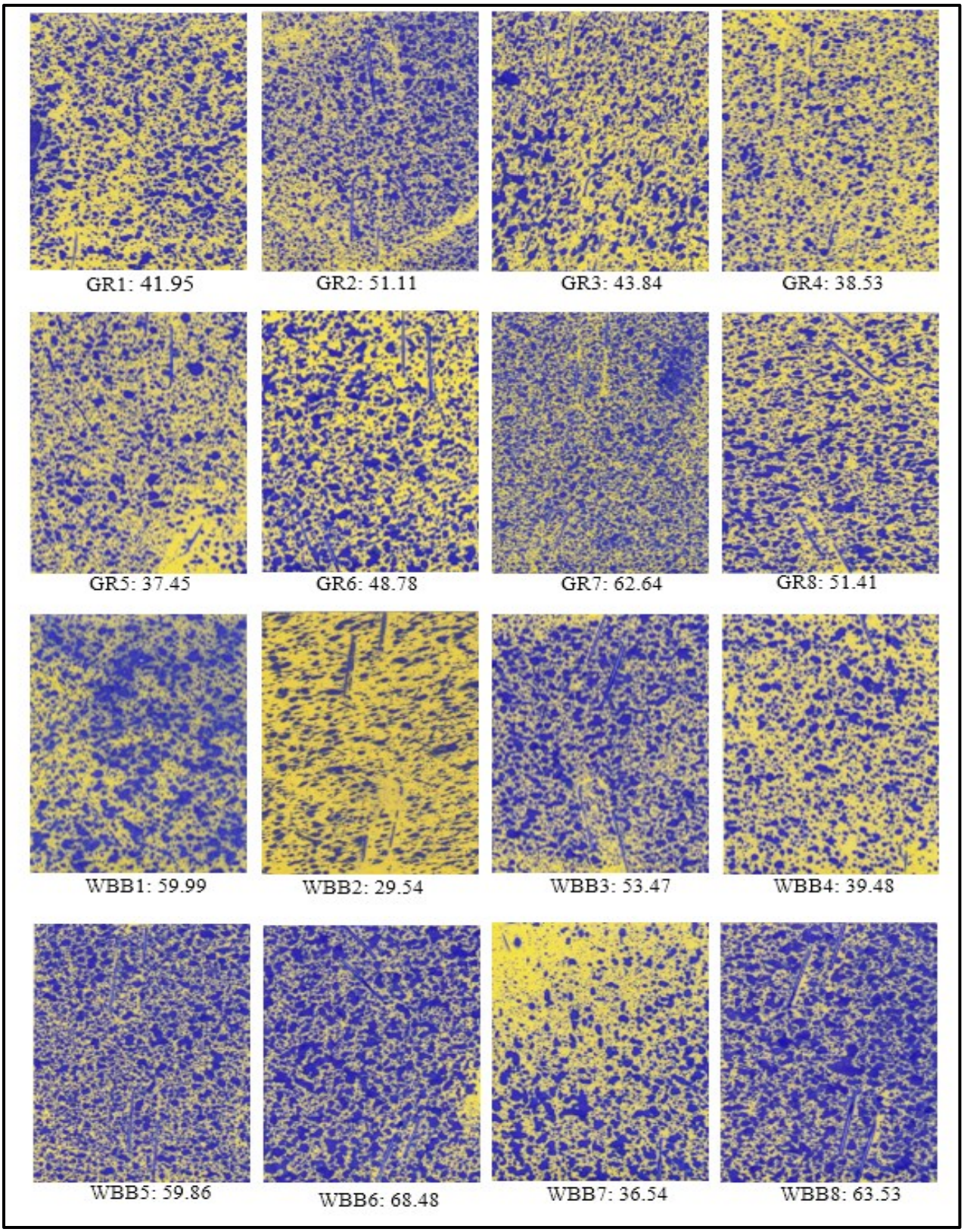

Figure B-6: First track (T1) of North River II field sprayed uniformly (GR represents the selected goldenrod spots and WBB represents selected wild blueberry spots).

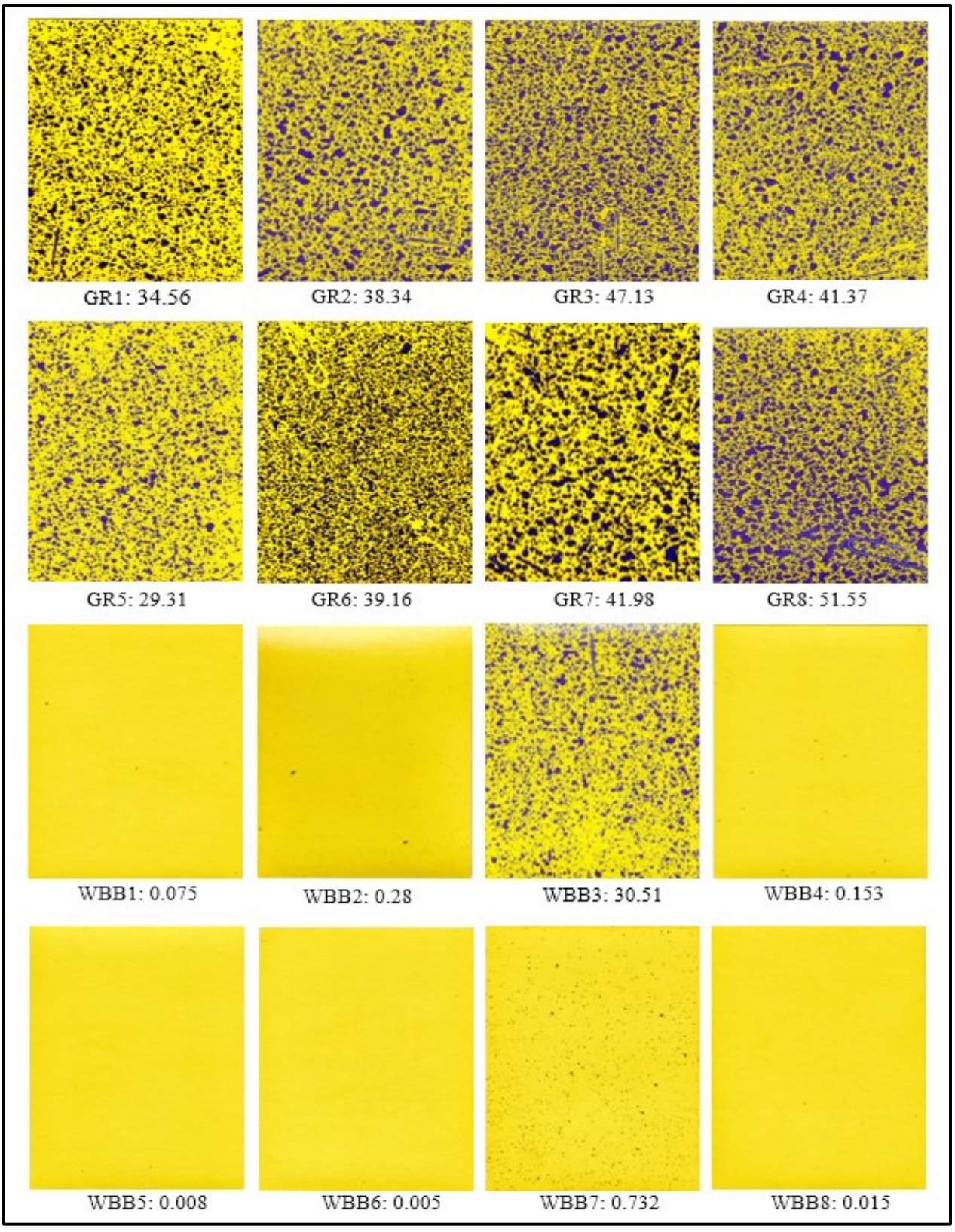

Figure B-7: Second track (T2) of North River II field sprayed with BP-ANN classifier (GR represents the selected goldenrod spots and WBB represents selected wild blueberry spots).

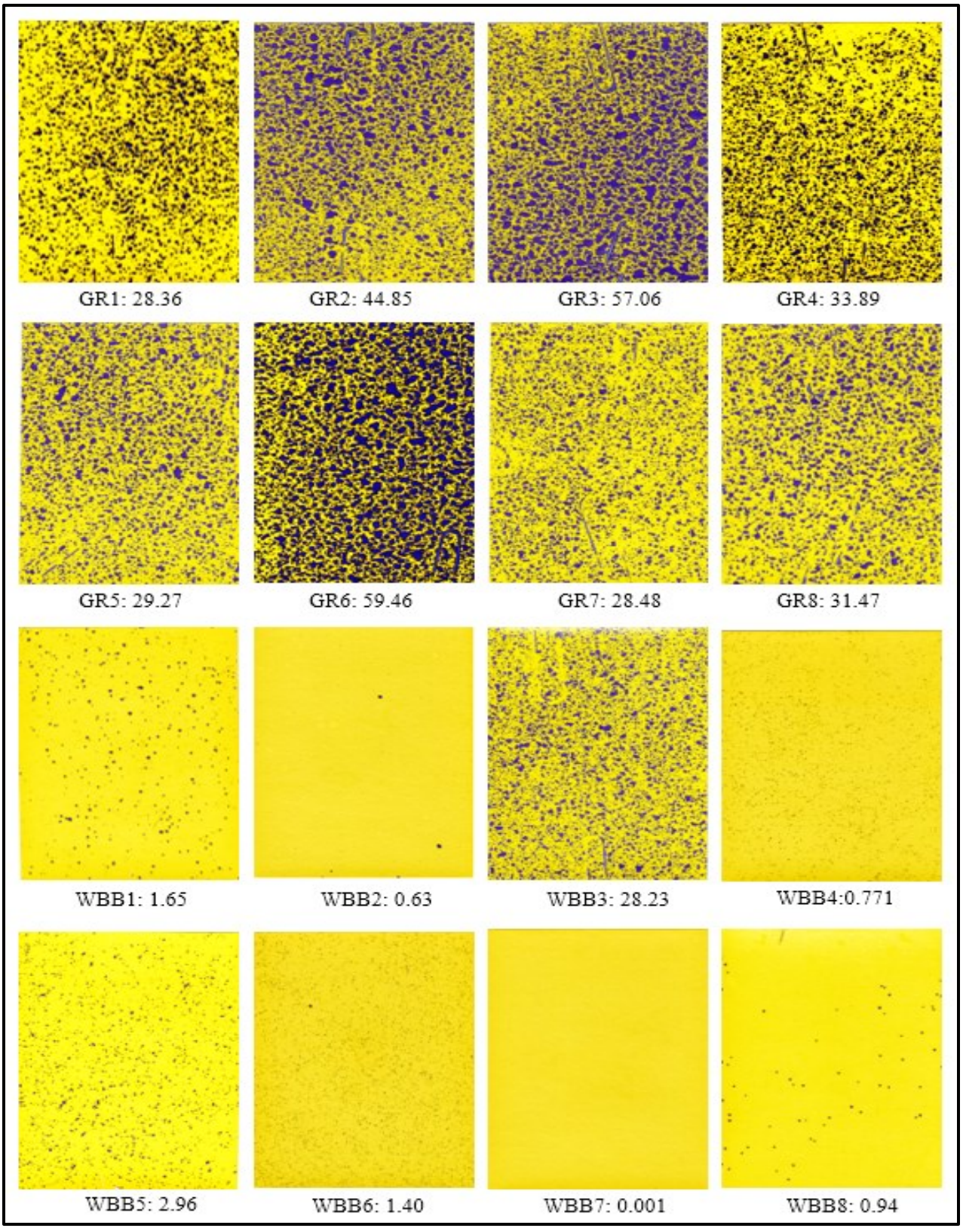

Figure B-8: Second track (T2) of North River II field sprayed with quadratic classifier (GR represents the selected goldenrod spots and WBB represents selected wild blueberry spots).

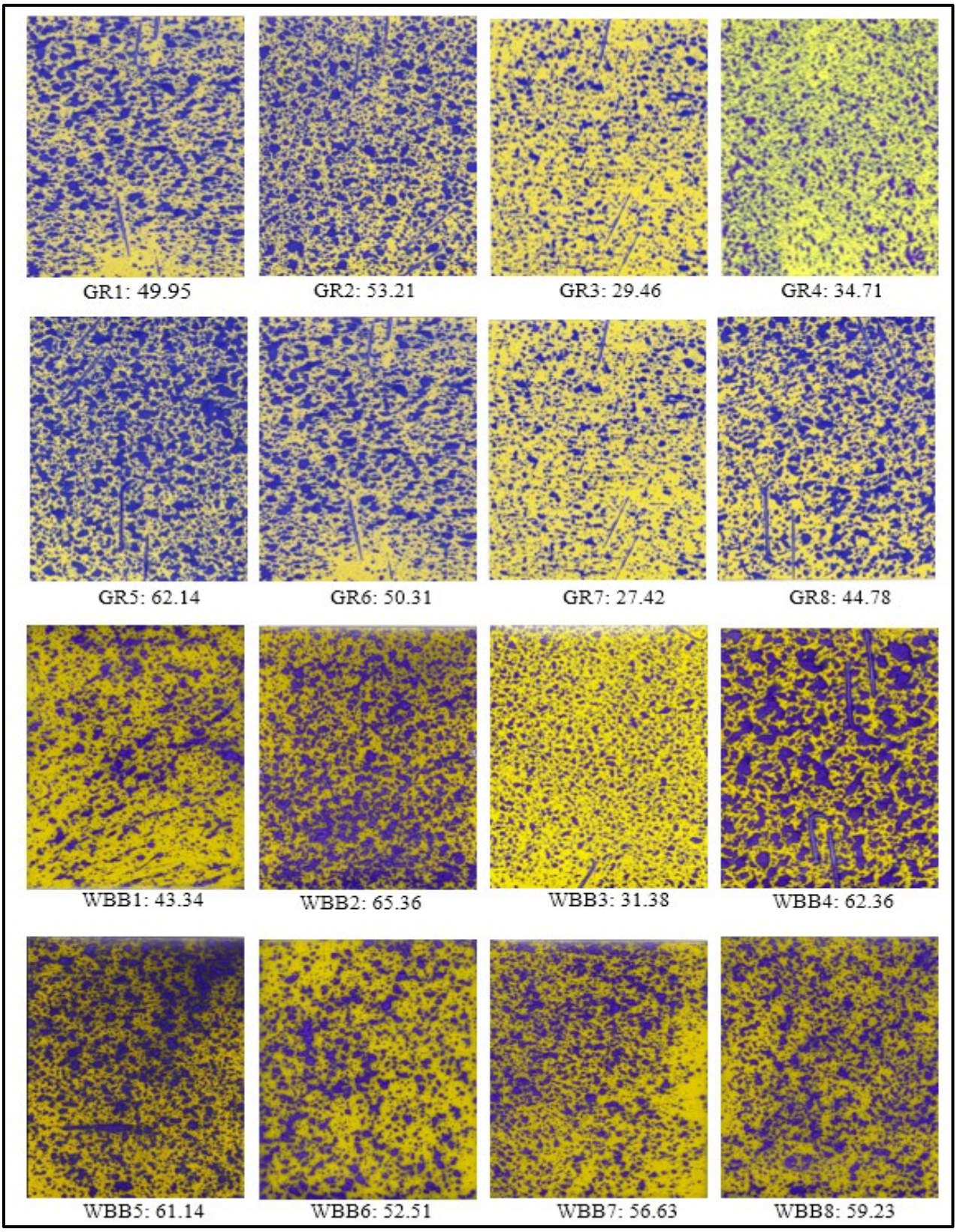

Figure B-9: Second track (T2) of North River II field sprayed uniformly (GR represents the selected goldenrod spots and WBB represents selected wild blueberry spots).